16/7/80

Indian J. pure appl. Phys., Vol. 18 No. 6 pp. 383-464
June 1980
CODEN : IJOPAU ISSN : 0019-5596
18 (6) 383-464 (1980)

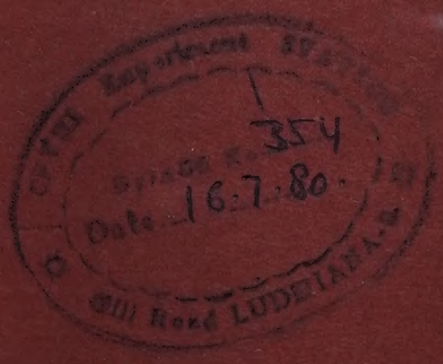

INDIAN JOURNAL OF PURE & APPLIED PHYSICS

Published by
PUBLICATIONS & INFORMATION DIRECTORATE, CSIR, NEW DELHI
in association with
THE INDIAN NATIONAL SCIENCE ACADEMY, NEW DELHI

Flame or Flameless

Pye Unicam AA technology is second to none

The range of Pye Unicam atomic absorption spectrophotometers is now the best ever. With recently-introduced state-of-the-art single and double beam instruments. With an exclusive graphite tube for the SP9-01 that brings new standards of performance to electrothermal atomisation. With a complete range of versatile accessories like the Electrodeless Discharge Lamp System and the automatic Gas Control Unit.
Take time to check the Pye Unicam range against other instruments. Write for our brochures. Only then will you be able to agree that in performance, price, reliability, versatility and ease-of-use Pye Unicam AA spectrophotometers are second to none.

SP191 single beam AA spectrophotometer

SP192 single beam AA spectrophotometer

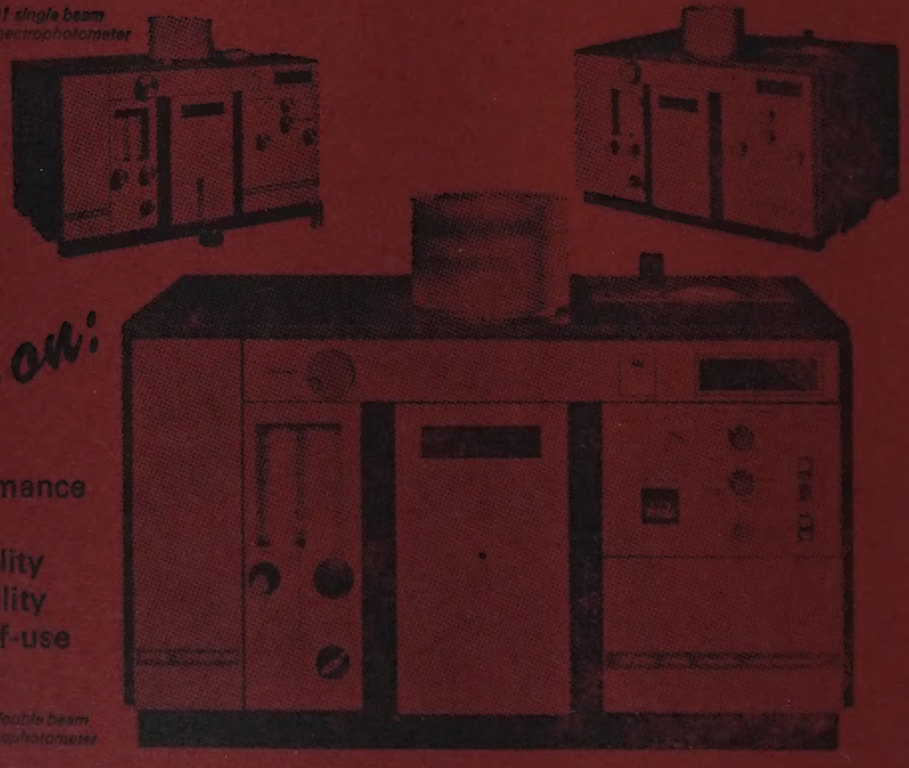

Check on:

- Performance
- Price
- Reliability
- Versatility
- Ease-of-use

SP2900 double beam AA spectrophotometer

For further details contact:
Peico Electronics & Electricals Ltd.
Product Division
Science & Industry
Shivsagar Estate, Block 'A'
Worli, Bombay-400 018

PHILIPS

PESI 4973

Indian Journal of Pure & Applied Physics

VOLUME 18 No. 6 JUNE 1980

EDITORIAL BOARD

Dr B A Dasannacharya
Bhabha Atomic Research Centre
Bombay

Prof. B M Deb
Indian Institute of Technology
Bombay

Prof. P Krishna
Banaras Hindu University
Varanasi

Prof. Krishnaji
Allahabad University
Allahabad

Prof. K V Ramanathan
Tata Institute of Fundamental Research
Bombay

Dr S Chandrasekhar
Indian National Science Academy
New Delhi/Raman Research
Institute Bangalore

Prof. A K Saha
Saha Institute of Nuclear Physics
Calcutta

Prof. N C Sil
Indian Association for
Cultivation of Science
Calcutta

Prof. R Srinivasan
Indian Institute of Science
Bangalore

Prof. K Venkataramiah
Osmania University
Hyderabad

Dr K L Chopra
Indian National Science Academy
New Delhi/Indian Institute of
Technology New Delhi

Shri Y R Chadha, *Ex-officio* Secretary & Chief Editor

EDITORIAL STAFF

Editors
D S Sastry & K S Rangarajan

Assistant Editors
G N Sarma, J B Dhawan & Tarun Banerjee

Published by the Publications & Information Directorate, CSIR, Hillside Road, New Delhi 110 012

Chief Editor : Y R Chadha

The Indian Journal of Pure & Applied Physics is issued monthly. The Directorate assumes no responsibility for the statements and opinions advanced by contributors. The editorial staff in its work of examining papers received for publication is assisted, in an honorary capacity, by a large number of distinguished scientists, working in various parts of India.

Communications regarding contributions for publication in the journal should be addressed to the Editor, Indian Journal of Pure & Applied Physics, Publications & Information Directorate, Hillside Road, New Delhi 110 012.

Correspondence regarding subscriptions and advertisements should be addressed to the Sales & Distribution Officer, Publications & Information Directorate, New Delhi 110 012.

Annual Subscription	**Single Copy**
Rs. 100.00 £ 16.50 $ 42.00	Rs. 10.00 £ 1.80 $ 4.50

50% Discount is admissible to research workers and students and 25 % discount to non-research individuals, on annual subscription. Payments in respect of subscriptions and advertisements may be sent by cheque, bank draft, money order or postal order marked payable *only* to **Publications & Information Directorate, New Delhi 110 012.** Claims for missing numbers of the journal will be allowed only if received within 3 months of the date of issue of the journal plus the time normally required for postal delivery of the journal and the claim.

© 1980 The Council of Scientific & Industrial Research, New Delhi.

CSIR SCIENTIFIC PERIODICALS

JOURNAL OF SCIENTIFIC & INDUSTRIAL RESEARCH (monthly)

With a fine record of over 35 years' service to the scientific community, this Journal has grown into India's leading general science periodical. Intended to fulfil the responsibility of helping the research workers to keep themselves abreast of current developments in various fields of science and technology, the Journal carries editorial features highlighting important scientific events in India and abroad; articles on science policy and management of science; review articles on topics of current research interest; technical reports on international and national conferences; reviews of scientific and technical publications; and notes on major advances in various fields.

Annual subscription	**Rs 60.00**	**£ 10.00**	**$ 25.00**
Single copy	6.00	1.00	2.50

INDIAN JOURNAL OF CHEMISTRY (monthly)

This Journal which is running the 18th year of its publication, Consists of the following two sections.

Section A : This section is devoted to papers in Inorganic, Physical, Theoretical and Analytical Chemistry.

Annual subscription	**Rs 70.00**	**£ 12.00**	**$ 30.00**
Single copy	7.00	1.20	3.00

Section B : This section is devoted to papers in Organic Chemistry including Medicinal Chemistry.

Annual subscription	**Rs 70.00**	**£ 12.00**	**$ 30.00**
Single copy	7.00	1.20	3.00

INDIAN JOURNAL OF PURE & APPLIED PHYSICS (monthly)

This Journal, which is running the 18th year of its publication, is devoted to original research communications (full papers and short communications) in all conventional branches of physics (except radio and space physics).

Annual subscription	**Rs 100.00**	**£ 16.50**	**$ 42.00**
Single copy	10.00	1.80	4.50

INDIAN JOURNAL OF RADIO & SPACE PHYSICS (bimonthly)

This Journal serves as a medium for the publication of original rearch work (full papers and communications) in various areas of radio and space physics.

Annual subscription	**Rs 60.00**	**£ 10.00**	**$ 25.00**
Single copy	12.00	2.00	5.00

INDIAN JOURNAL OF TECHNOLOGY (INCLUDING ENGINEERING) (monthly)

This Journal publishes papers reporting results of original research of applied nature pertaining to unit operations, heat and mass transfer, products, processes, instruments, and appliances, etc. The Journal is of special interest to research workers in the departments of applied sciences in universities, institutes of higher technology, commodity research laboratories, industrial cooperative research institutes, and industrial research laboratories.

Annual subscription	**Rs 60.00**	**£ 10.00**	**$ 25.00**
Single copy	6.00	1.00	2.50

INDIAN JOURNAL OF EXPERIMENTAL BIOLOGY (monthly)

This Journal, devoted to the publication of research communications in the fields of experimental botany, zoology, microbiology, pharmacology, endocrinology, nutrition, etc., is the only one in India with such a wide coverage and scope.

Annual subscription	**Rs 120.00**	**£ 20.00**	**$ 50.00**
Single copy	12.00	2.00	5.00

INDIAN JOURNAL OF BIOCHEMISTRY & BIOPHYSICS (bimonthly)

This Journal, published in association with the Society of Biological Chemists (India), Bangalore, is the only research Journal in India devoted exclusively to original research communications in biochemistry and biophysics.

Annual subscription	**Rs 40.00**	**£ 7.00**	**$ 17.00**
Single copy	8.00	1.40	3.50

INDIAN JOURNAL OF MARINE SCIENCES (quarterly)

Commencing publication from June 1972, this Journal is devoted to research communications (full papers and short communications) pertaining to various facets of marine research, viz. biological, physical, geological and chemical oceanography.

Annual subscription	**Rs 40.00**	**£ 7.00**	**$ 17.00**
Single copy	12.00	2.00	5.00

RESEARCH & INDUSTRY (quarterly)

Intended to serve as a link between science and industry, this Journal is addressed primarily to technologists, engineers, executives and others in industry and trade. It publishes informative original articles containing practical details of processes and products developed in India, which show promise of ready utilization, and technical digests on new processes, products, instruments and testing methods which are of interest to industry. Developments in Indian industry are regularly reported.

Annual subscription	**Rs 24.00**	**£ 4.00**	**$ 10.00**
Single copy	7.25	1.30	3.50

INDIAN JOURNAL OF TEXTILE RESEARCH (quarterly)

Commencing publication from March 1976, this Journal is devoted to the publication of papers reporting results of fundamental and applied researches in the field of textiles.

Annual subscription	**Rs 36.00**	**£ 6.00**	**$ 15.00**
Single copy	12.00	2.00	5.00

Please contact

THE SALES & DISTRIBUTION OFFICER
PUBLICATIONS & INFORMATION DIRECTORATE, CSIR
HILLSIDE ROAD, NEW DELHI 110 012

Indian Journal of Pure & Applied Physics

VOLUME 18 ... No. 6 JUNE 1980

CONTENTS

Solid State Physics

The Fatigue of Copper-Chromium Alloy 383
AFAF A GADALLA & VOLAMAR GEROLD

Electrical Conduction & Isothermal Dielectric Relaxation in Perspex 387
MALINI VARIYAR, M L KHARE & C S BHATNAGAR

Chemical Physics

Relationship between Potential Energy Constants & Heat of Atomization ... 392
G THYAGARAJAN & M K SUBHEDAR

Interpretation of the Spectra of Substituted Borazines by Urey-Bradley Force Field 396
M K SUBHEDAR & G THYAGARAJAN

Dielectrics & Microwaves

Dielectric Properties of Indian Clay Minerals : Bentonite & Pyrophillite ... 401
M K MAHAN, B L JHA & A R CHETAL

Dielectric Relaxation in Methylmercaptoacetate & Methylcyanoacetate in Benzene Solution 404
K SENGUPTA

Theoretical Physics

Close-Coupling Approach to Low Energy Electron Scattering by Oxygen Molecule 408
A K PANDE, D N TRIPATHY & R S SINGH

General Physics

Measurement & Analysis of Solar Radiation & Illumination for Clear Sky Conditions 413
M CHANDRA

Lasers, Masers & Holography

Laser Power Fluctuations due to Striations in a He-Ne Laser Operating at 6328Å 419
V D DANDAWATE

Spectroscopy

The $\tilde{a}^3A''-\tilde{X}^1A'$ Phosphorescence of Chlorobenzaldehyde Vapours 429
M K HAQUE & S N THAKUR

A Method of Absolute Spectroscopic Analysis Using X-ray Fluorescence Technique 437
T V KRISHNAN

Electronics

Acquisition Behaviour of Phase Locked Loops in the Face of Rayleigh & Lognormal Fading Signals 441
B C SARKAR, A K BHATTACHARYA, S K RAY & B N BISWAS

CONTENTS

COMMUNICATIONS

An Alternative Approach for the Description of Physical Properties in Ferroic Species 449

P GOPALAKRISHNA MURTI & S UMA DEVI

NOTES

Electrical Properties of Bi_2O_3 Layers under Reduced Pressure 452

S L PANDEY, S SINGH & R N SAXENA

Fermi Surface Distortion in Sodium 454

K N KHANNA

Effect of Magnetic Field on the Current Gain of Junction Transistors 455

N MANOHARA MURTHY, P MALLIKARJUNA REDDY & S V SUBRAHMANYAM

Surface Tension of Hard Sphere Liquids with Attractive Interactions & Estimation of Rao's Acoustical Parameter 457

B K SHARMA

Transport Properties of Neon, Krypton & Xenon According to L-J (12-6) Potential 459

P C JAIN

Calculations of CSDA Range & Projected Range of Monoenergetic Electrons ... 461

S K GUPTA & D K GUPTA

Indian Journal of Pure & Applied Physics
Vol. 18, June 1980, pp. 383-386

The Fatigue of Copper-Chromium Alloy

AFAF A GADALLA & VOLKMAR GEROLD*
Physics Department, Assiut University, Assiut, Egypt

Received 16 *September* 1978; *revised received* 26 *March* 1979

The characteristics of deformation of Cu-Cr alloy, containing 0·75% Cr subjected to fully reversed cyclic strain were investigated at room temperature. Generally the knee in the fatigue curves is found between 10^6 and 10^7 cycles. Also evidence is presented to show a dislocation structure associated with fatigue strain near the specimen surface which is discussed as cell dislocation structures. Some cracks have been observed on the surface of specimens after fatigue.

1. Introduction

In the search for a copper-base alloy with high strength properties, it was considered that the addition of small amounts of an age-hardening element to a binary system with useful strength might result in an alloy of theoretical and practical importance. The mechanical properties of Cu-Cr binary alloy were first studied by Hibbard and his coworkers[1]; their study demonstrated its promising nature as a good high-strength alloy. Corson[2] found that a range of 0·6-0·8% Cr sufficed to produce the maximum hardening and strengthening effects on ageing at 400 to 600°C. Davis[3] investigated the properties of a Cu-Cr alloy in the solution-treated and aged condition. In general, Davis found that greatest strength is obtained by homogenizing at the highest alpha temperature (1000-1050°C) and precipitation hardening between 400-500°C. From the phase diagram it can be predicted[4] that this alloy is of the precipitation-hardening type.

The present work is an attempt to determine the relationship between the *S-N* curves and the fatigue hardening curves of this alloy. Also a number of investigations have been carried out by transmission microscopy.

2. Experimental Procedure

2.1 Preparation of the Specimen

The starting materials were supplied by Wieland-Werks A G, West Germany. The chemical composition of this Cu-Cr alloy was such that it contained 0·75% Cr by weight. Sheets and rods were cut and specimens for fatigue experiments were prepared as shown in Fig. 1. They were machined to 0·16 in. in diameter and 0·7 in. in length. A number of specimens were carefully quenched in water after long annealing at 1050°C in argon gas; then they were polished chemically by total immersion in 60-40% solution of HNO_3 and CH_3OH respectively. The final surface has a mirror-like appearance.

2.2 Tensile Testing and Fatigue Experiments

The tensile properties were measured on 0·02 in sheet specimens of width 0·2 in. and 2 in. gauge length. They were aged at 400°C for different periods. The samples were pulled in an Instron tensile machine at 0·04 in./minute. The load-elongation curves were recorded automatically and transformed into true stress-strain curves. The strain cycles and fatigue studies on Cu-0·75% Cr alloy were performed on four groups of samples treated as detailed in Table 1. The annealing process was done in an evacuated sealed quartz tube and then cooled to room temperature. Comparison between the four groups was done by obtaining the fatigue characteristic curves, which were carried out at constant total strain amplitudes at room temperature. For this measurement, hydraulic fatigue testing machine was used.

2.3 Electron Microscopy

The metallographic features of precipitation at various treatments were observed and the dislocation arrangements in the strained specimens were investigated by transmission electron microscope.

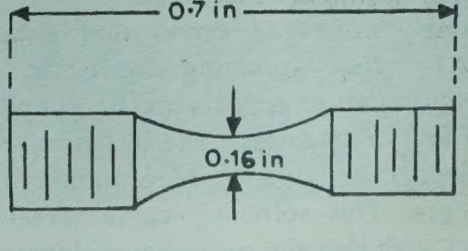

Fig. 1—The shape of the fatigue specimen

* Present Address : Max-Planck Institut fur Metallkunde, 7000 Stuttgart 1, Seeslasse 75, West Germany

Table 1—Groups of Treated Cu-0·75% Cr Alloy Samples

Group	Sample
I	Specimen quenched after homogenizing at 1050°C
II	Specimen annealed at 400°C for one day after quenching
III	Specimen twisted at 270°C and then annealed at 400°C for 1 day after quenching
IV	Specimen twisted, pre-annealed for 72 hr at 100°C and annealed at 400 °C for 1 day after quenching

The fatigued specimens were sectioned by spark-machine to get circular discs with parallel faces (0·3 mm thickness) at 45°. The technique which was established for the prepration of electron-transparent foils was the jet polishing method[5] using an electrolyte consisting of 500 ml of nitric acid and methanol and applying a potential difference of 13 V at −20°C. The foil samples were examined using an electron microscope operating at 100 kV. The selected images were determined from more than ten electron micrographs taken from different areas and foils.

3. Results and Discussion

3.1 Stress-Strain Curves

The tensile properties which were measured on Cu-0·75%Cr alloy aged at 400°C for various periods of time are shown in Fig. 2. A few samples were started at a lower strain rate but this caused no perceptible difference. The yield strength (0·2% strain) is plotted in Fig. 3, while the cyclic strain characteristics of Cu-Cr alloy at different treatments are given in Fig. 4.

The ageing of copper chromium alloy occurs in two stages.[4] The first stage appears to be the precipitation of very fine coherent plates of chromium, while the second stage consists of the competitive growth of these plates. The major changes in sample length occur during the first stage.

Examination of Fig. 4 shows that either strain hardening or strain softening can occur, and the most significant effect appears to be found in the region of low strain cycles. The softening tendencies of specimen I becomes more pronounced for all strain ranges. This softening curve reveals several curvatures such that the curve has a slope which is increasing at the point of failure. The cyclic strain

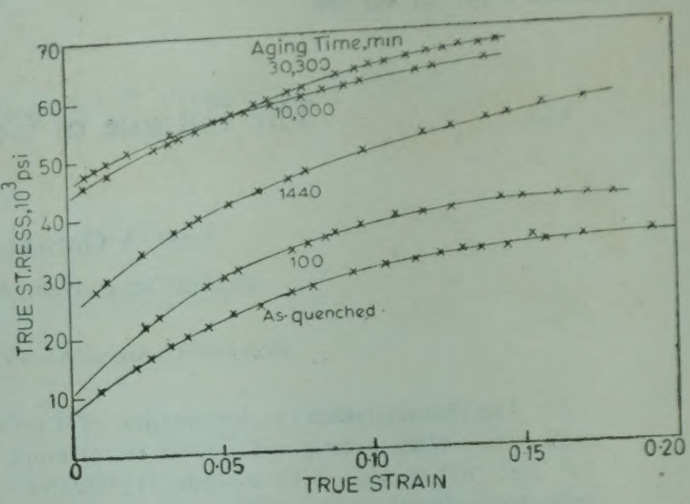

Fig. 2—Flow curves of a copper-base 0·75% Cr alloy aged at 400°C

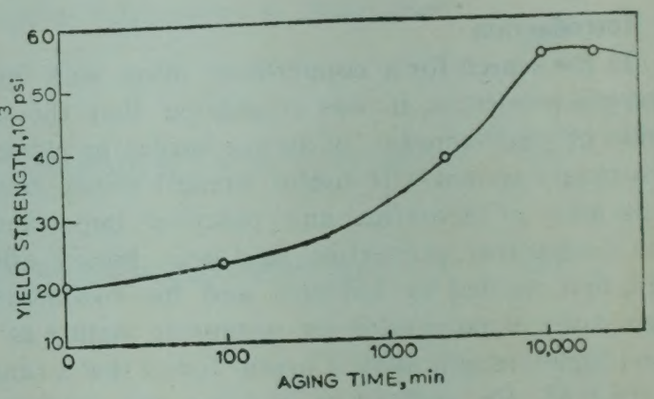

Fig. 3—Yield strength of Cu-Cr alloys versus ageing time at 400°C

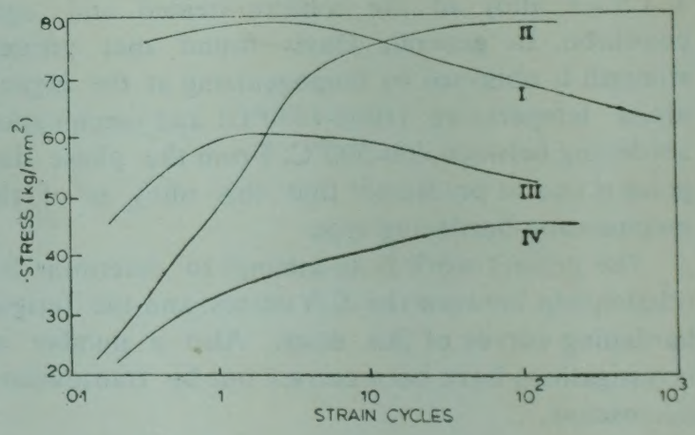

Fig. 4—Stress range versus strain cycles for Cu-0·75% Cr alloy with various treatments [Numbers I-IV on the different curves refer to the sample treatment as defined in Table 1]

behaviour of specimen II as influenced by annealing at 400°C for one day is quite distinct. It is observed that rapid hardening occurs during the early cycles of the process, followed by cyclic strain hardening rate approaching zero; this has been termed the 'saturation state'. Either strain hardening or strain softening can occur in the twisted specimen III. There is a slight hardening at the lowest strain range. Within the stress values tested, hardening appears to

be related more closely to the number of cycles than to the applied stress (cf. curve IV). The pre-annealed specimen IV hardens rather significantly while the twisted specimen III undergoes a prior strain hardening followed with softening until the two curves coincide. The annealed alloy is particularly interesting in view of the fact that it has reduced substantially the fracture ductility which does not appear to have a significant effect on its resistance to cyclic strain.

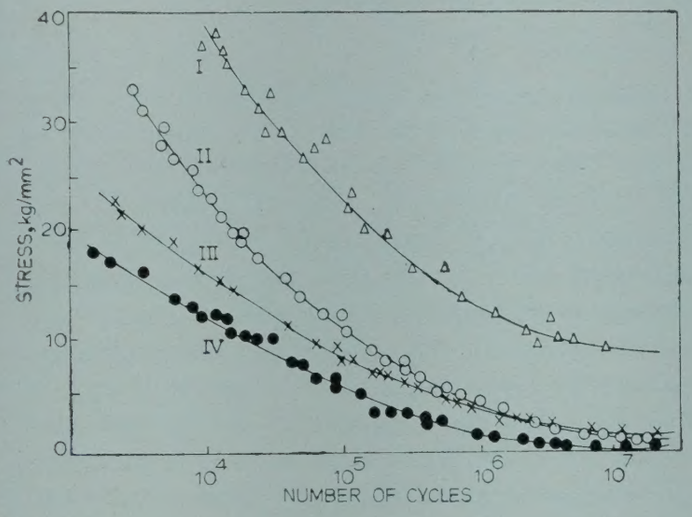

Fig. 5—Fatigue curves of Cu-0·75 Cr alloy at various treatment [Legend same as in Fig 4]

The fatigue characteristics are given in Fig. 5. Typical curves show the amount of strain hardening in course of fatigue for Cu-0·75% Cr alloy for various treatments. This alloy shows a knee between 10^6 and 10^7 cycles; in this case it can be said that a fatigue limit exists.[6] The present results in Cu-Cr alloy appear to be in good agreement with those of Cotteell,[7] if the difference in grain size is properly taken into account. The data suggest the complicated nature of the fracture behaviour of this material, not observed generally.

3.2 Transmission Electron Microscopy

Fig. 6 shows transmission electron micrographs of Cu-Cr alloy subjected to various treatments. In Fig. 6 (a) no precipitation was detected in specimen I, while in Fig. 6 (b) fine precipitation resulted; some of the particles thus precipitated formed strain fields but a large number of particles showed no strain fields. In Fig. 6 (c) for Cu-Cr alloy III, local precipitation occurred. Elastic strain field caused by the precipitation of fully coherent particles was observed in Fig. 6 (d); grain growth occurred in the matrix at

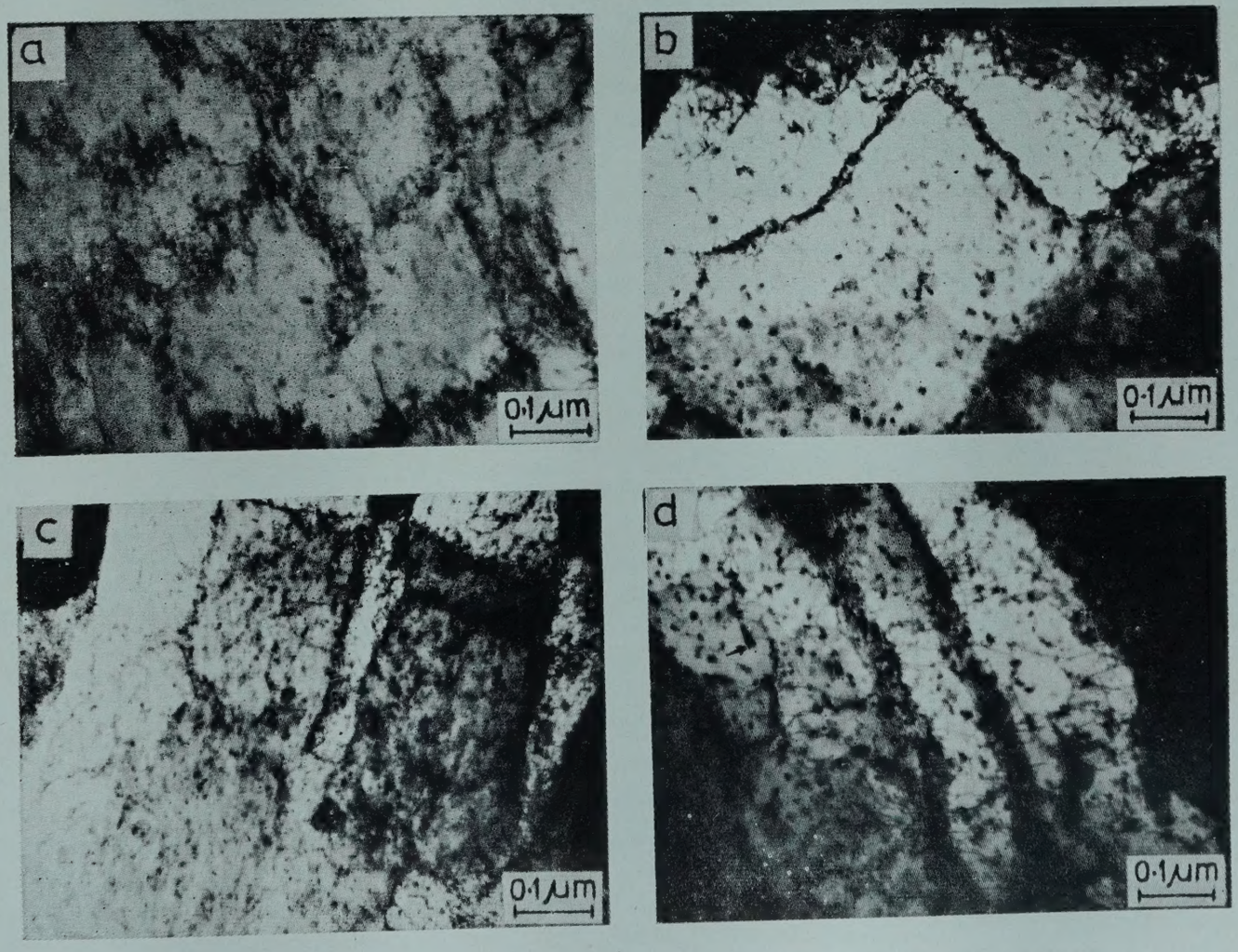

Fig. 6—Transmission electron micrographs of Cu-Cr alloy with different treatments

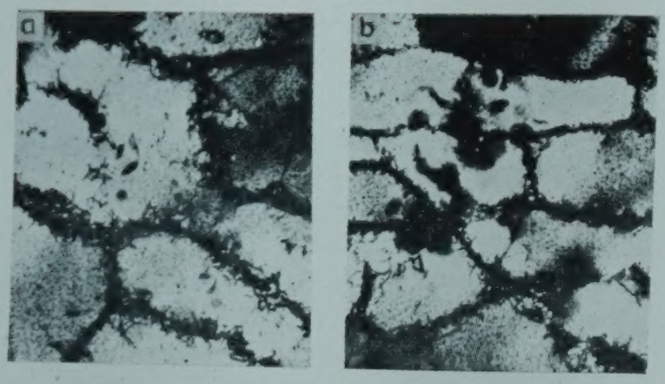

Fig. 7—Stereo photographs showing a general arrangement of fatigue striations (1×0000)

Fig. 8—Initiation and propagation of fatigued cracks in a crystallographic plane

this heat-treatment. The twisted pre-annealed specimen IV produced a coarse-grained matrix with a growth of precipitate particles indicated by the arrow in Fig. 6 (d) which indicates a higher density than in specimen III or II. While Nishikama and his coworkers[8] stated that particle contrasts in Cu-Cr alloy closely resembled those in Cu-Co alloy, the contrasts in the Cu-Cr alloy in this study are different from the coherent spherical particles in Cu-Co alloy. The electron diffraction analysis did not show any pure Cr and the crystal structure of the precipitates could not be determined. For a fatigued specimen of Cu-0·75% Cr alloy, a very distinctive pattern of dislocations was observed to be associated with fatigue striations (Fig. 7) which is discussed as a cell structure. Fig. 8 shows the formation and propagation of fatigued cracks in Cu Cr alloy. With this alloy, cracks were developed at the highest values of cyclic stress.

4. Conclusion

In the present Cu-0·75% Cr alloy, it was found that the strain hardening and the strain softening can take place. The deformation and fracture characteristics of this alloy with different treatments and subjected to fully reversed cyclic strain have been investigated. It is found that the strain-hardening behaviour of this alloy can be predicted from stress-strain characteristic; but some of the effects observed are unique to cyclic strain. The strain softening of certain specimens has been studied and it has been observed that cyclic strain tends to remove the effect of prior deformation. The fatigue curves show that the stress range remains unchanged at about 10^6 cycles. It is concluded that the fatigue limit is to be a property of the structure itself and not an ageing effect.

Transmission electron micrographs show no precipitation in non-annealed alloys, but the effect of precipitates in annealed specimens is detected. The cell structures are the general dislocation arrangements in cell walls at fatigue striation. The formation of a fatigue cracks and its propagation are observed.

References

1. Hibbard W R & Hoit E W, *J. Metals*, 7 (1955), 200.
2. Corson M G, *Trans. Am. Inst. Mining Metall. Engrs.* 77 (1927), 435; *Revue de Metallurgie*, 27 (1930), 93.
3. Davis C H, *Wire and Wire Prod.*, 13 (1938), 565.
4. Hanson M, *Constitution of binary alloys* (McGraw-Hill, New York), 1958, 524, 655.
5. Kelly P M & Natting J, *J. Iron Steel Inst.*, 192 (1959), 246.
6. Ferro A & Montalenli G, *Phil. Mag.*, 10 (1964), 1043.
7. Cotteell A H, *Trans. Metall. Soc.*, 212 (1950), 192.
8. Nishikawa S, Osada K & Kaboyashi S, *J. Japan Inst. Metals*, 30 (1966), 302, 760.

Indian Journal of Pure & Applied Physics
Vol. 18, June 1980, pp. 387-391

Electrical Conduction & Isothermal Dielectric Relaxation in Perspex

MALINI VARIYAR, M L KHARE & C S BHATNAGAR
Department of Physics, Maulana Azad College of Technology, Bhopal 462 007

Received 27 *April* 1979; *revised received* 15 *October* 1979

A study of isothermal current (I) as a function of time, voltage (V), temperature (T) and thickness has been made on perspex. The I-V curves show a low field and a high field behaviour. It is observed that trap-assisted space charge injection is responsible for the non-ohmic current in the low field region while space charge limited current governs the high field region. The I-T characteristics on the other hand have been interpreted using the cathodic depletion region approach. Values of activation energy, trap density, dielectric constant, mobility of carriers, difference in the metal-insulator work function ($\phi_m - \phi_i$), the energy difference between the bottom of conduction band and Fermi level and width of the depletion region for zero and different applied voltages have been computed from the above studies.

1. Introduction

In order to understand the electrical properties of polymers it is necessary to characterize the material by determining as many properties as possible by independent experimental methods and to relate them to molecular parameters. Moreover, localized impurity states are distributed throughout a dielectric[1,2] and the performance of a device made of these dielectrics depends on the trap parameters of the impurities.[3-6] Many non-steady state methods are available for the measurement of these parameters among which the method based on isothermal dielectric relaxation is attractive, because of its experimental simplicity.

The present investigation of electrical conduction in perspex coupled with time variation of current (that is isothermal dielectric relaxation) has been undertaken with a view to understanding the mechanism responsible for the electrical conduction in this dielectric.

2. Experimental Details

In order to study the dependence of current on sample thickness, voltage and time, a series of samples ranging from 1 to 5 mm in thickness and of 1·1 cm diameter were cut from perspex sheets. The current measurements were made with the sample mounted in a holder similar to that described elsewhere.[7] The temperature of the sample was controlled by keeping the electrode assembly in a thermostat. The thermostat used in the present case was a tempo oven which due to its specially constructed body ensured thermal insulation from atmosphere. The sample was heated to the required elevated temperature and the readings taken with the sample intact in the thermostat enclosure. As it is necessary to ensure thermal equilibrium in the specimen at the instant of measuring the current, a sufficiently long time was allowed to elapse before reading the current. Currents were measured using Philips dc microvoltmeter (type PP 9004) by varying the field in equal steps from 0·5 to 5 kV/cm at the desired temperature. Variation of current with field was observed at different constant temperatures of 80, 100, 120 and 140°C.

For the measurement of $I(t)$ the sample was heated as above to the desired temperature. A fixed initial field ranging from 10 to 25 kV/cm was then applied and the current measured at intervals of 5 min till the steady state was attained.

3. Results, Analysis and Discussion

Typical current-voltage (I-V) curves at different temperatures are shown in Fig. 1. They possess the general characteristics predicted by Rose-Lampert[8,9] theory, that is, an increase in current with temperature and applied voltage. The I-V curves seem to be divided into two parts each with a distinct characteristic behaviour.

In all cases, except at room temperature, the current increases much more rapidly with applied voltage in the low field region than it does in the high field region. However, in both the regions power-law variation ($I \propto V^n$) is apparent, the value of power n being more in the low field region as compared to high field. The power n also increases with temperature in the low field region (Fig. 1). Further, the voltage at which transition from low field to high field behaviour takes place also depends on temperature. The transition voltage is found to shift to

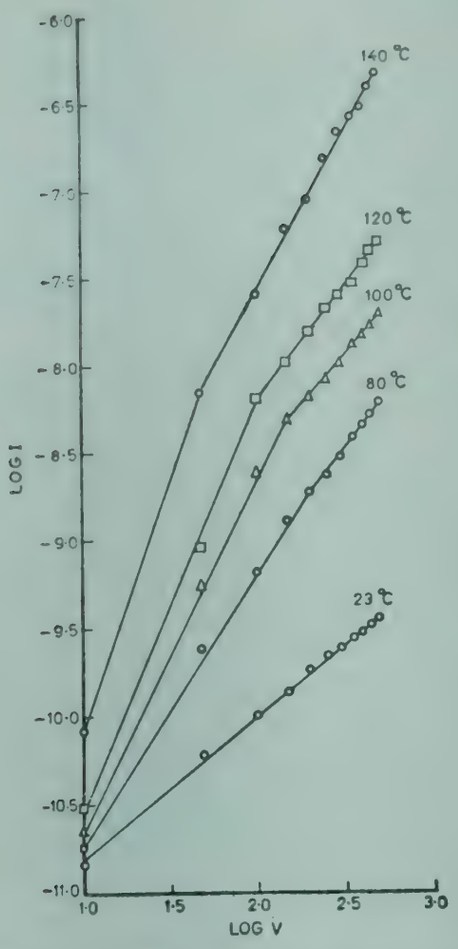

Fig. 1—Plot of Log I versus Log V at different temperatures

the lower voltage side as the temperature of the specimen increases.

Variation of current with voltage for samples of different thicknesses is shown in Fig. 2. The general characteristics remaining the same the current is found to increase with thickness. Fig. 3 shows $I(t)$ at different temperatures for different initially applied fields. The current is found to vary initially with time after which it attains the steady state.

Fig. 4 is a schematic energy level diagram of a Metal-Insulator-Metal (MIM) system showing the depletion region, and the variation of field corresponding to an applied voltage with distance within the sample.

On the basis of these experimentally observed facts, values of ϵ_r, $\phi_m - \phi_i$, N_t, E_{CT}, E_{CF}, λ_0, λ_v, Q and mobility of the carriers have been computed using the expressions mentioned and discussed in the following and the results are given in Tables 1 and 2.

In an MIM system, the electrode work function ϕ_m will be different from the insulator work function ϕ_i. Appyling the electrodes will, therefore, result in a transfer of charges between the electrode and the insulator until the two Fermi levels line up.[10,11]

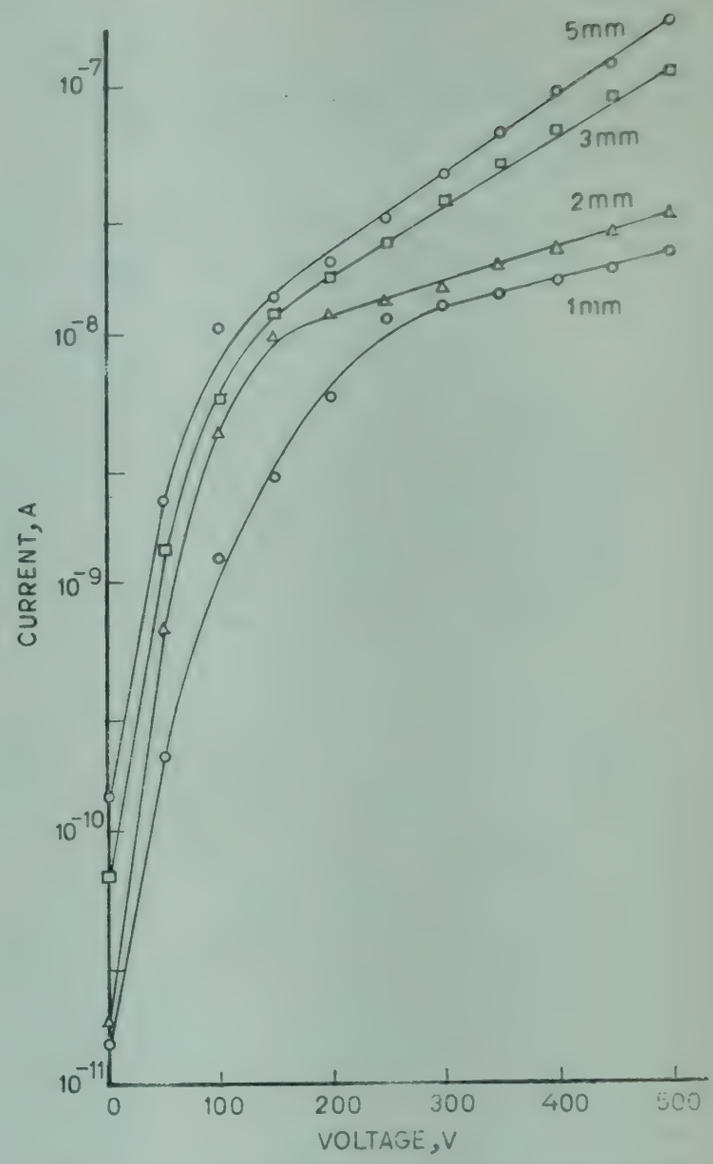

Fig. 2—Variation of current with voltage for samples of different thicknesses

This local variation of the potential known as 'band bending' causes the formation of Schottky barriers at both the surfaces. The width of this Schottky barrier depletion region is then given by the expression[11]

$$\lambda_0 = (2\epsilon/q^2 N_t)^{1/2} (\phi_m - \phi_i)^{1/2} \quad .. (1)$$

On applying a voltage to this junction, a current flows in the system and the width of the depletion region for this applied voltage takes the form

$$\lambda_v = (2\epsilon/q^2 N_t)^{1/2} (\phi_m - \phi_i + q v) \quad .. (2)$$

This applied field, however, is not uniform throughout the insulator. It changes with the distance from the metal-insulator interface. The rate of change of potential V as a function of the distance x from the interface can be written as follows in units of V/cm :

$$\frac{dv(x)}{dx} = \frac{N_t q}{\epsilon_r}\left[\left\{\frac{2\epsilon_r (ev + \phi_m - \phi_i)}{N_t q^2}\right\}^{1/2} - x\right] \quad .. (3)$$

Thus though a constant voltage is applied across the structure, the bulk field does not remain constant throughout. It varies with distance from the interface and also with time. At time $t = 0$ the voltage across the contacts is zero as initially the entire voltage is uniformly distributed across the insulator and hence the current at any time t in terms of the initial current can be shown to be[12]

$$(J_i\, t) = J_i\,(0)\left(\frac{V_i - V_c\,(t)}{V_i}\right) \exp - \left\{\left(\frac{2\beta}{kT}\right)\left(\frac{1}{L}\right)^{1/2}\right\} \left[V_i^{1/2} - \left\{ V_i - V_c\,(t)\right\}^{1/2} \right] \qquad ...(4)$$

where $2\beta\,(V_i/L)^{1/2}$ represents the field lowering of the trap levels, β being given by $(q^3/4\,\pi\,\epsilon_r)^{1/2}$ and $J_i(t)$ represents the steady state current density.

Dielectric constant is evaluated using the expression obtained on solving the initial currents for two applied voltages simultaneously. It takes the form

$$\epsilon_r = 7\,735\times 10^9\left(\frac{V_{i2}^{1/2} - V_{i1}^{1/2}}{L\,T^2}\right)^2 \left(\ln \frac{J_{i2}\,(0)\,V_{i1}}{J_{i1}\,(0)\,V_{i2}}\right)^{-2} \qquad ...(5)$$

By plotting the $I\,(t)$ characteristics for two applied voltages, the charges collected in these two cases can be known in the usual way.[13] Then using the depletion region approach and solving the equation for Q_1 and Q_2, the expression for trap density and $\phi_m - \phi_i$ can be written as

$$f_t\, N_t = \frac{1}{A^2}\,\frac{1}{2\epsilon}\,\frac{Q\,(1)\,Q\,(2)\,[Q\,(1) - Q\,(2)]}{Q\,(2)\,eV_1 - Q\,(1)\,eV_2} \qquad ...(6)$$

and

$$(\phi_m - \phi_i)^{1/2} = \frac{(2\epsilon\, f_t\, N_t)^{1/2}\, A\, q\, V_{c1}}{2\,Q\,(1)} - \frac{Q\,(1)}{2\,(2\epsilon f_t\, N_t)^{1/2}\, A} \qquad ...(7)$$

The observed current in an MIM structure at any time is essentially the bulk limited current, and therefore, the Poole-Frenkel effect is mainly responsible for the conduction in the structure. The bulk current density at any time is

$$J_i\,(t) = q\,\mu\, N_c\, F_i\,(t) \exp\left[\frac{2\beta\, F_i^{1/2} - E_{cF}}{k\,T}\right] \qquad ...(8)$$

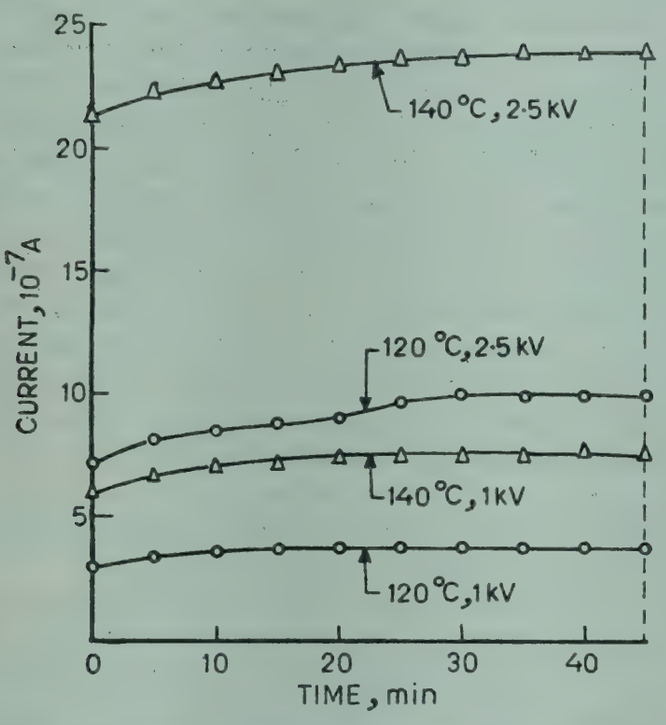

Fig. 3—Variation of current with time after the application of a fixed initial voltage

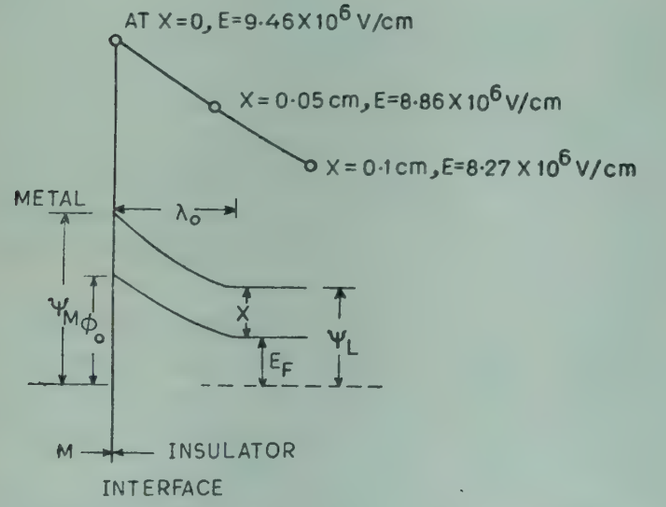

Fig. 4—Schematic representation of the energy level diagram for an MIM structure

Table 1—Values of Dielectric Constant, Charge, $\phi_m - \phi_i$ Trap Density, λ_0 Depletion Region for Zero Bias λ_0 and Mobility (γ) of the Carriers for Samples at Different Temperatures

Temp. °C	Dielectric constant	Charge (in coul) in depletion region for applied voltage		$\phi_m - \phi_i$ eV	Trap density cm^{-3}	λ_0 Å	μ $cm^2/V/sec$
		2·5 kV	1·0 kV				
80	1·291	$1{\cdot}702\times10^{-4}$	$7{\cdot}350\times10^{-5}$	0·01	$4{\cdot}515\times10^{16}$	199·4	0·1016
100	1·5924	$6{\cdot}460\times10^{-4}$	$2{\cdot}917\times10^{-4}$	0·02	$8{\cdot}790\times10^{16}$	224·3	1·188
120	1·9119	$2{\cdot}475\times10^{-3}$	$9{\cdot}750\times10^{-4}$	0·13	1.615×10^{17}	461·3	4·893
140	2·5122	$6{\cdot}265\times10^{-3}$	$1{\cdot}95\times10^{-3}$	0·25	$4{\cdot}037\times10^{17}$	464·5	40·93

Table 2—Values of the Field F_i at the Metal-Insulator Interface, Width of the Depletion Region λ_v, E_{CF} and Activation Energy for Different Applied Voltages

Applied voltage kV	F_i V/cm	λ_v cm	E_{CF} eV
1·0	$9·459\times10^{6}$	$2·939\times10^{-4}$	0·8290
1·5	$11·58\times10^{6}$	$3·599\times10^{-3}$	1·104
2·0	$13·38\times10^{6}$	$4·158\times10^{-3}$	1·129
2·5	$14·96\times10^{6}$	$4·645\times10^{-3}$	1·201

Voltage	Activation energy for SCLC eV
350	0·6102
400	0·6122
450	0·6310
500	0·6310

From Eq. (8) it is inferred that the slope of the initial current density versus absolute temperature curve at a constant applied voltage will yield $2\beta F_i^{1/2}-E_{eF}$ which will eventually give E_{cF} the energy of the bottom of conduction band with respect to Fermi level.

An abrupt increase in current with applied voltage unlike an expected ohmic behaviour seems to suggest that the current in this case is carried by the charges (electrons) injected from the electrodes.

Some of the injected electrons are trapped in the trapping centres within the dielectric; so the current in the low field region is trap limited. This goes on until, with increasing number of injected electrons which increase with applied voltage, the traps gradually fill up, and a trap-filled limit is reached. This refers to the highest current in the low field region.

At this stage the injected carriers start a limiting process at the surface and the conduction becomes space charge limited. This transition from trap-limited to space charge-limited conduction takes place at lower voltages as the temperature increases. This is so because at a higher temperature a smaller fraction of the total injected charge at each applied potential is trapped, consequently the space charge tends to limit the current at a lower voltage.

The observed increase in current with temperature may be partly due to thermal activation and partly due to increase in mobility. The increase in mobility with temperature is clear from Table 1. The increase in current with thickness is due to increased number of charge carriers in thick samples.

The results presented in Fig. 3 may be understood as follows. When a voltage is applied across an MIM structure, initially the entire voltage is uniformly distributed across the insulator and very little voltage appears across the contacts. This is the non-steady state. The current in this condition corresponds to the field due to the entire voltage across the bulk of the insulator. In this state, the current due to the bulk-limited processes is not the same as that due to electrode-limited processes at the interface, the bulk current being much higher than the contact current. This tends to the formation of a depletion region near the interface which, in turn, modifies the electrical field until the current is uniform throughout the structure. In this condition, the potential across the insulator becomes very small compared to its initial value, and most of the potential appears across the cathode metal-insulator contact. This gives rise to the steady state.

Before steady state is reached, the rate of positive charge accumulation (due to electron migration) in cathodic depletion region is equal to the difference between the bulk and contact currents. The charge accumulated in this region becomes constant when steady state is reached. This charge increases with temperature as shown in Table 1. The cathodic depletion region depends on $(\phi_m-\phi_i+qV)$ (Ref. 14). As the temperature is increased, the Fermi level of insulator (with donor impurities) shifts down towards the middle of valence and conduction bands. Due to this, $(\phi_m-\phi_i)$ increases as is clear from Table 1. Increase in $(\phi_m-\phi_i)$ causes greater band bending at the interface, which is associated with greater charge accumulation.

In perspex, there are several types of thermally stimulated motions of different sized parts of the molecular chain segments and groups, due to the loosening of the bonds. This causes an increase in dielectric constant at higher temperatures.

Increase in trap density with temperature is understandable in terms of an increase in imperfections within the structure.

Acknowledgement

The authors are thankful to the Principal, M A College of Technology, Bhopal, for the facilities provided. They are also thankful to the National Science Foundation, USA, for providing necessary equipments. One of the authors (MV) is thankful to the Government of India, Ministry of Education and Social Welfare, New Delhi, for awarding a Research Training Scholarship to her.

References

1. Bube R H, *Photoconductivity of solids* (Wiley, New York), 1960.
2. Mott N F, *Adv. Phys.*, 16 (1967), 49.
3. Lamb D R, *Electrical conduction mechanism in thin insulating films* (Methuen, London), 1967.
4. Simmons J G, *Phys. Rev.*, 166 (1968), 912.
5. Pollack S R & Seitchik J A, *Appl. Solid St. Sci.*, 1 (1969), 343.
6. Gupta H M & Van Overstaeten R J, *J. appl. Phys.*, 46 (1975), 2675.
7. Verma D & Bhatnagar C S, *Indian J. pure appl. Phys.*, 14 (1976), 93.
8. Rose A, *Phys. Rev.*, 97 (1955), 1538.
9. Lampert M A, *Phys. Rev.*, 103 (1956), 1648.
10. Simmons J G & Taylor D W, *Phys. Rev.*, B6 (1972), 4793.
11. Henisch H K, *Rectifying semiconductor contacts* (Oxford University Press, London), 1957.
12. Gupta H M, *J. appl. Phys.*, 48 (1977), 3448.
13. Nadkarni G S & Simmons J G, *Phys. Rev.*, B7 (1973), 3719.
14. Azaroff L V & Brophy J J, *Electronic processes in materials* (McGraw Hill-Kogakusha Ltd., Tokyo), International Student Edn., 1963, 231.

Indian Journal of Pure & Applied Physics
Vol. 18, June 1980, pp. 392-395

Relationship between Potential Energy Constants & Heat of Atomization

G THYAGARAJAN & M K SUBHEDAR
Department of Physics, Indian Institute of Technology, Bombay 400 076

Received 19 *March* 1979

Relations between the force constants and heats of atomization have been deduced for polyatomic molecules of planar XYZ, planar and pyramidal XYZ_2 and pyramidal XYZ_3 types by employing an approximately separable potential function for the molecules and using specific functional forms for the bonded and non-bonded interactions. To test the validity of the relations deduced, heats of atomization have been calculated from the available force constants data for some molecules and fair agreement between the observed and calculated values (of heats of atomization) is noticed.

1. Introduction

For an exact evaluation of the force constants of a polyatomic molecule, vibrational frequency data alone are often inadequate.[1] Additional relations connecting the force constants with other parameters such as the Coriolis coupling coefficients, the centrifugal stretching constants, etc. can be employed to solve the problem, but the usefulness of these relations is limited by the scanty data available on these parameters.

Lippincott and Schroeder[2] had earlier deduced a relationship between the bond stretching force constant and the bond dissociation energy rather than the bond energy which is more readily available. Later, Thyagarajan *et al.*[3] obtained a relationship between force constant and bond energy for XY_n type of polyatomic molecules having similar X—Y bonds.

In the present work, it has been shown how the force constants can be related to the heat of atomization of a polyatomic molecule having dissimilar bonds such as XYZ, XYZ_2 and XYZ_3. Heat of atomization is one of the most extensively and fairly accurately known parameters and is more readily available.

2. Theory

The process of atomization, as defined by Szwarc and Evans[4] is one in which all the bonds are stretched to infinity while keeping the initial shape of the molecule unchanged.

The steps involved in the present problem are (i) to write down an analytical expression for the potential energy of a molecule for all arbitrary configurations of the molecule, (ii) to deduce the heat of atomization of the molecule ΔH_a^0 as the limiting value of the potential function (1) when all bonds are stretched to infinity, and (iii) to write the relationship between ΔH_a^0 and the potential energy constants.

Let us consider the above steps briefly. Detailed discussion is available in Ref. 3.

Step (i)—The total potential energy for an arbitrary configuration of a molecule having t bonds with lengths indicated by r, m bond angles indicated by α, and p non-bonded distances indicated by q, can be written symbolically as $V(r_1 \ldots r_t, \alpha_1 \ldots \alpha_m; q_1 \ldots q_p)$. Since the analytical form of this energy function is not known for any polyatomic molecule, a reasonable approximation, viz. that this function is separable in terms of distinct sets of internal coordinates, is made, i.e.

$$V(r_1 \ldots r_t; \alpha_1 \ldots \alpha_m; q_1 \ldots q_p) = V(r_1, \ldots r_t) + V(\alpha_1, \ldots \alpha_m) + V(q_1, \ldots q_p) \quad \ldots (1)$$

Further it is assumed that

$$V(r_1 \ldots r_t) = \sum_{i=1}^{t} V(r_i) + \sum_{i>j}^{t} \sum_{j=1}^{t-1} V(r_i, r_j) \quad \ldots (2)$$

and

$$V(q_1 \ldots q_p) = \sum_{k=1}^{p} V(q_k) \quad \ldots (3)$$

The Lippincott-Schroeder potential function and its generalized form is used to represent the functions $V(r_i)$ and $V(r_i, r_j)$ respectively.

A number of functions have been proposed to represent the non-bonded interaction potential $V(q_k)$ in Eq. (3), depending on whether the atoms involved are both hydrogen or not.

Step (ii)—In order to study the functions near the atomization process, we need the limiting form of

Eq. (1), as all bonds are stretched to infinity. At equilibrium configuration, the value of each part of the energy in Eq. (1) is taken to be zero. Then the heat of atomization is given by

$$\Delta H_a^0 = \underset{\text{all } r\to\infty}{\text{Lt}} V(r_1 \ldots r_t) + \underset{\text{all } r\to\infty}{\text{Lt}} V(\alpha_1 \ldots \alpha_m) + \underset{\text{all } r\to\infty}{\text{Lt}} V(q_1 \ldots q_\mu) \quad \ldots(4)$$

The constancy of the bond angles, throughout the atomization process, leads to zero contribution from the angular part of the potential energy. Also the non-bonded part, can, in the limit, as all $r\to\infty$, be written as

$$\sum_{k=1}^{\mu} V_\infty (q_k).$$

It has been shown in the earlier work,[3] that contribution from $V_\infty (q_k)$ for all other atoms, except those containing hydrogen atoms, is negligible compared to that from the bonded atoms.

Substitution of the above limiting values into Eq. (4), leads to

$$\Delta H_a^0 = \sum_{i=1}^{t} D_{ii} + \sum_{i>j} D_{ij} + \sum_k V_\infty (q_k) \quad \ldots(5)$$

where D's are the bond energies.

Step (iii)—The relation between ΔH_a^0 and force constants is obtained by expanding $V(r_1 \ldots r_t)$ in Taylor series. By comparing the terms in the above expansion with the corresponding terms in the expansion of $V(r_1 \ldots r_t)$ using GVFF notation and then substituting for D_{ii} and D_{ij} in Eq. (5), we get

$$\Delta H_a^0 = \sum_i \frac{(r_i)_e}{n_i} f_{r_i} + \sum_{i>j} 2 \left\{ \frac{(r_i)_e (r_j)_e}{n_i n_j} \right\}^{1/2} f_{r_i} f_{r_j} + \sum_k V_\infty (q_k) \quad \ldots(6)$$

Here n_i and n_j are the Lippincott parameters. Eq. (6) is the working equation for the relationship between ΔH_a^0 and force constants.

It should be pointed out here that anharmonicity effects should be included in the above equation so that the potential function truly corresponds to the region near dissociation. As these effects are not known for almost all polyatomic molecules, the force constants may, at best, be corrected for anharmonicity in the way Lippincott and Schroeder[2] have done, (i.e. an increase of 8% in the case of bonds containing hydrogen and 3% in others), after studying large number of molecules.

The expression is modified depending on the type of molecules considered here, viz. XYZ, XYZ_2 and XYZ_3

Planar XYZ

$$\Delta H_a^0 = \left(\frac{r_e}{n}\right)_r f_r + \left(\frac{r_e}{n}\right)_R f_R + 2 \left(\frac{r_e}{n}\right)_r^{1/2} \left(\frac{r_e}{n}\right)_R^{1/2} f_{rR} + V_\infty (q_k) \quad \ldots(7)$$

The subscripts r and R refer to the values of (r_e/n) for the respective bonds and n is the Lippincott parameter for the bond in question.

Planar XYZ_2

$$\Delta H_a^0 = \left(\frac{r_e}{n}\right)_r f_r + 2 \left(\frac{r_e}{n}\right)_R \left(f_R + f_{RR}\right) + 4 \left(\frac{r_e}{n}\right)_r^{1/2} \left(\frac{r_e}{n}\right)_R^{1/2} f_{rR} + \sum_{k=1}^{3} V_\infty (q_k) \quad \ldots(8)$$

Pyramidal XYZ_3

Same expression as Eq. (8)

Pyramidal XYZ_3

$$\Delta H_a^0 = \left(\frac{r_e}{n}\right)_r f_r + 3 \left(\frac{r_e}{n}\right)_R \left(f_R + 2f_{RR}\right) + 6 \left(\frac{r_e}{n}\right)_r^{1/2} \left(\frac{r_e}{n}\right)_R^{1/2} f_{rR} + 6 \sum_k V_\infty (q_k) \quad \ldots(9)$$

In Eqs. (7), (8) and (9)
r = X—Y bond distance; R = Y—Z bond distance; and q = X—Z non-bonded distance.

It may be mentioned that in Eqs. (7) to (9) the symmetry force constants F_{11}, F_{22} and F_{12} of the totally symmetric species (a species) may be used in place of f_r, $f_R + f_{RR}$, $f_R + 2f_{RR}$, f_{rR}, etc. as the case may be. There is no need to know f_R and f_{RR} separately.

It may also be noted that consistent with the definition of the atomization process, it is the set of force constants of the totally symmetric species, when the bonds stretch in phase, which appear in the relations obtained.

Experimental values of heats of atomization are usually expressed in kcal/mole. If force constants are expressed in mdyne/Å, the right hand side of all the above Eqs. (7), (8) and (9) should be multiplied by a factor of 144·2 in order to express ΔH_a^0 in kcal/mole.

Table 1—Comparison of Theoretical Values of ΔH_a^0 Obtained Using Eqs. (7)-(9) with Experimental Values for Different Types of Molecules

Molecule	F_{11}	F_{22}	f_{rR}	ΔH_a^0, kcal/mole Theo.	ΔH_a^0, kcal/mole Exptl	References for force constants
Planar XYZ Molecule [Eq. (7)]						
HOCl	7·94	3·65	0·62	196·1	169·5	9
ONCl	14·94	1·48	−1·13	144·4	189·1	10
ONCl	15·37	2·26	0·13	194·8	189·1	11
ONCl	15·72	1·31	1·58	219·7	189·1	12
ONF	15·53	2·15	1·91	218·2	207·3	13
ONF	15·93	2·22	2·24	230·6	207·3	12
ONBr	15·25	1·13	1·47	212·4	179·7	12
ONBr	14·83	1·34	−1·03	144·12	179·7	11
OOH	6·65	6·73	0·0	176·5	166·2	14
OOF	1·47	10·80	0·0	136·9	135·0±5	15
FCO	4·69	13·20	0·0	209·0	290·3±15	16
ClCO	1·58	14·71	0·0	199·1	274·4±10	17
HCO	3·59	14·77	0·0	240·3	286·8	18
Planar XYZ_2 Molecule [Eq (8)]						
OCF_2	14·22	7·42	1·20	395·0	420·9	19
OCF_2	12·50	7·35	0·71	348·7	420·9	19
OCF_2	12·50	8·55	0·37	361·6	420·9	19
$OCCl_2$	13·54	4·61	0·21	327·2	340·8	19
$OCCl_2$	13·47	3·93	0·52	320·7	340·8	19
$OCBr_2$	13·77	3·44	0·10	296·0	306·9	19
$OCBr_2$	13·66	2·99	0·10	276·9	306·9	19
OCH_2	13·39	5·57	1·23	447·0	362·4±1·5	20
OCH_2	13·18	4·76	0·78	387·4	362·4±1·5	20
FNO_2	2·74	13·12	0·0	308·5	225·0	21
$ClNO_2$	2·53	12·36	0·0	300·8	258·0	21
$ClNO_2$	1·90	9·02	0·0	220·3	258 0	21
ClF_3	3·74	4·06	0·47	182·3	123·5	22
BrF_3	3·75	4·17	0·41	183·6	144·4	23
$BBrCl_2$	3·04	4·88	0·71	317·4	297·7±14	24
$BClBr_2$	3·39	3·14	0·63	250·7	280·0±14	24
$BClF_2$	3·39	6·89	0·87	307·2	410·8±9	24
$BFCl_2$	7·36	3·66	1·26	326·2	363·3±9	24
$BFBr_2$	7·36	3·21	0·58	270·5	327·9±14	24
Pyramidal XYZ_2 Molecule [Eq. (8)]						
$ClNF_2$	3·22	5·14	0·0	156·1	176·4±3	25
$ClNF_2$	4·09	6·18	0·70	225·7	176·4±3	25
OSF_2	11·59	5·85	1·33	408·3	297·9±10	27
OSF_2	11·33	3·88	0·14	280·9	297·9±10	28
$OSCl_2$	9·83	4·27	0·62	366·2	233·8	27
$OSCl_2$	9·36	1·85	0·48	249·2	233·8	28
$OSBr_2$	8·64	2·43	0·46	267·8	200·5	27
$OSBr_2$	8·03	0·66	0·36	217·3	200·5	28
$FClO_2$	2·61	9·22	0·0	276·1	—	29
$OSeF_2$	7·24	1·98	0·0	197·0	172·8	30
$OSeF_2$	8·35	4·24	0·30	267·3	—	31
$NFCl_2$	4·34	3·54	0·0	141·5	—	25
$NFCl_2$	3·31	2·76	0·28	122·9	—	32
$NFCl_2$	3·83	3·63	0·54	164·6	—	26
Tetrahedral XYZ_3 Molecule [Eq. (9)]						
POF_3	12·19	7·64	0·09	496·1	481·1	33
POF_3	10·19	6·80	0·52	468·2	481·1	34
POF_3	11·28	6·50	0·48	469·1	481·1	35
$POCl_3$	10·69	2·64	0·27	341·7	355·8	35
$POCl_3$	10·37	3·61	0·05	373·1	355·8	33
$POBr_3$	10·02	3·40	0·02	362·8	324·8	33
CH_3F	6·37	5·86	−0·71	359·0	383·2±7	38
CH_3Cl	3·50	2·75	−0·05	396·3	375·4	36
CH_3Cl	4·00	6·08	−0·84	337·0	375·4	38
CH_3Br	2·98	5·81	−0·01	402·1	362·3	36
CH_3Br	3·21	5·93	−0·71	333·4	362·3	38
CH_3I	2·39	5·75	−0·09	384·6	349·6	36
CH_3I	2·39	5·78	−0·30	360·4	349·6	38
CHF_3	5·29	8·35	0·18	411·0	444·0	37
$CHCl_3$	5·32	4·51	0·08	348·1	334·4	37
$CHBr_3$	5·35	4·30	0·06	345·0	299·2	27
ONF_3	14·16	5·58	0·66	370·1	268·1	26
SiH_3F	5·73	3·08	0·001	355·4	388·5±15	33
SiH_3Cl	3·11	3·07	0·002	335·8	341·6±15	33
$SiHF_3$	3·16	7·13	−0·003	424·5	500·0±15	33
$SiHCl_2$	3·01	3·68	0·01	340·5	366·8	33

3. Results and Discussion

In Table 1, the values of ΔH_a^0 obtained using Eqs. (7), (8) and (9) for some planar XYZ, planar XYZ_2, pyramidal XXZ_2 and pyramidal XYZ_3 are compared with the experimental values. In Table 1, the force constants were corrected for anharmonicity as mentioned earlier. Further, the contribution to the non-bonded part V_∞ (q) has been added in the case of molecules containing hydrogen atoms, where they are significant, using the parameters given in Ref. 3. The Lippincott parameter n for bonds r and R is determined from the ionization potentials listed by Sargent.[5]

The agreement between the experimental and theoretical values of ΔH_a^0 may be considered very good, for a large number of molecules. The deviations, in some cases, may be a result of uncertainties in the force constants which are collected from different sources in the literature. Uncertainties in ΔH_a^0 (experimental) are not likely to be significant as the values reported by different investigators[6-8] for the same molecule often agree closely.

It may be noted that in the following cases, where two or three sets of force constants are available due to different investigators, ΔH_a^0 calculated using one of these sets agrees very well, while distinct differences are noticed when calculated with the other sets for the molecules : ONCl, ONF, ONBr, OCF_2, $OCCl_2$, $OCBr_2$, OCH_2 $ClNO_2$, $ClNF_3$, OSF_2, $OSCl_2$ $OSBr_2$, POF_3, $POCl_3$, CH_3Br and CH_3I. This indicates clearly how the heat of atomization can provide a sensitive test for the validity of the force constants obtained.

References

1. Wilson (Jr) E B, Decius J C & Cross P C, *Molecular vibrations* (McGraw-Hill, New York), 1955.
2. Lippincott E R & Schroeder R, *J. Am. chem. Soc.*, 78 (1956), 5171.
3. Thyagarajan G, Sarma C R & Subhedar M K, *J. molec. Spectrosc.*, 31 (1969), 100.
4. Szwarc M & Evans M G, *J. chem. Phys.*, 18 (1950), 618.
5. Sargent E H, Sargent and Co. Catlog No. 518806, Chicago, 1962.
6. National Bureau Standards (U S), Tech. Note 270-1, 1965.
7. National Bureau Standards (U S) JANAF Thermochemical Tables, 1971.
8. Dean J A, *Lange's handbook of chemistry*, (McGraw-Hill, New York), 11th Edn, 1973.
9. Venkateswarlu K & Mariam S, *Indian J. pure appl. Phys.*, 3 (1965), 117.
10. Mirri A M & Mazzariol E, *Spectrochim. Acta*, 22 (1966), 785.
11. Devlin J P & Hisatsune I C, *Spectrochim. Acta*, 17 (1961), 206.
12. Jones L H, Asprey L B & Ryan R R, *J. chem. Phys.*, 47 (1967), 3371; 49 (1968), 581.
13. Cook R L, *J. chem. Phys.*, 42 (1965), 2927.
14. Milligan D E & Jacox M E, *J. chem. Phys.*, 38 (1963), 2627.
15. Spratley R D, Turner J J & Pimental G C, *J. chem. Phys.*, 44 (1966), 2063.
16. Milligan D E, Jacox M E, Bass A M, Comford J J & Mann D E, *J. chem. Phys.*, 42 (1965), 3187.
17. Jacox M E & Milligan D E, *J. chem. Phys.*, 43 (1965), 866.
18. Milligan D E & Jacox M E., *J. chem. Phys.*, 41 (1964), 3032.
19. Beckmann L, Gutajahr L & Mecke R, *Spectrochim. Acta*, 20 (1964), 1295.
20. Curtis E C, *J. molec. Spectrosc.*, 14 (1964), 279.
21. Bernitt D L, Miller R H & Hisatsune I C, *Spectrochim. Acta*, 23 (1967), 237.
22. Ramaswamy K & Muthusubramanian P, *J. molec. Struct.*, 9 (1971), 173.
23. Selig H, Classen H H & Holloway J H, *J. chem. Phys.*, 52 (1970), 3517.
24. Ford T A & Orville-Thomas W J, 1967, *Spectrochim. Acta*, 23 (1967), 579.
25. Shanmugasundaram G & Nagarajan G, *Mh. Chem.*, (1970), 1309.
26. Ramaswamy K & Mohan N, *Z. Naturf.*, 25B (1970), 169.
27. Sambandam P T & Venkateswarlu K, *Z. phys. Chem.*, 218 (1961), 310.
28. Cotton F A & Horrocks (Jr) W D, *Spectrochim. Acta*, 16 (1960), 358.
29. Robinson E A, Lavery D S & Weller S, *Spectrochim. Acta*, 25A (1969), 151.
30. Paetzold R, *Z. Chem.*, 4 (1964), 272.
31. Pillai M G K & Parameswaran P P, *Z. Naturf.*, 25B (1970), 246.
32. Nair B S & Purushothaman C, *Curr. Sci.*, 38 (1969), 488.
33. Mueller A, Krebs B, Fadini A & Glemser O, *Z. Naturf.*, 23 (1968), 1656.
34. Ziomek J S & Piotrowski E A, *J. chem. Phys.*, 34 (1961), 1087.
35. Dogennette L, *J. Chim. Phys.*, 58 (1961), 487.
36. King W T, Mills I M & Crawford (Jr) Bryce, *J. chem. Phys.*, 27 (1957), 455.
37. Galasso V, De Alti G & Costa G, *Spectrochim. Acta*, 21 (1965), 669.
38. Subhedar M K, Ph D thesis, I I T, Bombay, 1977.

Indian Journal of Pure & Applied Physics
Vol. 18, June 1980, pp. 396-400

Interpretation of the Spectra of Substituted Borazines By Urey-Bradley Force Field

M K SUBHEDAR & G THYAGARAJAN

Department of Physics, Indian Institute of Technology, Bombay 400 076

Received 19 *March* 1979

A collective account of the Urey-Bradley force field (UBFF), for Borazine and several of its substituents is presented. The complete vibrational data for all the molecules have been examined together to form a consistent set of potential energy constants. The UBFF has been found to be quite reliable for these molecules in the present investigation.

1. Introduction

In an earlier paper[1] the Urey-Bradley force field analysis of the borazine molecule was reported. The data on the vibrational spectra of halide-substituted borazines and N-trimethyl borazine have now been given by Totani and Watanabe[2] and Anderson and Lagowski.[3] But no attempts have been made to assign these data in a systematic way. The present investigation aims at extending the Urey-Bradley method to the substituted borazines so that vibrational analysis will become definite in these cases. The Urey-Bradley force constants for borazine have been transferred to $X_3B_3N_3Y_3$ [where X = halogens and Y=hydrogen or X=hydrogen and Y=methyl group], with their deuterated analogues.

2. Results

The Urey-Bradley force constants transferred throughout and data on the structural parameters used are given in Table 1. The complete potential energy matrix for the molecules studied is given in Table 2. The potential energy constants for borazine which had to be modified (in Ref. 1) are also given in Table 2, along with others. The calculated frequencies are compared in Table 3, with the observed ones wherever available.

3. Discussion

The following observations may be made regarding the results obtained.

1. There is a significant contribution from the non-bonded interactions to the diagonal elements of the F matrix in both the a_1' and e' species, and in particular, to the BN ring force constants (viz. F_{33}, G_{77} and F_{88}) in all the molecules.

2. The BN ring-NY bond and the BN ring-BX bond, stretch interactions (viz. F_{13}, P_{23}, F_{57}, F_{58}, F_{67} and F_{68}), and the BN ring modes-NY bond interactions, (viz. $F_{7,10}$, $F_{8,10}$ and $F_{10,11}$) are more significant than other off-diagonal terms in every case. This systematic finding has not been made in the earlier investigations, where UBFF has not been attempted.

3. There is a good general agreement of calculated and observed frequencies, except the ring stretching vibrations ν_7 and ν_8 in the e' species where both are of the same order of magnitude, viz. between 1500 and 1400 cm^{-1}. It is quite possible that mutual interactions of these ring vibrations may be responsible for this and not easily accountable from the force field considered.

4. The B-X, stretching frequencies in e' species, in the B-halogenated compounds show a systematic trend in the variation, as they occur at 1171, 761, 673 and 559 cm^{-1}. They may be compared with the

Table 1—Structural Parameters for Substituted Borazines and the Urey-Bradley Force Constants (mdyne/Å) for Bonds and Angles Transferred Throughout

Bond distances in Å

B—H = 1·20 N—H = 1·02 B—F = 1·34 B—Cl = 1·754
B—Br = 1·87 B—I = 2·10 B—N = 1·44 N—C = 1·47

All bond angles were assumed to be 120°

$K_{BH} = 3{\cdot}3126$	$K_{NH} = 6{\cdot}165$	$L_{BH} = 0{\cdot}81$
$K_{BF} = 7{\cdot}0$	$K_{BN\ ring} = 4{\cdot}648$	$L_{BF} = 0{\cdot}30$
$K_{BCl} = 3{\cdot}6$	$L_{BN\ ring} = 4{\cdot}20$	$L_{BCl} = 0{\cdot}17$
$K_{BBr} = 3{\cdot}0$	$L_{NH} = 0{\cdot}35$	$L_{BBr} = 0{\cdot}04$
$K_{BI} = 1{\cdot}9$	$\frac{1}{2}(H_B + H_N) = 0{\cdot}447$	$L_{BI} = 0{\cdot}02$

Table 2—Symmetry Potential Energy Constants (mdyne Å) for Borazines

	$(NBNH)_3$	$(FBNH)_3$	$(ClBNH)_3$	$(BrBNH)_3$	$(IBNH)_3$	$[(HBN(CH_3)]_3$
			a_1' Species			
F_{11}	K_{BH} + 0·2426	K_{BF} + 0·3668	K_{BCl} + 0·4	K_{BBr} + 0·4276	K_{BI} + 0·4886	K_{BH} + 0·2396
	(3·5552)	(7·3668)	(4·0)	(3·4270)	(2·3886)	(3·5522)
F_{12}	0·0106	0·0212	0·0346	0·0394	0·0478	0·0082
F_{13}	0·3871	0·5861	0·5725	0·6027	0·6712	0·3814
F_{14}	−0·1290	−0·2097	−0·2372	−0·2572	−0·3011	−0·1279
F_{22}	K_{NH} + 0·5918	K_{NH} + 0·5938	K_{NH} + 0·5918	K_{NH} + 0·5906	K_{NH} + 0·5874	K_{NC} + 0·1981
	(6·7567)	(6·7587)	(6·7567)	(6·7555)	(6·7523)	(5·1680)
F_{23}	0·9929	1·0037	1·0117	1·0144	1·0184	0·2933
F_{24}	0·2972	0·2949	0·2910	0·2891	0·2854	0·1278
F_{33}	K_{BN} + 1·2476	K_{BN} + 1·3159	K_{BN} + 1·2978	K_{BN} + 1·3053	K_{BN} + 1·3227	K_{BN} + 0·9627
	(5·8955)	(5·9638)	(5·9457)	(5·9532)	(5·9706)	(5·6116)
F_{34}	0·1455	0·0901	0·0856	0·0754	0·0534	−0·0181
F_{44}	$\frac{1}{2}(H_B + H_N)$	$\frac{1}{2}(H_B + H_N)$	$\frac{1}{2}(H_B + H_N)$	$\frac{1}{2}(H_B + H_N)$	$\frac{1}{2}(H_B + H_N)$	$\frac{1}{2}(H_B + H_N)$
	+0·1390	+0·1486	+0·1424	+0·1403	+0·1344	+0·1091
	(0·5846)	(0·5942)	(0·588)	(0·586)	(0·58)	(0·5547)
			e' Species			
F_{55}	K_{BH} + 0·2426	K_{BF} + 0·3668	K_{BCl} + 0·4	K_{BBr} + 0·4276	K_{BI} + 0·4886	K_{BH} + 0·2396
	(3·5552)	(7·3668)	(4·0)	(3·4276)	(2·3886)	(3·5522)
F_{56}	0·0026	0·0053	0·0087	0·0099	0·0120	0·0020
F_{57}	−0·1935	−0·2930	−0·2862	−0·3014	−0·3356	−0·1907
F_{58}	0·3352	0·5075	0·4957	0·5220	0·5813	0·3303
F_{59}	0·0	0·0	0·0	0·0	0·0	0·0
$F_{5,10}$	−0·0085	−0·0191	−0·0440	−0·0557	−0·0842	−0·0070
$F_{5,11}$	−0·1325	−0·2175	−0·2552	−0·2800	−0·3355	−0·1308
F_{66}	K_{NH} +0·5918	K_{NH} + 0·5938	K_{NH} + 0·5918	K_{NH} + 0·5906	K_{NH} + 0·5874	K_{NC} + 0·1981
	(6·7567)	(6·7587)	(6·7567)	(6·7575)	(6·7523)	(5·1681)
F_{67}	0·2482	0·2509	0·2529	0·2536	0·2546	0·0733
F_{68}	0·4299	0·4346	0·4380	0·4392	0·4410	0·1270
F_{69}	−0·0104	−0·0211	−0·0334	−0·0376	−0·0436	0·0124
$F_{6,10}$	0·0	0·0	0·0	0 0	0·0	0·0
$F_{6,11}$	0·1502	0·1505	0·1503	0·1500	0·1490	0 0586
F_{77}	K_{BN} + 0·5056	K_{BN} + 0·5740	K_{BN} + 0·5559	K_{BN} + 0·5634	K_{BN} + 0·5808	K_{BN} + 0·2207
	(4·6)	(4·7)	(4·8)	(4·8)	(4·8)	(4·42)
F_{78}	0·0	0·0	0·0	0·0	0·0	0·0
F_{79}	0·0	0·0	0·0	0·0	0·0	0·0
$F_{7,10}$	−0·3108	−0·3231	−0·3453	−0·3549	−0·3778	−0·1092
$F_{7,11}$	−0·0320	0·0057	0·0261	0·0391	0 0687	−0·1149
F_{88}	K_{BN} + 1·002	K_{BN} + 1·0686	K_{BN} + 1·0505	K_{BN} + 1·058	K_{BN} + 1·0754	K_{BN} + 0·7153
	(5·648)	(5·7165)	(5·6984)	(5·706)	(5·7233)	(5·363)
F_{89}	0·0	0·0	0·0	0·0	0·0	0·0
$F_{8,10}$	−0·3108	−0·3231	−0·3452	−0·3549	−0·3778	−0·1092
$F_{8,11}$	0·1261	0·0781	0·0741	0·0653	0·0462	0·158

Contd.

Table 2—Symmetry Potential Energy Constants (mdyne Å) for Borazines (Contd.)

	$(HBNH)_3$	$(FBNH)_3$	$(ClBNH)_3$	$(BrBNH)_3$	$(IBNH)_3$	$[(HBN(CH_3)]_3$
F_{99}	$L_B + 0.2008$ (0.83)	$L_B + 0.3502$ (0.65)	$L_B + 0.4882$ (0.66)	$L_B + 0.5608$ (0.6)	$L_B + 0.7336$ (0.75)	$L_B + 0.1996$ (0.85)
$F_{9,10}$	−0.0092	−0.0209	−0.0493	−0.0625	−0.0953	−0.0108
$F_{9,11}$	0.0	0.0	0.0	0.0	0.0	0.0
$F_{10,10}$	$L_N + 0.4168$ (0.95)	$L_N + 0.4368$ (0.8)	$L_N + 0.4766$ (0.84)	$L_N + 0.4942$ (0.85)	$L_N + 0.5368$ (0.85)	$L_{NC} + 0.1905$
$F_{10,11}$	0.2509	0.2800	0.3220	0.3409	0.3871	0.1233
$F_{11,11}$	$\frac{1}{2}(H_B + H_N + 0.3368)$ (0.614)	$\frac{1}{2}(H_B + H_N + 0.3676)$ (0.6294)	$\frac{1}{2}(H_B + H_N + 0.3835)$ (0.6471)	$\frac{1}{2}(H_B + H_N + 0.3927)$ (0.642)	$\frac{1}{2}(H_B + H_N + 0.4138)$ (0.65)	$\frac{1}{2}(H_B + H_N 0.27)$ (0.585)

The values given in the parentheses denote the actual numerical values of the corresponding diagonal elements.

Table 3—Calculated and Observed Frequencies for Borazine and Substituted Borazines $(BXNY)_3$ in cm^{-1}

		$(HBNH)_3$		$(DBNH)_3$		$(HBND)_3$		$(DBND)_3$	
		Calc	Obs	Calc	Obs	Calc	Obs	Calc	Obs
				a_1' Species					
N-Y st.s.	ν_1	3453·4	3452	3453·4	3452	2536·4	2579	2505·6	2567
B-X st.s.	ν_2	2536	2535	1873·4	1893	2505·3	2521	1873·4	1895
B-N ring st.s.	ν_3	940·4	940	915·2	903	934·8	940	905·3	901
B-N ring bend s.	ν_4	852·3	852	838·7	852	835·9	824	826·6	824
				e' Species					
N-Y st.as.	ν_5	3481	3486	3481	3485	2544	2594	2540	2582
B-N ring st.as.	ν_6	2538	2520	1878	1897	2534	251	1874	1895
B-N ring st.as.	ν_7	1535	1465	1461	1440	1534	1438	1454	1418
N-Y bend as.	ν_8	1474	1406	1448	1328	1295	1289	1253	1245
B-X st.as.	ν_9	1121	1096	1031	1022	1029	1071	911	797
B-N ring bend as.	ν_{10}	904	990	736	813	847	786	731	766
B-X bend as.	ν_{11}	516	518	508	509	501	—	493	—

	$(FBNH)_3$		$(FBND)_3$		$(ClBNH)_3$		$(ClBND)_3$	
	Calc	Obs	Calc	Obs	Calc	Obs	Calc	Obs
			a_1' Species					
ν_1	3453	3440	2505	2566*	3453	3412	2505	2539
ν_2	1479	1474*	1479	1460*	1155	1350	1154	–
ν_3	872	863	850	821*	865	866	844	828
ν_4	530	551	530	539*	365	358	365	357
			e' Species					
ν_5	3482	3478	2540	2578	3481	3446	2542	2569
ν_6	1581	1506	1543	1474	1505	1443	1474	1414
ν_7	1403	1396	1385	1391	1413	1334	1307	1255
ν_8	1171	1137	990	1025	1041	1032	873	816
ν_9	909	921	844	718	761	743	755	739
ν_{10}	415	435	400	425	366	376	352	367
ν_{11}	245	289	245	314	183	172	183	170

Contd

Table 3 – Calculated and Observed Frequencies for Borazine and Substituted Borazines $(BXNY)_3$ in cm^{-1} (Contd.)

	$(BrBNH)_3$		$(BrBND)_3$		$(IBNH)_3$		$(IBND)_3$	
	Calc	Obs	Calc	Obs	Calc	Obs	Calc	Obs
			a_1' Species					
ν_1	3453	3420	2505	2530	3452	—	2504	—
ν_2	1088	—	1088	—	985	—	985	—
ν_3	862	859	841	829	855	—	834	—
ν_4	237	228	237	225	169	—	169	—
			e' Species					
ν_5	3481	3466	2540	2532	3480	—	2541	—
ν_6	1505	1436	1470	1404	1528	—	1503	—
ν_7	1408	1327	1287	1241	1415	—	1275	—
ν_8	1027	1025	876	806	1022	—	888	—
ν_9	673	665	662	664	559	—	544	—
ν_{10}	318	316	306	309	292	—	280	—
ν_{11}	122	114	122	111	103	—	103	—

	$(HBN\text{-}CH_3)_3$		$(DBN\text{-}CH_3)_3^{\dagger}$	$(HBN\text{-}CD_3)_3^{\dagger}$	$(DBN\text{-}CD_3)_3^{\dagger}$
	Calc	Obs	Calc	Calc	Calc
			a_1 Species		
ν_1	2536		1875	2536	1875
ν_2	1353	inactive in I.R.	1352	1391	1391
ν_3	938		897	938	898
ν_4	623		623	646	646
			e' Species		
ν_5	2537	2505-2560	2537	1875	1873
ν_6	1533	1485-1492	1532	1483	1461
ν_7	1470	1323-1427	1325	1420	1290
ν_8	1275	1265**	1272	1250	1244
ν_9	1106	1067	1000	1033	908
ν_{10}	893	894	846	729	725
ν_{11}	489	not recorded	495	481	487

* From Ref. 4

† Recorded in ref. 2, but not fully assigned

†* A band at this position was recorded in all B-halogenated N-trimethyl molecules but not assigned in Ref. 3

systematic trend in the variation of halogenated BX_2Y type molecules where they occur at 1247, 701, 637 cm^{-1} respectively[5] in which the data on iodinated molecules are not included as they are not available.

5. The bands at 245, 183, 122 and 103 cm^{-1} in e' species should be assigned to the B–X bending frequencies respectively as they also show a regular trend.

6. It is also worth noting the variations of the ring bending frequency in the e' species in all the cases. They occur at 516 cm^{-1} in borazine and fall to 415, 366, 318 and 292 cm^{-1} in B-halogenated borazines in F, Cl, Br, I order.

7. The results of the N-trimethyl borazine compounds have been obtained with the reduced mass of the methyl group.[6] The N—CH_3 stretch and the N—CH_3 in-plane bend, ν_8 and ν_9, respectively (see Table 3) have not properly been identified in the earlier experimental work,[2,3] but they are possible through the normal coordinate analysis carried out here. While most of the force constants have been fixed from the values for the rest of the molecules, the N—CH_3 stretch value has been initially taken[7] from CH_3NH_2 and the N—CH_3 bend value was varied.

References

1. Subhedar M K & Thyagarajan G, *Indian J. pure appl. Phys.*, 12 (1974), 498.
2. Totani T & Watanabe H, *Spectrochim. Acta*, **25A** (1969), 585.
3. Anderson G A & Lagowski J J, *Spectrochim. Acta*, **26A** (1970), 2013.
4. Blick K E, Dawson J W & Niedenzer K, *Inorg. Chem.*, **9** (1970), 1416.
5. Ford T A & Orville-Thomas W J, *Spectrochim. Acta*, **23A** (1967), 579.
6. King W T & Crawford Bryce (Jr), *J. Molec. Spectrosc.*, 5 (1960), 421.
7. Dellepiane G & Zerbi G, *J. chem. Phys.*, **48** (1968), 3573.

Indian Journal of Pure & Applied Physics
Vol. 18, June 1980, pp. 401-403

Dielectric Properties of Indian Clay Minerals : Bentonite & Pyrophillite

M K Mahan, B L Jha & A R Chetal

Department of Physics & Mathematics, Indian School of Mines, Dhanbad 826 004

Received 3 *April* 1979; *revised received* 29 *November* 1979

The dielectric properties of the Indian clay minerals bentonite and pyrophillite, have been studied in the radio frequency range. It has been observed that the dielectric constant (ϵ') increases as the adsorbed water content increases. The increase in ϵ' is more for bentonite than that for pyrophillite. Also, ϵ' has been found to be directly proportional to the adsorbed water content, base exchange capacity, degree of lattice expansion and density of the mineral. Loss tangent studies show that the conduction is by displacement current.

1. Introduction

There are various factors, viz. structure, composition, moisture content, porosity, temperature, pressure, salinity, etc. which affect the dielectric properties of materials. To understand the dielectric behaviour of clay minerals it is necessary to study the effects of these factors in detail. In the present study, the effect of moisture content (adsorbed water content) on dielectric properties of the Indian clay minerals, bentonite (Kashmir) and pyrophillite (Uttar Pradesh), at radio frequency has been taken up. To our knowledge, no such work seems to have been done on these clays.

2. Experimental Procedure

The clay minerals investigated were obtained from the Department of Chemistry, Allahabad University, Allahabad. The samples were crushed and powdered and passed through 200 mesh sieve to get rid of non-clay minerals. Remaining non-clayey portions were removed by heavy liquid separation. The separated clayey fractions were thoroughly washed with distilled water followed by absolute alcohol. Finally, the chemical analysis of the clayey fraction was carried out and the base exchange capacities (BEC) were determined.

An important aspect of the measurement of dielectric properties is the means of holding the sample during the measurement. One of the main requirements placed upon a sample holder is that the geometry of the electrodes be such that the distribution of the field is known. The measurements were carried out using a sample holder fabricated in our laboratory. The electrodes of the sample holder were of 50 mm diam. and were precision ground. The samples used were in the form of pellets (diam., 50 mm). As no binder was used for making the pellets, the formation of pellets was tried at different pressures. We found that the pellets were formed easily at the pressure of 640 kg/cm^2. Thickness of the pellets varied from 2 to 3 mm. To get rid of series air capacitance due to the remaining micropore contact between the pellet surface and the holder electrodes, the pellet surface was coated with the air drying silver conducting paint[1,2] obtained from the National Physical Laboratory, New Delhi. Shielded wires were used as leads of the electrodes to avoid stray capacitance between the leads. To get dry samples, the painted pellets were placed in an oven at 100°C till constant weight was achieved. The sample was then removed from the oven and placed immediately in the sample holder. The sample holder with the pellet was then placed in the glass chamber in which vacuum of the order of 10^{-3} mm of mercury was maintained throughout the course of the measurement. To obtain moist samples, the dry samples were exposed to atmosphere for different lengths of time with the silver paint electrode on. Errors introduced due to the moisture loss during the course of measurements were avoided by taking the average of the moisture percentage determined by weighing the sample prior to and after the measurements. The loss in moisture content during the experiment was never more than 0.01%.

Dielectric constant (ϵ') and loss tangent ($\tan \delta$) were measured using an Advance Q meter Type T2 No. 422, England. The measurements were carried out by using the two-electrodes system.[1] The reproducibility of the measurement was checked after each run by repeating the measurements. A maximum variation between the two readings for ϵ' and

tan δ was about 5 and 7% respectively. The estimated accuracies obtained for the different parameters are: frequency, $\pm$ 1%; capacitance, 0·2 pF; and tan δ, $\pm$ 5%.

3. Results and Discussion

The chemical analysis data for the samples are presented in Table 1. The general behaviour of ϵ' as a function of frequency is shown in Fig. 1 for both the dry and the moist samples. It is clear from Fig. 1 that whereas ϵ' is almost independent of frequency in the case of dry samples, a dispersion is observed up to frequency of 5·0 and 6·0 MHz in the case of moist samples of bentonite and pyrophillite respectively. This suggests that at higher frequencies the measured ϵ' may represent the intrinsic ϵ'. The increase in ϵ' due to moisture at lower frequencies may be attributed to the interfacial effects.[3] We feel that some sort of interfacial polarization is formed, most probably at the boundaries of the clays at these frequencies. It is probable that the phenomenon observed here is closely related to the induced polarization which according to Howell and Licastro[2] is prominent in clays. The low frequency dispersion in the moist samples may also be attributed to the limitations of the motion of impurity charges within the crystals of the samples and to the presence of moisture. These lead to the Maxwell-Wagner type of polarization.

In the case of dry samples, ϵ' is nearly independent of frequency, suggesting that the adsorbed water plays an important role in increasing ϵ'. It may be due to high permittivity of water.[4] It is also seen from Fig. 1 that ϵ' of the dry sample of bentonite is greater than that of pyrophillite. We attribute this to the BEC which is greater for bentonite (111·49 m eq/100 g) than for pyrophillite (22·41 m eq/100 g). The other possible explanation for bentonite having high ϵ' is that although both bentonite and pyrophillite are three-layer clays, the lattice of the former is expanding and that of the latter is non-expanding.[5] We also observe that the dispersion is stronger in bentonite than in pyrophillite. This may be due to the following reasons : (i) Dispersion is directly proportional to the degree of lattice expansion of the samples; and (ii) Counter ions are present in the expandable clays

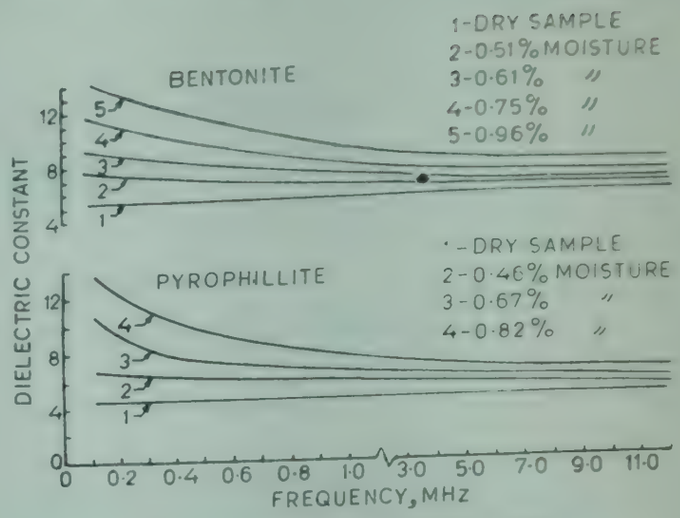

Fig. 1—Variation of ϵ' with frequency

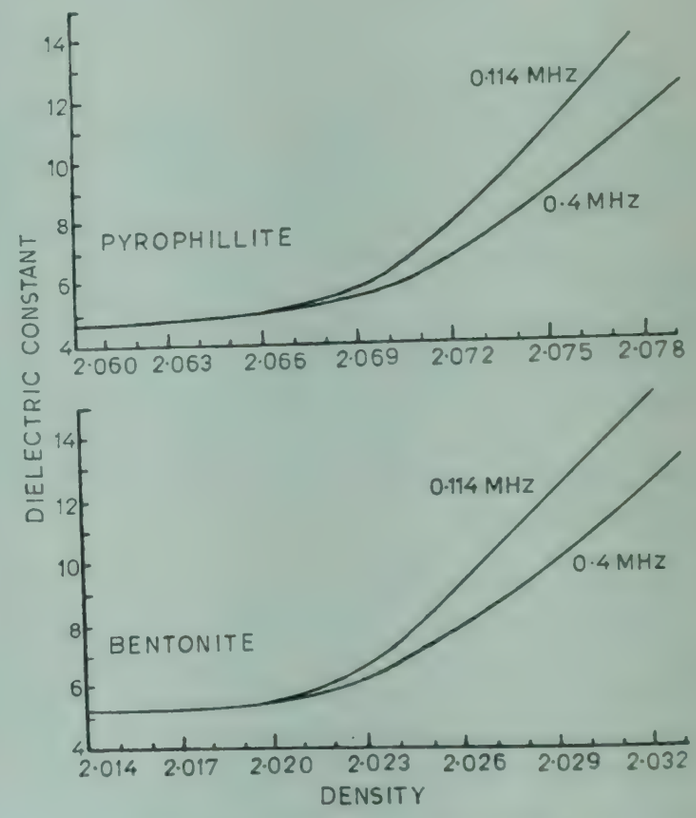

Fig. 2—Variation of ϵ' with density

Table 1—Chemical Analysis of Indian Clay Minerals

Constituent	Clay minerals	
	Bentonite (Kashmir) %	Pyrophillite (Uttar Pradesh) %
SiO_2	54·64	60·28
TiO_2	Trace	—
Al_2O_3	20·52	30·29
Fe_2O_3	2·15	3·92
MgO	5·48	1·21
CaO	2·25	1·38
Na_2O	1·20	—
K_2O	0·65	0·42
H_2O^+	11·20	2·04
H_2O^-	2·04	0·80

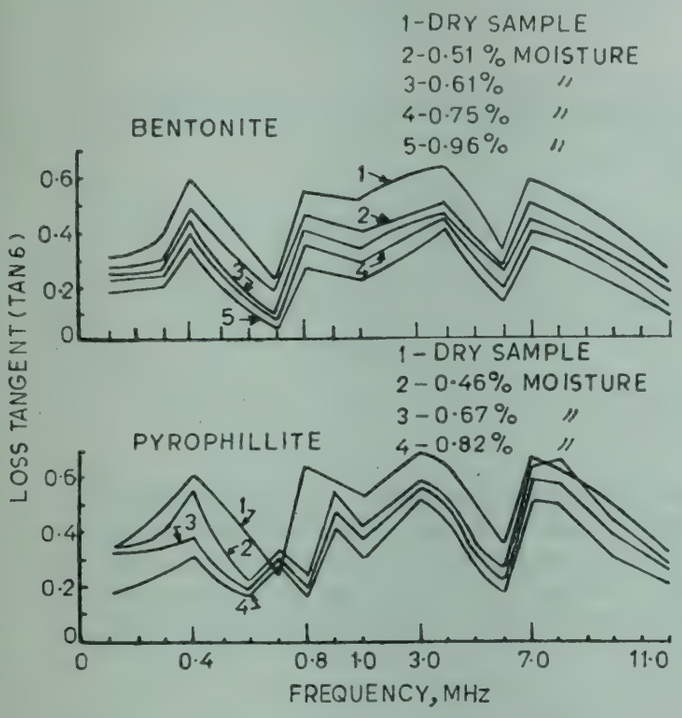

Fig. 3—Variation of tan δ with frequency

and the particle association is strongest in such clay minerals compared with the non-expandable clay minerals.

Fig. 2 shows that ϵ' increases with density. These results are difficult to explain and require further investigation. However, we might mention that our results also show trends similar to those observed by other workers.[6-12]

The dependence of tan δ on frequency for both the dry and the moist samples is shown in Fig. 3. The tan δ values are less than unity in all the samples studied. This suggests that the conduction is by the displacement current.[13] The experimental values for tanδ provide information about the nature of polarization. It can be seen from Fig. 3 that whereas the number of peaks are same both in the dry as well as in the moist samples of bentonite, one extra peak is observed around 0·7 MHz in the case of moist samples of pyrophillite, which is difficult to explain as the electrical polarization that takes place in the rocks or clays is very complicated. There is a host of phenomena occurring in such systems which contribute to the electrical polarization.[13]

Acknowledgement

The authors are thankful to Dr A Mansingh, University of Delhi, Delhi, for fruitful suggestions and to Dr B Sengupta for supplying and purifying the samples. One of us (MKM) is grateful to the University Grants Commission, New Delhi, for the financial assistance.

References

1. ASTM (American Society for Testing Materials, Philadelphia) D-150-65 T (1966), 68.
2. Howell B F & Licastro P F, *Am. Miner.*, 46 (1961), 269.
3. Olhoeft G R & Strangway D W, *Earth Planet. Sci. Lett.*, 24 (1975), 394.
4. Chatterjee S K, *Indian J. Phys.*, 22 (1948), 260.
5. Grim R E, *Clay mineralogy* (McGraw-Hill Book Co. Inc., London), 1953.
6. Alvarez R, *Trans. Am. geophys. Un.*, 51 (1973), 1129.
7. Bassett H L & Shackleford R G, *Geochim. Cosmochim. Acta, Suppl.*, 3 (1972), 3175.
8. Frisillio A L, Olhoeft G R & Strangway D W, *Earth Planet. Sci. Lett.*, 24 (1975), 345.
9. Gold T, Campbell M J & O'Leary B T, *Proc. Apollo* 11 *Lunar Sci. Conf.*, 3 (1970), 2149.
10. Gold T, O'Leary B T & Campbell M, *Proc. 2nd Lunar Sci. Conf.*, 3 (1971), 2173.
11. Gold T, Bilson E & Yerbury M, *Proc. 3rd Lunar Sci. Conf.*, 3 (1972), 3187.
12. Gold T, Bilson E & Yerbury M, *Lunar Sci.*, 4 (1973), 293.
13. Parkhomenko E I, *Electrical properties of rocks* (Plenum Press, New York), 1967.

Indian Journal of Pure & Applied Physics
Vol. 18, June 1980, pp. 404-407

Dielectric Relaxation in Methylmercaptoacetate & Methylcyanoacetate in Benzene Solution

K SENGUPTA

Optics Department, Indian Association for the Cultivation of Science, Jadavpur, Calcutta 700 032

Received 26 *December* 1978

Complex dielectric permittivities for methylmercaptoacetate and methylcyanoacetate in benzene solution have been determined at four microwave frequencies (8·6, 18·3, 24·4 and 35·14 GHz) and at three temperatures (30, 45 and 60°C). The dielectric data have been analyzed into two relaxation mechanisms, viz. molecular orientation and internal rotation. The energy barriers for molecular and group rotations have been determined. Comparison of the observed dipole moment with the moments calculated for *cis*- and *gauche*-conformers shows that the *cis*-conformer is the major constituent in both the esters.

1. Introduction

Various investigations, namely, dipole moment,[1-3] infrared[4] and microwave spectroscopy,[5,6] have established that the *trans*-conformer is much more abundant than the *cis*-conformer in simple aliphatic esters (see chart 1). This result has been attributed to the rigid coupling of R_2 with the carbonyl oxygen, either in O—C—O plane[5,6] or a few degrees outside this plane[7,8] in esters with large R_2. Accordingly, the internal rotation of OR_2 about the C—O bond is inhibited. In substituted aliphatic esters, the situation is different; the internal rotation about the C—C bond is possible and has been reported in halogenated esters.[9,10] The object of the present investigation is to study the possibility of internal rotation and identify the molecular conformations in the esters of methylcyanoacetate and methylmercaptoacetate (hereafter abbreviated as MCA and MMA respectively). The results of investigations of microwave absorption at different frequency regions in the two esters are presented and discussed in this paper.

2. Experimental Details

Samples of MMA and MCA of 99% purity, procured from Ega Chemie, (Germany), and the solvent, AR grade benzene, were dried and distilled under reduced pressure before use.

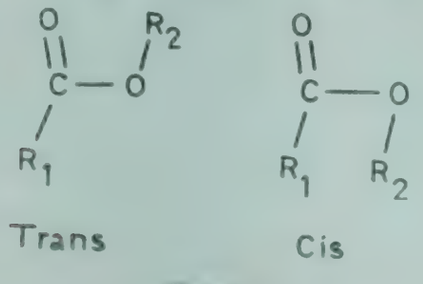

Chart 1

The experimental arrangements and techniques for the measurement of dielectric permittivity (ϵ'), dielectric loss (ϵ'') at microwave frequencies, viscosity (η), refractive index (n_D) and static dielectric constant (ϵ_0) are the same as described earlier.[11] During the experiments the temperature was maintained constant within $\pm$ 1°C by means of a thermostat. Estimated error in the measurements of ϵ' and ϵ'' was about 2 and 4% respectively.

3. Results and Discussion

The experimental values of ϵ' and ϵ'' at different frequencies and temperatures are given in Table 1. The values of ϵ_0, density (d), η and n_D at different temperatures are given in Table 2. Cole-Cole arc plots drawn between ϵ' and ϵ'' (Fig. 1) show significant distribution parameter (α), which indicates the presence of more than one relaxation process in both the esters. Further, the plots of ϵ' versus $\epsilon''\omega$ (Fig. 2), where ω is the angular frequency, are not linear, but two straight lines pass through the points. This confirms that two relaxation mechanisms occur in the two esters. The dielectric data have, therefore, been analyzed for the two relaxation times (τ_1 and τ_2) using the relationships[12]

$$\frac{\epsilon' - \epsilon_\infty}{\epsilon_0 - \epsilon_\infty} = \frac{C_1}{1+(\omega\tau_1)^2} + \frac{C_2}{1+(\omega\tau_2)^2} \quad \ldots(1)$$

$$\frac{\epsilon''}{\epsilon_0 - \epsilon_\infty} = \frac{C_1\omega\tau_1}{1+(\omega\tau_1)^2} + \frac{C_2\omega\tau_2}{1+(\omega\tau_2)^2} \quad \ldots(2)$$

Table 1—Experimental Values of ϵ' and ϵ'' of the Two Esters in Benzene at Different Temperatures and Frequencies

Temp °C	Frequency GHz	0·09 *M* MCA				0·33 *M* MMA			
		ϵ'obs	ϵ'calc	ϵ''obs	ϵ''calc	ϵ'obs	ϵ'calc	ϵ''obs	ϵ''calc
30	8·6	3·36	3·36	0·64	0·66	4·07	4·02	0·58	0·64
45	8·6	3·38	3·37	0·55	0·56	4·04	4·00	0·48	0·54
60	8·6	3·40	3·38	0·44	0·47	3·94	3·90	0·33	0·40
30	18·3	3·00	3·01	0·57	0·56	3·68	3·67	0·70	0·68
45	18·3	3·06	3·07	0·52	0·52	3·70	3·70	0·62	0·60
60	18·3	3·12	3·13	0·47	0·46	3·72	3·69	0·47	0·46
30	24·4	2·88	2.89	0·50	0·50	3·50	3·53	0·71	0·70
45	24·4	2·95	2 96	0·48	0·48	3·59	3·59	0·64	0·63
60	24·4	3·02	3·04	0·45	0·45	3·60	3·62	0·51	0·49
30	35·14	2·78	2·76	0·42	0·40	3·28	3·31	0·68	0·71
45	35·14	2·82	2·82	0·41	0·41	3·35	3·40	0 64	0·67
60	35·14	2·90	2·90	0·41	0·41	3·42	3·49	0·54	0·57

Table 2—Values of α, ϵ_0, d, η, n_D^2, ϵ_∞ and μ of the Two Esters in Benzene at Different Temperatures

Temp °C	α	ϵ_0	d, g/cc 0·09*M*	η cp MMA	n_D^2	ϵ_∞	μ D
30	0·21	4·62	0·956	0·50	2·20	2·60	2·18
45	0·24	4·46	0·942	0·44	2·16	2·56	2·17
60	0·28	4·21	0·926	0·38	2·11	2·49	2·15
			0·33*M*	MCA			
30	0·13	4·30	0·895	0·52	2·18	2·60	3·87
45	0·16	4·12	0·878	0·44	2·15	2·60	3·83
60	0·19	3·93	0·862	0·37	2·11	2·60	3·81

which after simplification are solved by the method of least squares.[13,14] The values of τ_1, τ_2 and C_2 thus obtained are given in Table 3. The values of ϵ' and ϵ'' calculated using these values of τ_1, τ_2 and C_1 are included in Table 1 for comparison with the experimentally obtained values.

The heats of activation for molecular orientation ($\Delta H\tau_1$) and the energy barrier for internal rotation ($\Delta H\tau_2$) are obtained from the slopes of the plots of $\log \tau_1 T$ versus $1/T$ and $\log \tau_2 T$ versus $1/T$ respectively. The heat of activation for viscous flow ($\Delta H\eta$) is obtained from similar plots of $\log \eta$ versus $1/T$. The dipole moment (μ) is calculated from the relation:[15]

$$\mu^2 = \frac{9kT}{4\pi N} \cdot \frac{(\epsilon_0 - \epsilon_\infty)(2\epsilon_0 + \epsilon_\infty)}{\epsilon_0 (\epsilon_0 + \epsilon_\infty)^2} \quad \ldots(3)$$

where N is the number of solute molecules/ml of the solution, and k the Boltzmann's constant. The values of α, ϵ_∞ and μ are included in Table 2 and those of $\Delta H\tau_1$, $\Delta H\tau_2$ and $\Delta H\eta$ in Table 3.

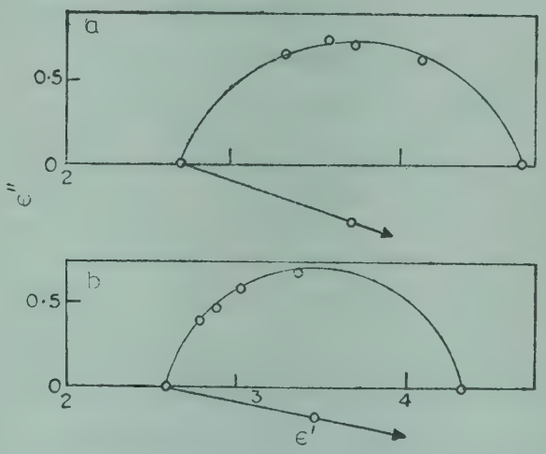

Fig. 1—Cole-Cole arc plots for esters (a) MCA and (b) MMA

3.1 Relaxation Time

It is seen from Table 3 that the molecular relaxation time τ_1 for MCA at 30°C (38 psec) is larger than that for MMA (24 psec). This shows that the MCA molecule is much larger than the MMA molecule.

If the shorter relaxation times (τ_2) are due to internal rotation of the $-OCH_3$ group about the C—O bond, they should be of equal magnitude in both the esters. But the value of τ_2 for MCA at 30°C (8·4 psec) is much larger than that for MMA (3·5 psec). This suggests that the internal rotation in the two esters does not arise due to the $-OCH_3$ group rotation about the C—O bond, and this supports the view reported earlier.[1-6] The value of τ_2 (8·4 psec) in MCA at 30°C, which compares well with the value of the $-CH_2CN$ group relaxation time of 8·9 psec in *p*-xylylenecyanide,[16] is attributed to the $-CH_2CN$ group relaxation time about the C—C bond in MCA. Similarly the value of τ_2 ($\simeq$3·5 psec) in MMA at 30°C compares well with the value of

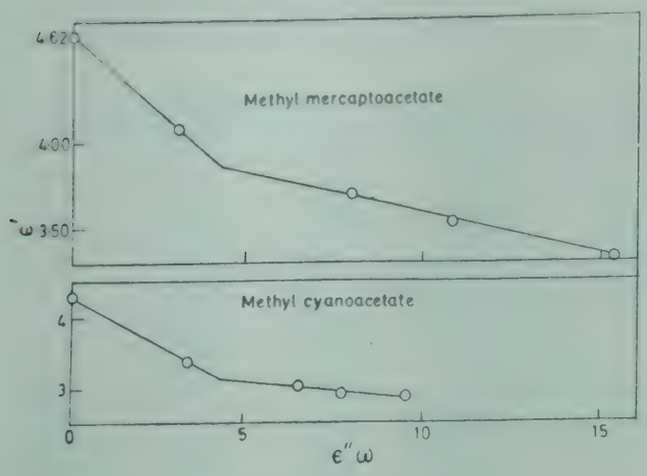

Fig. 2 –Plots of ϵ' versus $\epsilon''\omega$

Table 3—Values of τ_1, τ_2, C_2, $\Delta H\tau_1$, $\Delta H\tau_2$ and $\Delta H\eta$ of the Two Esters in Benzene

Temp °C	τ_1 psec	τ_2 psec	C_2	$\Delta H\tau_1$ kcal/mole	$\Delta H\tau_2$ kcal/mole	$\Delta H\eta$ kcal/mole
			MMA			
30	24·0	3·6	0·56			
45	22·2	2·9	0·61	0·50	3·1	1·8
60	21·0	2·1	0·69			
			MCA			
30	38·0	8·4	0·41			
45	35·6	6·6	0·44	1·14	3·0	2·14
60	29·5	4·9	0·47			

the $-CH_2SH$ group relaxation time of 3·5 psec in benzylthiol[17] in the liquid state at 30°C and, is therefore, assigned to the group rotation of $-CH_2SH$ group about C—C bond in MMA.

3.2 Heats of Activation

The values of $\Delta H\tau_1$ (0·5-1·14 kcal/mole) are found to be much less than those of $\Delta H\eta$ (3·1-3·0 kcal/mole) in both the esters. The value of $\Delta H\tau_2$ is about 3 kcal/mole in each ester and is much larger than that of $\Delta H\tau_1$. This shows that the groups are much less flexible to rotate than the molecules.

It is seen from Table 3 that the weight factor for group rotation C_2 is about 0·6 in MMA and 0·45 in MCA.

3.3 Dipole Moment and Molecular Configurations

The observed value of μ of MCA at 30°C is 3·87D which decreases slightly with increase of temperature (Table 2). This indicates the presence of more than one conformer in this liquid and the conformer with lower moment increases in proportion at higher temperatures. From infrared studies, Charles *et al.*[18]

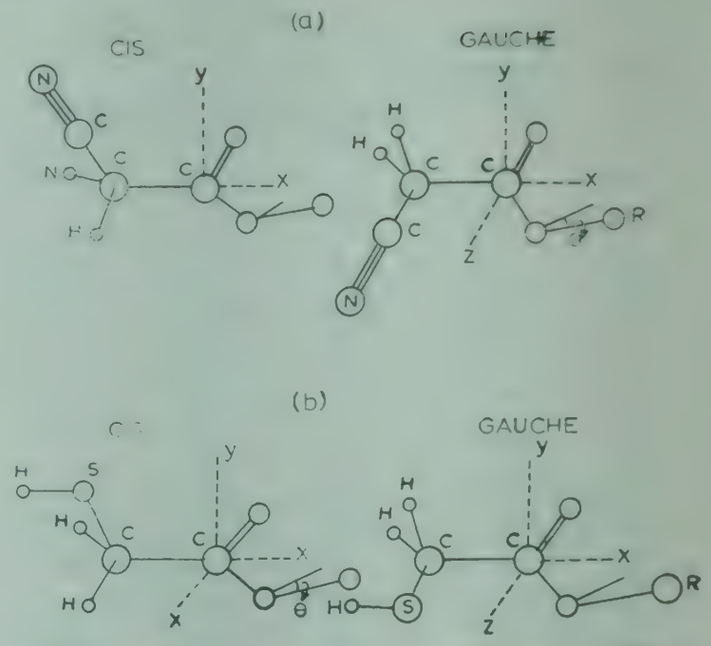

Fig. 3—Molecular conformation of (a) MCA and (b) MMA

reported the existence of *cis*-and *gauche*-conformers (Fig. 3) in the MCA ester. Approximate calculations of the dipole moments from bond moments and bond angles show that μ_1 of the *cis*-conformer is 4·32 D and that μ_2 of the *gauche*-conformer is 2·74 D (Appendix 1). As the apparent moment $\mu = 3{\cdot}87$ D is very close to the moment of the *cis*-conformer (4·3D), it is concluded that the majority of the molecules in this ester are of *cis*-configuration. If n_1 is the fraction of the *cis*-conformer, than,

$$\mu^2 = n_1\,\mu_1^2 + (1-n_1)\,\mu_2^2 \qquad \ldots(4)$$

on solving Eq. (4), the value of n_1 comes out to be 0·68, i.e. 68% of the molecules belong to *cis*-configuration and the rest are *gauche*-conformers.

In the case of MMA, the observed moment is 2·18 D which also decreases with increase in temperature. Kastha and Das[19] reported from infrared and Raman studies the presence of *cis*-and *gauche*-conformers in MMA. The calculated values of the moment for *cis*-and *gauche*-conformers are 2·33 and 1·18D respectively. So in this case also, the observed moment $\mu = 2{\cdot}18$ D is very close to the moment ($\mu = 2{\cdot}0$ D) for the *cis*-conformer. Thus in this ester also the *cis*-conformer is predominant.

Acknowledgement

The author is thankful to Dr S B Roy for helpful discussions and to Prof. G S Kastha for his kind interest in the work.

References

1. Bender M L, *Chem. Rev.*, **60** (1960), 53.
2. Marsden R J B & Sutton L E, *J. chem. Soc.*, Part II, (1936), 1383.
3. Le Fevre R J W & Sundaram A, *J. chem. Soc.*, Part III, (1962), 3904.

4. Welmshurst J K, *J. molec. Spectrosc.*, **1** (1957), 201.
5. Williams G, Owen N L & Sheridon J, *Trans. Faraday Soc.*, **67** (1971), 922.
6. Lister D G & Owen N L, *J. chem. Soc. Faraday II*, **69** (1973), 1036.
7. Oki M & Nakanishi H, *Bull. chem. Soc. Japan*, **43** (1973), 2564.
8. Pinkus A G & Lin E Y, *J. molec. Struct.*, **24** (1975), 19.
9. Srivastava S C & Dinanath, *Indian J. pure appl. Phys.*, **12** (1974), 448.
10. Roy S K, Sengupta K & Roy S B, *Indian J. Phys.*, **51B** (1977), 42.
11. Roy S K, Sengupta K, Ghatak A & Das A, *J. chem. Phys.*, **65** (1976), 3695.
12. Bergmann K, Roberti D & Smyth C P, *J. phys. Chem.*, **64** (1960), 665.
13. Roy S K, Sengupta K & Roy S B, *Bull. chem. Soc. Japan*, **49** (1976), 663,
14. Sengupta K, Roy S K & Roy S B, *Adv. molec. relaxation & interaction Proc.*, **10** (1977), 273.
15. Tay S P & Crossley J, *Can. J. Chem.*, **50** (1972), 2031.
16. Smyth C P, *Molecular relaxation Process*, Special publication No. 20 (Chemical Society, London), 1966, 6.
17. Hasan A, Das A & Ghatak A, *Indian J. Phys.*, **48** (1974), 246.
18. Charles S W, Jones G I L & Owen N L, *J. chem. Soc. Faraday II*, **69** (1973), 1454.
19. Das R & Kastha G S (communicated).
20. Minkin V I, Osipov O A & Zhdanov Y A, *Dipole Moment in Organic Chemistry*, (Plenum Press, New York), 1970.

Appendix I

Approximate calculations of the dipole moments of the *cis*- and *gauche*-conformers of MCA and MMA from bond angles and bond moments.

MCA

Cis-conformer

$$\mu_x = 3{\cdot}1 \cos 70^\circ - 3{\cdot}1 \cos 70^\circ + 2{\cdot}4 \cos 60^\circ + 0{\cdot}74 \cos 64^\circ - 1{\cdot}14 \cos 3^\circ$$

$$\mu_y = 3{\cdot}1 \sin 70^\circ + 2{\cdot}4 \sin 60^\circ - 0{\cdot}74 \sin 64^\circ - 1{\cdot}14 \sin 3^\circ$$

$$\mu = 4{\cdot}32 \text{ D.}$$

Gauche-conformer

$$\mu_x = -3{\cdot}1 \cos 60^\circ \cos 70^\circ - 3{\cdot}1 \sin 60^\circ \cos 70^\bullet + 2{\cdot}4 \cos 60^\circ + 0{\cdot}74 \cos 64^\circ - 1{\cdot}14 \cos 3^\circ.$$

$$\mu_y = -3{\cdot}1 \cos 60^\circ \sin 70^\circ + 2{\cdot}4 \sin 60^\circ - 0{\cdot}74 \sin 64^\circ - 1{\cdot}14 \sin 3^\circ = 3{\cdot}1 \sin 60^\circ \sin 70^\bullet$$

$$\mu = 2{\cdot}74 \text{ D.}$$

MMA

Cis-conformer

$$\mu_x = 0{\cdot}7 - 0{\cdot}9 \cos 70^\circ + 2{\cdot}4 \cos 60^\circ + 0{\cdot}74 \cos 64^\circ - 1{\cdot}14 \cos 3^\circ = 0{\cdot}9 \sin 70^\circ + 2{\cdot}4 \sin 60^\circ - 0{\cdot}74 \sin 64^\circ - 1{\cdot}14 \sin 3^\circ = 2{\cdot}33 \text{ D.}$$

Gauche-conformer

$$\mu_y = -0\,9 \cos 60^\circ \cos 70^\circ - 0{\cdot}9 \sin 60^\circ \cos 70^\circ + 2{\cdot}4 \cos 60^\circ + 0{\cdot}74 \cos 64^\circ - 1{\cdot}14 \cos 3^\circ = -0{\cdot}9 \cos 60^\circ \sin 70^\circ + 2{\cdot}4 \sin 60^\circ - 0{\cdot}74 \sin 64^\circ - 1{\cdot}14 \sin 3^\circ$$

$$\mu = 0{\cdot}9 \sin 60^\circ \sin 70^\circ$$

$$\mu = 1{\cdot}18 \text{ D.}$$

It is assumed that the O—CH_3 in the ester skeleton remains rigidly coupled with the carbonyl oxygen in a plane 31° outside the plane O=C—O (Refs. 7 and 8). The values of the bond moments and bond angles are taken from Minkin *et al*:[20]

$\mu_{C\equiv N} = 3{\cdot}1$ D, $\mu_{C-S} = 0{\cdot}9$ D, $\mu_{H-S} = 0{\cdot}7$ D,

$\mu_{C=O} = 2{\cdot}4$ D, $\mu_{C-O} = 0{\cdot}74$ D, $\mu_{O-CH_3} = 1{\cdot}14$ D.

Indian Journal of Pure & Applied Physics
Vol. 18, June 1980, pp. 408-412

Close-Coupling Approach to Low Energy Electron Scattering by Oxygen Molecule

A K Pande, D N Tripathi & R S Singh
Department of Physics, Banaras Hindu University, Varanasi 221 005

Received 24 *March* 1979

Low energy electron scattering by oxygen molecule in its ground state has been studied using the quantum mechanical close-coupling approach. The method of non-iterative solution of integral equations for the scattering problem is used to calculate the transition T-matrix. Both long-range and short-range forces have been included in the interaction potential. The calculated results for the differential, momentum and total cross-sections for the rotationally elastic and inelastic transitions have been compared with the available theoretical and experimental results. A good agreement between the experimental and theoretical results have been obtained for the total and differential elastic scatterings. There is a discrepancy between the experimental and theoretical values of momentum transfer cross-section.

1. Introduction

The determination of elastic and inelastic scattering cross-sections for electron-oxygen molecule scattering is of great interest due to the presence of the latter in the ionosphere of the planets and in interstellar space and also because of its importance in laser and plasma physics. However, only a few attempts[1-4] have so far been made to study the rotational excitation of oxygen molecule by electron impact.

Oksyuk[1] utilized Fisk's phase shifts[5] to study the problem but could not get good results due to absence of long-range interaction potential in his treatment Takayanagi[2] studied the problem in the Born-approximation considering only the long range part of the interaction potential. Later, Takayanagi and Geltman,[3] improved upon this method by applying spherical distorted wave method of Mjolness and Sampson.[6] They choose a long-range model potential including quadrupole and polarization terms to calculate the total elastic as well as rotational excitation cross-section of e-O_2 system. However, due to the absence of short-range interaction potential the result was not good. Later on, its importance was realized and Geltman and Takayanagi,[4] included the effect of short-range in their paper but again they failed to obtain good results due to the use of distorted wave approximation which is known to be a weak-coupling approximation.

We can say that in all the four earlier studies either the form of interaction potential was not proper or the approach was not correct. Therefore it is worthwhile to study the scattering of electron by oxygen molecule taking into account the effect of long-range as well as short-range interaction potential using a more accurate method, i.e. a close-coupling one. The present study is an attempt in this direction. In the present approach, we have neglected the coupling of spin with the rotational motion according to the findings of Takayanagi and Itikawa.[7]

2. Theory and Method

The rotational excitation cross-section is calculated using the close-coupling formulation of Arthurs and Dalgarno.[8] All quantities are referred to a coordinate system fixed in space at the centre-of-mass of the system. The scattering amplitude for a transition from a rotational state $(j_1 m_1)$ to another state $(j_2 m_2)$ is given by

$$f(j_1 m_1, j_2 m_2; \gamma) = \sqrt{\pi} \sum_{J=0}^{\infty} (2J+1) \sum_{M=-J}^{+J} \sum_{l_1=|J-j_1|}^{|J+j_1|} (2l_1+1)^{1/2} \sum_{l_2=J-j_2}^{|J+l_2|} \sum_{n_2=-l_2}^{+l_2} \begin{pmatrix} j_1 & l_1 & J \\ -m_1 & O & M \end{pmatrix} \begin{pmatrix} l_2 & j_2 & J \\ n_2 & m_2 & -M \end{pmatrix} T^J_{j_1 l_1, j_2 l_2} \; Yl_2 n_2 (\hat{\gamma}) \qquad \ldots(1)$$

where $\begin{pmatrix} a & b & c \\ \alpha & \beta & \gamma \end{pmatrix}$ is a $3j$ coefficient transition and transition matrix. $T^J J(j_1 l_1, j_2 l_2)$ is related to the scattering matrix by

$$T^J_{l_1 l_1, l_2 l_2} = \delta_{j_1 j_2} \delta_{l_1 l_2} - S^J_{j_1 l_1, j_2 l_2}$$

we, therefore, have for the $j_1 \rightarrow j_2$ transition the differential cross-section[8,9]

$$\frac{d\sigma}{d\hat{\gamma}} = \frac{\bar{K}^{-2}_{j_1 j_2}}{2j_1+1} \sum_{m_1=-j_1}^{+j_1} \sum_{m_2=-j_2}^{+j_2} | f(j_1 m_1, j_2 m_2, \hat{\gamma}) |^2 \quad ...(2)$$

$$= \frac{\bar{K}^{-2}_{j_1 j_2}}{4(2j_1+1)} \sum_{\lambda=0}^{\infty} B_\lambda^{j_1 j_2}(E) P_\lambda(\cos\theta) \quad ...(3)$$

The momentum transfer cross-section is given by

$$\sigma^m_{j_1 \rightarrow j_2} = \frac{\pi \bar{K}^{-2}_{j_1 j_2}}{(2j_1+1)} \left(B_0 - \frac{1}{3} B_1 \right) \quad ...(4)$$

The transition elements matrix $T_{j_1 l_1, j_2 l_2}$ are determined from the asymptotic form of the solutions using integral equations algorithm of Sams and Kouri.[10] The partial rotational excitation cross-sections $A^J(j_1 \rightarrow j_2)$ are calculated from

$$A^J = \frac{\pi}{k^2 j_1 j_2 (2j_1+1)} \sum_{l_1=|J-j_2|}^{|J+j_1|} \sum_{l_2=|J-j_2|}^{|J+j_2|} | T^J_{j_1 l_1, j_2 l_2} |^2 \quad ...(5)$$

The rotational excitation cross-section is then determined from the expression

$$\sigma(j_1 \rightarrow j_2) = (2J+1) \sum_{J=0}^{\infty} A_J(j_1 \rightarrow j_2) \quad ..(6)$$

The sum in Eq. (6) is truncated at a certain value of the total angular momentum J_{max} (six in the present work). Further details are given in our previous paper.[11,12]

3. Interaction Potential

The electron-O_2 interaction potential may be written in terms of Legendre polynomials as follows:

$$v(r) = \sum_{\lambda=0}^{\infty} v_\lambda P_\lambda(\cos\theta) \quad ...(7)$$

where for homo-nuclear molecules λ will have only even values and for hetero-nuclear molecules it will have both even and odd values. As it is well known from the study of electron-atom scattering that the polarization force, which arises from a temporary and partial excitation of the atom (molecule) during the encounter, has an important influence on the scattering of slow electrons. In molecules, this interaction becomes orientation dependent. Therefore, our final choice of model potential in the present work is

$$v_\lambda(r) = v^L_\lambda(r) + v^S_\lambda(r) \quad ...(8)$$

The spherical and non-spherical parts of both the components of the potential are given below:
For spherical interaction we have

$$v^P_0(r) = \frac{-\alpha_0}{2r^4} \left[1 - \exp(-r/r_0)^6 \right] \quad ...(9)$$

For the non-spherical interaction, which induces the rotational excitation, one has

$$v^P_2(r) = -\left[\frac{\alpha_2}{2r^4} + \frac{Q}{r^3} \right] P_2(\cos\theta) \left[1 - \exp(-r/r_0)^6 \right] \quad ...(10)$$

In Eqs. (9) and (10), α_0 and α_2 are the spherical and nonspherical polarizabilities respectively of the molecule, Q is its quadrupole moment and r_0 is an adjustable parameter, which is optimized to give good results for total cross-section. The values of the above parameters and the form of the short-range interaction potentials are taken to be the same as in the work of Geltman and Takayanagi.[4]

4. Results and Discussion

The rotational excitation cross-sections for $1 \rightarrow 3$ transition in the ground state of oxygen molecule are shown graphically in Fig. 1.

However, the nature of the present curve is in agreement with the results of Geltman and Takayanagi's[4] distorted wave calculations. The distorted wave method with neglect of nonspherical interaction is known to yield unreasonably large cross-sections[7] and this may in part be responsible for the quantitative discrepancy between the two results.

The close-coupling results of the elastic scattering ($1 \rightarrow 1$ transition) cross-sections are shown in Fig. 2, along with the experimental results of Sunshine *et al.*,[13] and Salop and Nakano.[14] The results are also given along with the results of other workers in Table 1, for some specific incident energy values. The present curve of total elastic cross-sections is in reasonable agreement with the experimental curve. Our results are in good agreement with the results of Salop and Nakano.[14] Keeping in view that the experimental results are accurate within $\pm$ 25%, we can conclude that the results are quite satisfactory.

The angular dependence of the differential cross-sections for the $1 \rightarrow 3$ transition at the incident electron energies of 1·36 eV and 5·0 eV is shown in Fig. 3. It is observed that the curve corresponding to 5·0 eV is more oscillatory as compared with that at 1·16 eV. The results at still lower incident energies which are not shown in Fig. 3, exhibit still less oscillatory nature as a function of angle. Thus, the oscillations which

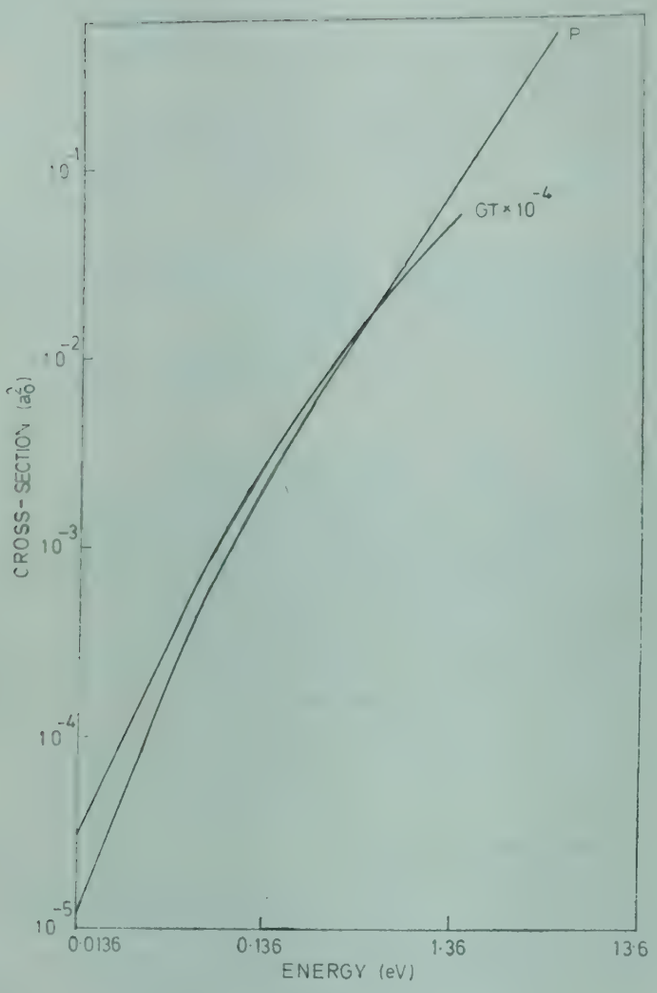

Fig. 1—The close-coupling cross-sections σ (1→3) of oxygen molecule [GT, theoretical results of Geltman and Takayanagi;[4] and P present work]

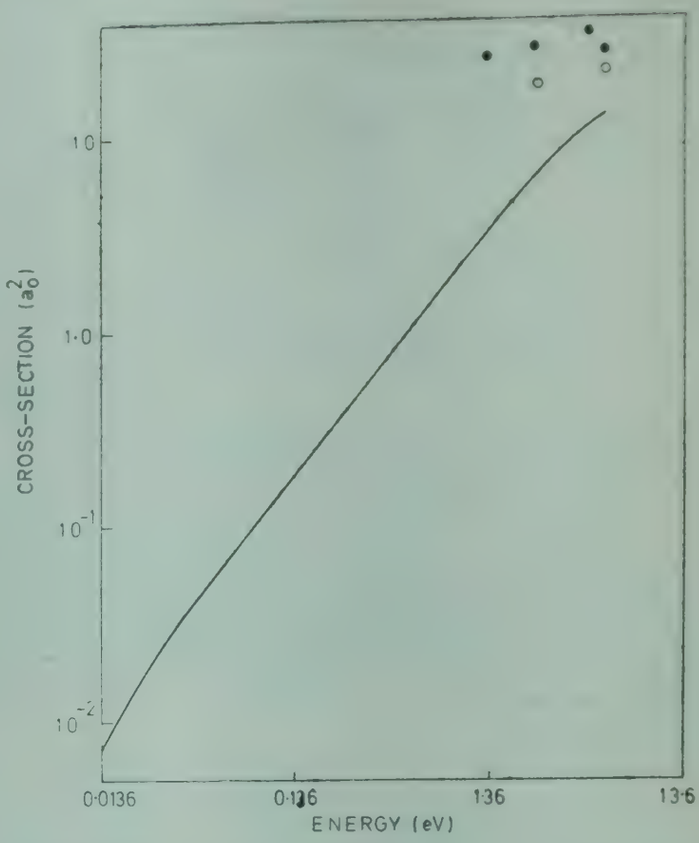

Fig. 2—The experimental and theoretical cross-section (1→1) of oxygen molecule [(———), present work; ●, Sunshine *et al.*[13]; and O Salop and Nakano[14]]

Table 1—Comparison of Total Elastic Cross-sections by Different Workers

Energy eV	Cross-section au
0·0136	$7·5\times10^{-3}$ (Present study)
0·136	$1·7\times10^{-1}$ (Present study)
1·36	2·9 (Present study) 24·2 (Ref. 13)
2·5	6·7 (Present study) 18·6 (Ref. 14) 28·0 (Ref. 13)
5·0	12·5 (Present study) 21 0 (Ref. 14) 26·6 (Ref. 13)
4·5	30·4 (Ref. 15) 11·2 (Present study)

make the differential cross-section curve at 5·0 eV similar to a sine curve, are damped with the decrease of incident energy. As no other results, experimental or theoretical, are available for comparison, it is difficult to ascertain the significance of these results.

The differential cross-sections for elastic scattrering ($j_1=1$ to $j_2=1$) are shown in Fig. 4 at the incident energy of 1·36 eV and 5·0 eV. The present result of the differential cross-section at the incident electron energy of 5·0 eV has been compared with the experimentally determined cross-sections by Hall and Trajmar.[15] The oscillatory nature of the differential cross-section curve becomes quite obvious at high incident energies. These oscillations together with finer details can well be understood with the help of the contributions of different partial waves to the tolal cross-sections.

In order to complete the study of e-O_2 collisions we have also calculated the momentum transfer cross-sections. The momentum transfer cross-sections for the transitions $j_1=1$ to $j_2=3$ and $j_1=1$ to $j_2=1$ have been calculated using the $B_\lambda^{j_1j_2}(E)$ coefficients of close-coupling calculation with the help of expersion (4). The calculated results are shown graphically in Figs. 5 A and B, for the transition 1→3 and 1→1, respectively. The theoretical results of Chang[16] and experimentally determined values of Hake and

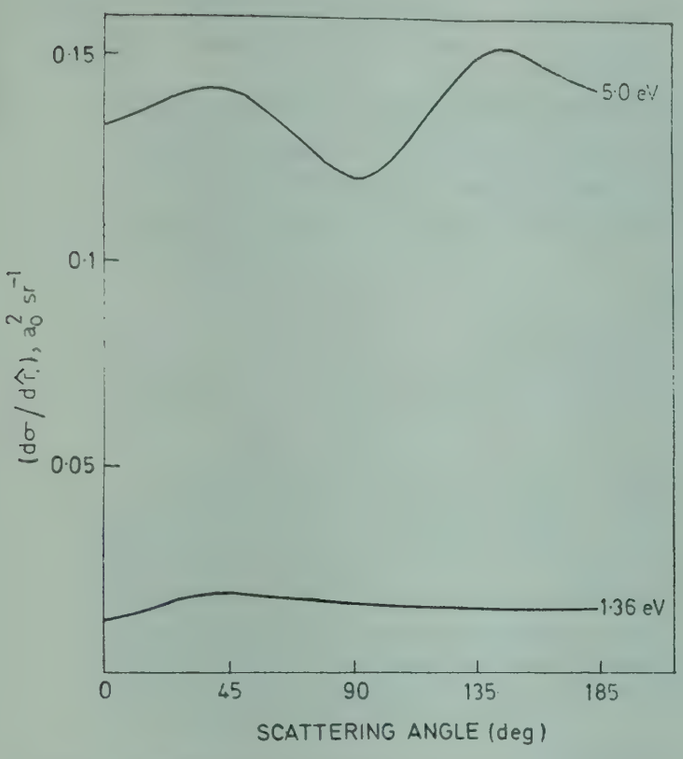

Fig. 3—Differential cross-sections in the 1→3 transition

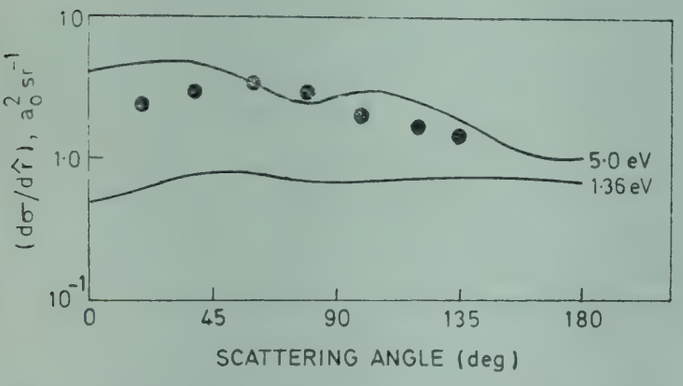

Fig. 4—The experimental and theoretical differential cross-sections of oxygen molecule (●, experimental results of Hall and Trajmar[15])

Phelps[17] are also shown in Fig. 5 (B) for comparison. The momentum transfer cross-section curves for both the transitions are similar to the respective total cross-section curves shown in Figs. 1 and 2, respectively and this, is a good indication for the results being correct. The momentum transfer cross-section for 1→3 transition is lower by a factor of two than that of 1→1 transition. The 1→1 transition curve is almost linear in nature, whereas in the case of 1→3 transition it increases very slowly from 0·0136 eV to 0·136 eV and then rises very steeply assuming a flat shape at about 5·0 eV; thereafter it shows a tendency to fall down. In the absence of any other experimental or theoretical results for 1→1 transition, it is difficult to comment on this feature.

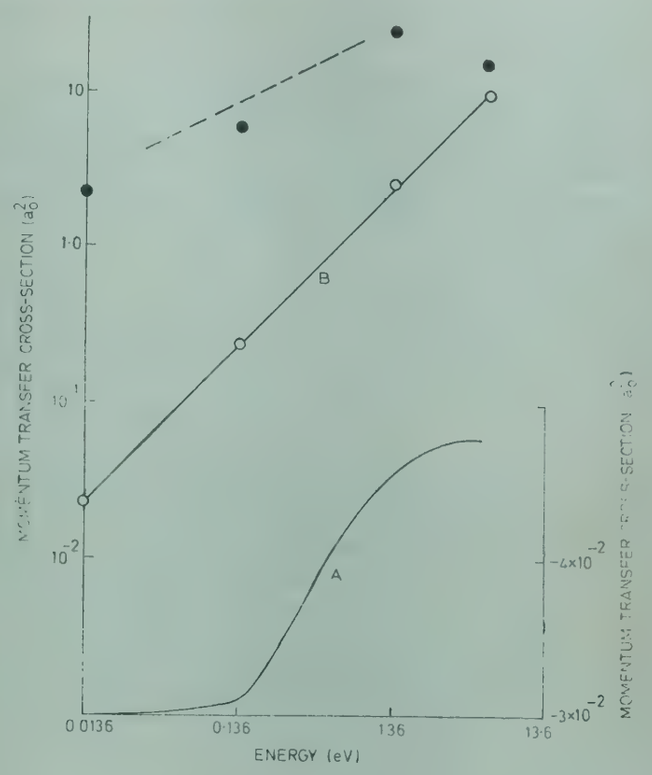

Fig. 5—(A) Momentum transfer cross-sections for the 1→3 transition; (B) the experimental and theoretical momentum transfer cross-sections for the 1→1 transition [●, experimental results of Hake and Phelps[17] and — — — —, theoretical results of Chang[16]]

The momentum transfer cross-section curve for the 1→1 transition is in good agreement qualitatively with the theoretical curve of Chang,[16] though it differs in magnitude. The absence of short-range interaction (which is bound to lower the cross-section results) in Chang's treatment is responsible for the discrepancy. The results of the present work are, in general, not in good agreement with the experimental results of Hake and Phelps.[17] A part of this discrepancy is certainly due to errors in the experimental work.[16]

In the circumstances stated above, the present results for the momentum transfer cross-sections seem to be quite reliable.

References

1. Oksyuk Yu D, *Soviet Phys. JETP*, **22** (1966), 873.
2. Takayanagi K, *Rep. Inosph. Space Res. Japan*, **19** (1965), 1.
3. Takayanagi K & Geltman S, *Phys. Rev.*, **138A** (1965), 1003.
4. Geltman S & Takayanagi K, *Phys. Rev.*, **143** (1966), 25.
5. Fisk J B, *Phys. Rev.*, **49** (1936), 167.
6. Mjosness R C & Sampson D H, *Phys. Rev. Lett.*, **13** (1966), 812.
7. Takayanagi K & Itikawa Y, *Adv. atom. molec. Phys.*, **6** (1970), 105.

8. Arthurs A M & Dalgarno A, *Proc. R. Soc.*, **A256** (1966), 540.
9. Blatt J M & Biedenharn L C, *Rev. mod. Phys.*, **24** (1952), 258.
10. Sams W N & Kouri D J, *J. chem. Phys.*, **51** (1960), 4809.
11. Pande A K & Singh R S, *Indian J. pure appl. Phys.*, **15** (1977), 493.
12. Pande A K & Singh R S, *J. Phys.*, **B11** (1978), 1623.
13. Sunshine G, Aubrey B B & Bederson B, *Phys. Rev.*, **154** (1967), 1
14. Salop A & Nakano H H, *Phys. Rev.*, **A2** (1970), 127.
15. Hall R I & Trajmar S, *J. Phys.*, **B12** (1975), L 293.
16. Chang E S, *Phys. Rev.*, **A9** (1974), 1944.
17. Hake R D & Phelps A V, *Phys. Rev.*, **158** (1967), 70.

Indian Journal of Pure & Applied Physics
Vol. 18, June 1980, pp. 413-418

Measurement & Analysis of Solar Radiation & Illumination for Clear Sky Conditions

M CHANDRA

Central Building Research Institute, Roorkee

Received 26 *July* 1978; *revised received* 23 *November* 1979

Simultaneous measurements of solar radiation and illumination carried out over a period of nearly three years at Roorkee for clear sky conditions have been analyzed and a set of empirical expressions are obtained for the direct and diffuse components of solar radiation and illumination. Different expressions, in sine functions of solar altitude, are given for three different ranges of atmospheric turbidity specified in terms of Linke's new turbidity factor. These expressions are useful for the calculation of thermal radiation and illumination quantities for practical problems, e.g. in the design of buildings. The values of luminous efficiency for the two components of solar radiation determined from these measurements are also given. A knowledge of luminous efficiency can enable the conversion of relatively abundant solar radiation data in to illumination data which are scarce.

1. Introduction

An important requirement for the design of the thermal and visual environments in buildings is the knowledge of climatological factors which influence the internal environment. Of these, thermal and visual components of radiation from the sun and the sky are of particular significance. Simple methods for the calculation of solar radiation and illumination intensities are, therefore, needed to solve the problems related to functional efficiency of buildings. If the radiation and illumination quantities are expressed as functions of solar altitude and atmospheric turbidity, these quantities, on any plane of inclination, can be easily assessed with reasonable accuracy for any plane, season and time. In this direction, empirically established relationships can play an important role. In the past, several workers have attempted to evolve computational methods for these quantities.[1-5] However, these methods are generally applicable for certain places or regions only and accordingly have their own limitations. Interrelationships between different components of solar radiation have also been attempted to facilitate the use of solar radiation data in localities where estimates of long term average total radiation are available.[6,7] The present study deals with simultaneous measurements of solar radiation and illuminations (on a horizontal surface) for clear (cloudless) sky conditions covering wide range of atmospheric turbidity. Based on these measurements, polynomial expressions in sine functions of solar altitude for the direct and diffuse components of both the solar radiation and illumination have been established separately for three distinct ranges of atmospheric turbidity specified in terms of Linke's new turbidity factor.[8-10]

Often, long term solar radiation data collected and processed by meteorological departments are readily available in suitable form. But similar illumination records are not available as they do not figure in the routine observational programmes of climatological elements. In view of this, attempts have been made to derive natural illumination intensities from solar radiation data. In the absence of measured data on illumination, the International Commission on Illumination (CIE) also favours this method. Based on this approach, the illumination climate in USSR has been classified into five luminous climatic zones.[11] For such conversions, a knowledge of values of luminous efficiency of solar radiation to a certain degree of accuracy is essential. Some workers have reported the values of luminous efficiency for certain European cities.[5,12-15] In the tropics, practically no attempt was made to determine it except for some approximate and indicative results.[16] In view of the demand for illumination data, the luminous efficiency of both the direct and diffuse solar radiation derived from above measurements are presented in this paper.

2. Atmospheric Attenuation of Solar Radiation

Solar radiation incident on a unit surface normal to sun's rays outside the earth's atmosphere, for mean sun-earth distance, is known as the solar constant.

Its most recent and accepted value, as given by Thekaekara,[17] is 1353 W/m^2 or 1·94 cal cm^{-2} min^{-1}. The solar light constant calculated by the present author from Thakaekara's extra-terrestrial spectral irradiance comes out to be 127·1 klux.

While passing through the earth's atmosphere, the direct solar beam interacts with the atmospheric constituents like air molecules, aerosols, water vapour, ozone, etc. Thus the incoming solar energy is partly scattered, partly absorbed, and partly transmitted as direct component. On the earth's surface, the proportion of the direct and diffuse components depends on the angular height of the sun above the horizon and concentration of the atmospheric elements, i.e. turbidity conditions.[18] Therefore, both the direct and diffuse components of solar radiation and illumination available on the earth's surface should be expressible as functions of solar altitude and atmospheric turbidity.

3. Spectral Luminosity and Luminous Efficiency of Solar Radiation

On the earth's surface, the spectral composition of solar radiation may vary from about 0·30 μ in the ultraviolet region to about 3·0 μ in the infrared region. The human eye can perceive energy in the wavelength region from about 0·38 to 0·78 μ only. The relative sensitivity of normal-light adopted human eye is different at different wavelengths in this region and is represented by relative spectral luminosity function $V(\lambda)$. The variation of $V(\lambda)$ for photopic vision (Ref. 19) is shown in Fig. 1. Its absolute values are obtained by multiplying $V(\lambda)$ with a constant factor K_{max} (=680 lumens/W$\approx$ 475 klux/cal cm^{-2} min^{-1}). Thus the luminous efficiency of solar radiation can be mathematically represented by the expression

$$K = \frac{K_{max} \int_{0.38}^{0.78} V(\lambda)\, I_\lambda\, d\lambda}{\int_0^\infty I_\lambda\, d\lambda} = \frac{E}{I} \qquad \ldots(1)$$

where I_λ is the spectral solar energy and E and I are the simultaneously available integral illumination and radiation, respectively.

4. Measurement of Solar Radiation and Illumination

Instantaneous spot measurements were carried out simultaneously for global and diffuse solar radiation and illumination on a horizontal surface. The experimental arrangement is shown in Fig. 2. A Moll-Gorczynski Pyranometer called solarimeter[20] and a selenium photocell were mounted side by side on an adjustable tilt table which was held in the horizontal position for the measurements presented here. Measurements were carried out on the terrace of the Physics Laboratory of the Central Building Research Institute, Roorkee, so as to provide unobstructed view of the whole sky vault to the sensing elements

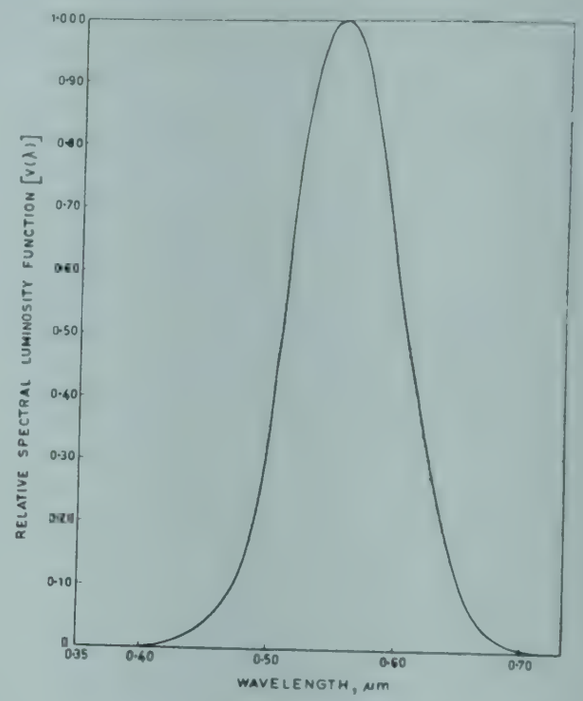

Fig. 1—Relative spectral luminosity function at different wavelengths in the visible region

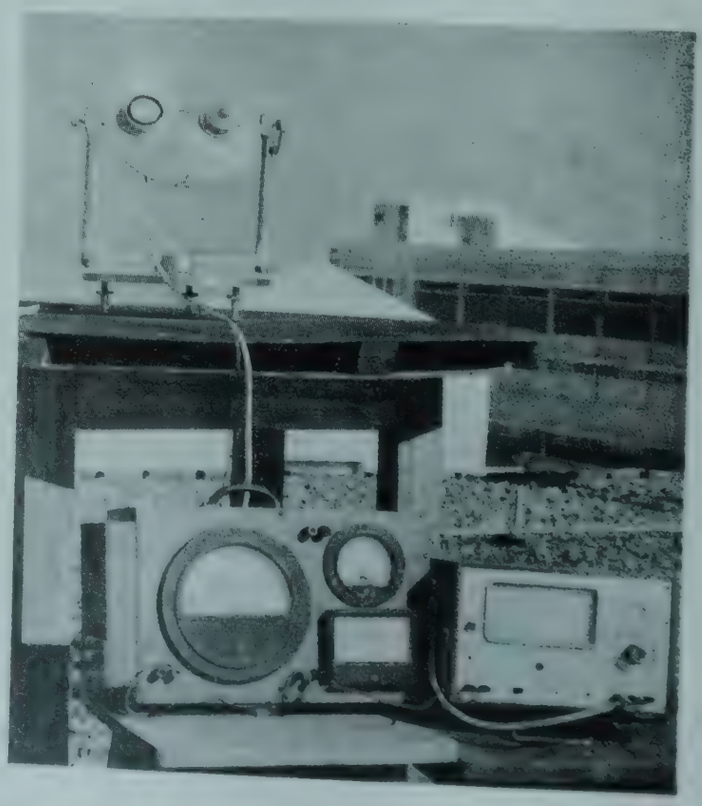

Fig. 2—Arrangement for simultaneous measurement of solar radiation and illumination

of solarimeter and photocell. Nearby was a building subtending an angle of approximately 1 degree from the measuring spot. This will have practically no effect on the accuracy of measured values. The diffuse solar radiation and illumination were obtained by shading the sensitive elements by means of a blackened circular disc of appropriate diameter. The outputs of the solarimeter and photocell were recorded by means of suitable meters.

5. Results and Discussion

The radiation and illumination values measured at different solar elevations were divided into three different ranges of atmospheric turbidity specified in terms of Linke's new turbidity factor T. This has the advantage of representing atmospheric turbidity conditions with a single meteorological parameter. It is defined as the ratio of total extinction coefficient (σ_m) of the actual atmosphere for direct solar beam to that of a standard atmosphere (σ_s) consisting of pure air molecules and 1 cm of precipitable water.[10] Thus

$$T = \frac{\sigma_m}{\sigma_s} = \frac{\log (I_0/I_m)}{\log (I_0/I_s)}$$

or

$$T = \frac{\log I_0 - \log I_m}{\log I_0 - \log I_s} \qquad \ldots(2)$$

where I_0 is the solar constant; I_m is the measured direct solar radiation and I_s that for the standard atmosphere for the same solar elevation as I_m, both at normal incidence. For determination of T, I_m was measured with a Linke and Fuessner actinometer[21] and values of I_s were calculated from more recent available data.[22,23] The three ranges of atmospheric turbidity, namely, $2{\cdot}0 < T < 3{\cdot}0$, $3{\cdot}0 < T < 4{\cdot}0$ and $4{\cdot}0 < T < 5{\cdot}0$ (denoted by T_1, T_2 and T_3) into which the data were broadly divided, may be roughly considered as the representatives of low, average and high turbidity conditions, respectively.

5.1 Direct and Diffuse Solar Radiation

Fig. 3 shows the plot of direct solar radiation (D_H) on a horizontal surface against solar altitude (θ) for the three turbidity ranges mentioned earlier. The direct component was obtained by subtracting the diffuse component from the global radiation. These data were used for determining the empirical relations for direct radiation intensity on a horizontal surface. As discussed by Spencer,[24] the form of the expression for a horizontal surface was assumed to be polynomial in sine function of solar altitude having no constant and linear terms, i.e.

$$D_H = a_2 \sin^2 \theta + a_3 \sin^3 \theta + a_4 \sin^4 \theta + \ldots \qquad \ldots(3)$$

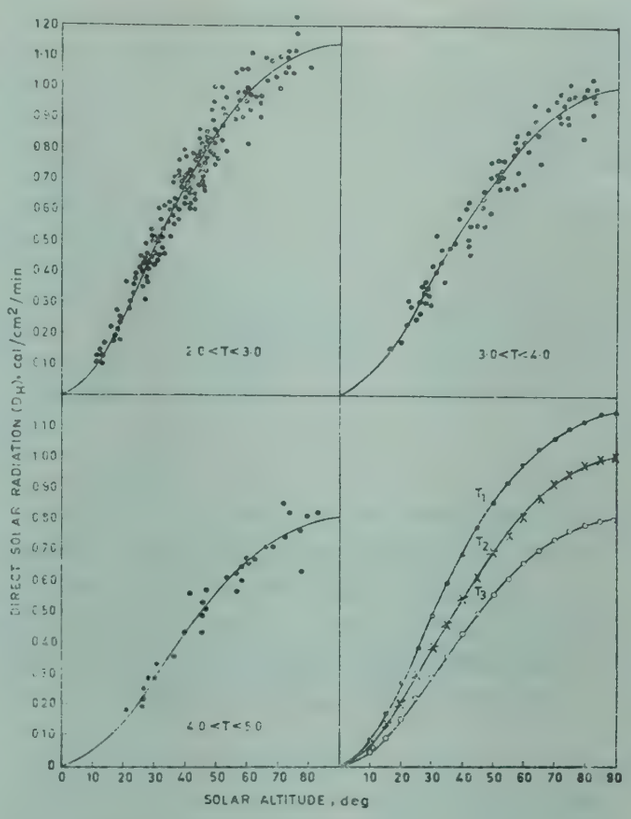

Fig. 3—Variation of direct solar radiation on a horizontal surface with solar altitude for different turbidity conditions

From this it is easy to derive an expression for the radiation intensity normal to sun's rays which is often more convenient for calculating direct solar radiation on inclined planes. In the above polynomial expression [Eq. (3)], constants a_2, a_3, a_4,...etc. (regression coefficients) were evaluated by fitting the data in the expression and applying the least squares criterion for obtaining normal equations which were solved by the matrix inversion method. Polynomials containing different number of terms were tried. Keeping in view the reasonable accuracy, etc. the following expressions were finally chosen.

For $2{\cdot}0 < T < 3{\cdot}0$

$$D_{H,1} = 3{\cdot}27 \sin^2 \theta - 3{\cdot}17 \sin^3 \theta + 1{\cdot}03 \sin^4 \theta \qquad \ldots(4)$$

For $3{\cdot}0 < T < 4{\cdot}0$

$$D_{H,2} = 2{\cdot}58 \sin^2 \theta - 2{\cdot}68 \sin^3 \theta + 1{\cdot}10 \sin^4 \theta \qquad \ldots(5)$$

and for $4{\cdot}0 < T < 5{\cdot}0$

$$D_{H,3} = 1{\cdot}64 \sin^2 \theta - 1{\cdot}10 \sin^3 \theta + 2{\cdot}64 \sin^4 \theta \qquad \ldots(6)$$

Here the radiation values are in cal cm^{-2} min^{-1}. The corresponding expressions for direct solar radiation normal to sun's rays are found by dividing the right hand side of Eqs. (4), (5) and (6) by the cosine of solar angle of incidence, i.e. $\cos (90-\theta) = \sin \theta$.

In the case of diffuse solar radiation on a horizontal surface, d_H is plotted against solar altitude as in Fig. 4. Though there should not be a constant term in the power series expression to satisfy the

condition of zero diffuse radiation at zero solar altitude, the linear term is not precluded. In this case, the following expressions were found to represent the data adequately for the above three ranges of turbidity respectively.

$$d_{H,1}=0{\cdot}745 \sin\theta - 1{\cdot}56 \sin^2\theta + 1{\cdot}85 \sin^3\theta - 0{\cdot}767 \sin^4\theta \quad ...(7)$$

$$d_{H,2}=0{\cdot}816 \sin\theta - 1{\cdot}30 \sin^2\theta + 1{\cdot}45 \sin^3\theta - 0{\cdot}657 \sin^4\theta \quad ...(8)$$

$$d_{H,3}=1{\cdot}64 \sin\theta - 5{\cdot}13 \sin^2\theta + 7{\cdot}31 \sin^3\theta - 3{\cdot}41 \sin^4\theta \quad ...(9)$$

5.2 Direct and Diffuse Solar Illumination

The direct illumination E_H and diffuse illumination e_H on a horizontal surface measured simultaneously along with the solar radiation described in Section 5·1 are plotted against solar altitude on Figs. 5 and 6 respectively. Considerations similar to those

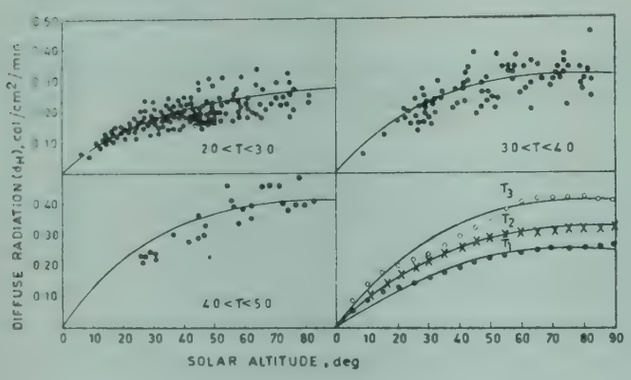

Fig. 4—Variation of diffuse solar radiation on a horizontal surface with solar altitude for different turbidity conditions

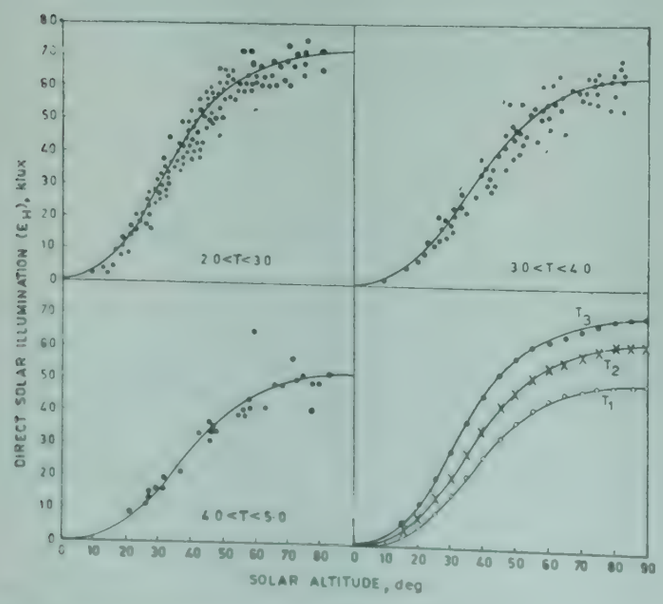

Fig. 5—Variation of direct solar illumination on a horizontal surface with solar altitude for different turbidity conditiosn

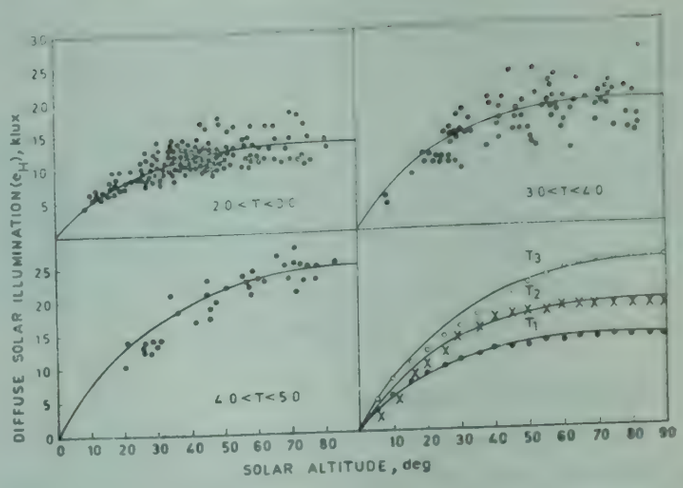

Fig. 6—Variation of diffuse solar illumination on a horizontal surface with solar altitude for different turbidity conditions

of solar radiation led to the following expressions for the two components of solar illumination.

For direct solar illumination

$$E_{H,1}=109{\cdot}2 \sin^2\theta - 110{\cdot}6 \sin^3\theta + 557{\cdot}3 \sin^4\theta - 536{\cdot}4 \sin^5\theta \quad (10)$$

$$E_{H,2}=116{\cdot}1 \sin^2\theta - 414{\cdot}8 \sin^3\theta + 1414{\cdot}6 \sin^4\theta - 1745{\cdot}3 \sin^5\theta + 692{\cdot}6 \sin^6\theta \quad ...(11)$$

$$E_{H,3}=5{\cdot}0 \sin^2\theta + 193{\cdot}8 \sin^3\theta - 148{\cdot}6 \sin^4\theta \quad (12)$$

For diffuse solar illumination

$$e_{H,1}=37{\cdot}7 \sin\theta - 51{\cdot}6 \sin^2\theta + 39{\cdot}4 \sin^3\theta - 12{\cdot}3 \sin^4\theta \quad ...(13)$$

$$e_{H,2}=24{\cdot}2 \sin\theta + 30{\cdot}9 \sin^2\theta - 64{\cdot}9 \sin^3\theta + 27{\cdot}5 \sin^4\theta \quad ...(14)$$

$$e_{H,3}=58{\cdot}2 \sin\theta - 114{\cdot}8 \sin^2\theta + 153{\cdot}2 \sin^3\theta - 71{\cdot}7 \sin^4\theta \quad ...(15)$$

The values of illumination calculated from these expressions are in the units of klux. The expressions for direct solar illumination at normal incidence are obtained by simply reducing the power of sin θ by unity in each term of the Eqs. (10), (11) and (12).

5.3 Determination of Luminous Efficiency

From the simultaneously measured radiation and illumination quantities, the computations for the luminous efficiency of direct radiation (K_D) and of diffuse radiation (K_d), were made from the formulae,

$$K_D = E_H/D_H \quad . \quad (16)$$

and

$$K_d = e_H/d_H \quad .. \quad (17)$$

These values are plotted in Figs. 7 and 8 respectively. Lot of scatter is observed in the luminous efficiency values. Bartineva and Polakova[18] have also reported large scatters. Although the luminous efficiency

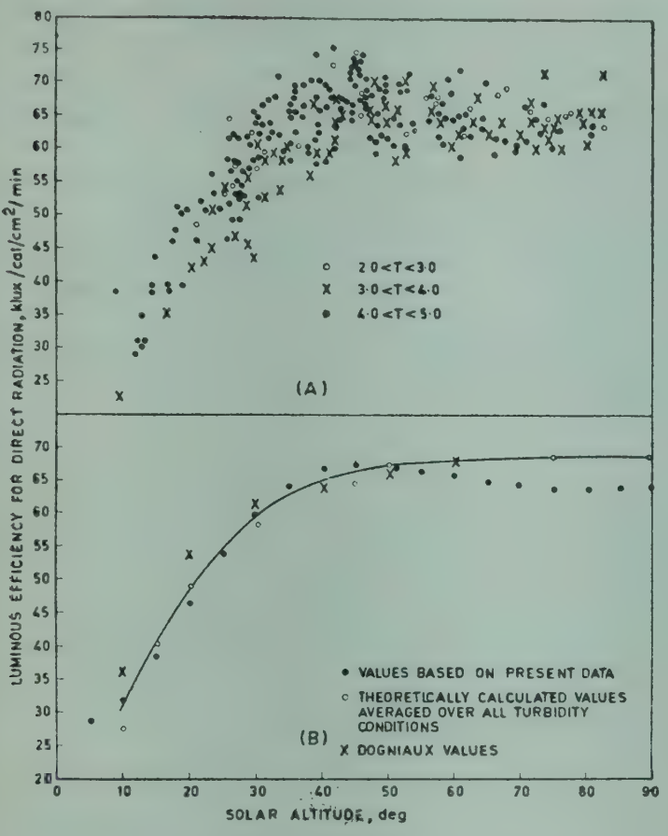

Fig. 7—Luminous efficiency for direct solar radiation for different solar altitudes

depends on turbidity factor, more data will be required for categorizing it in different turbidity ranges. However, average values may be used for most practical purposes. In the case of luminous efficiency for direct component, a least square polynomial in sin θ as given below was obtained

$$K_D = 32{\cdot}2 \quad 87{\cdot}7 \sin\theta + 644{\cdot}8 \sin^2\theta - 905{\cdot}8 \sin^3\theta + 308{\cdot}7 \sin^4\theta \qquad (18)$$

The values calculated from this expression are plotted in Fig 7(B). In this figure the values reported by Dogniaux[14] and those calculated by the author[25] averaged over all conditions of the atmosphere, are also plotted. The solid curve may finally be considered for practical use.

In the case of luminous efficiency for diffuse radiation, there does not seem to be any significant variation with solar altitude as shown on Fig. 8. An average value of 58·5 klux/cal cm^{-2} min^{-1} is good enough for practical use under all conditions in the tropics.

6. Conclusion

Empirical relations have been obtained for direct and diffuse components of both solar radiation and illumination for different turbidity ranges under tropical clear sky conditions. These formulae have

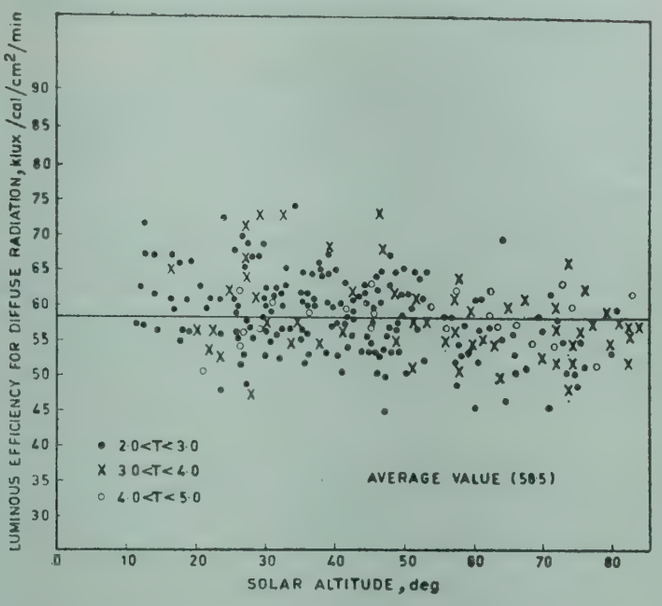

Fig. 8—Luminous efficiency of diffuse solar radiation for different solar altitudes

wider scope from the application point of view compared to those either based on visual classification of sky conditions or limited to typical regions.

The values of luminous efficiency given in this paper may be considered as the representative values for tropical conditions for the conversion of solar radiation data into natural illumination.

Acknowledgement

The author wishes to thank Dr B K Saxena for his keen interest and help during the course of this study. The paper forms part of the research activities of the Central Building Research Institute, Roorkee, and is published with the permission of the Director.

References

1. Moon P, *J. Franklin Inst.*, 230 (1940), 583-617.
2. Elvegrad E & Sjostedt G, *Illumin. Engg.*, 35 (1940), 333.
3. Pleizel G, *Victor petterson bokindustri actibolog, Stockholm*, 1954.
4. *Proc. Commission Internationale de L' Eclairage, Inter sessional Conf Bouwcentrum, Rotterdam*, 1967.
5. Chrocicki W, *Teaching the teachers, colloquium on building climatology, Stockholm*, 1972.
6. Liu B Y H & Jordan R C, *Solar Energy*, 4 (1960), 1.
7. Parmelee G V, *American society of heating and ventilating engineers*, 60 (1954), 341-358.
8. Linke F & Boda K, *Meteor. Z.*, 39 (1922), 161.
9. Linke F, *Beitr. Phys. Freien Atmosphaire*, 15 (1929), 176.
10. Linke F, Die sonnenstrahlung und ihre schivachung in der atmosphaire, in *Handbuch der Geophysik* (Borntrager, Berlin), 8 (1942), 281.

11. *Commission Internationale de L'Eclairage*, Publication No. 14B (1968), 448.
12. Krochman J, *Lichttecknik*, 16 (1964), 585-590.
13. Bartineva O D & Polakova E A, *Proc. Main Geophys. Observatory*, No. 169 (in Russian), 1965.
14. Dogniaux R, Publication, Serie B, No. 12, IRM de Belgique, 1954.
15. Kimbal H H, *Month. Weath. Rev.*, 52 (10), 1924.
16. Narsimhan V & Sarvender Kumar, *Indian J. Met. Geophys.*, 16 (1965), 677.
17. Thekaekara M P, *Solar Energy*, 14 (1973), 109-127.
18. Chandra M, *Mausam*, 30 (1979), 415-422.
19. List R, *Smithsonian Met. Tables*, (1958), 452.
20. Courvoisier P & Wierzejewski, *Arch. Meteor. Geophys. Bioklimatol., Ser. B*, 1 (1948), 45-53; 1 (1948), 156-99.
21. Robinson N, *Solar Radiation* (Elsevier, Amsterdam), 1966.
22. Chandra M, *Indian J. pure appl. Phys.*, 15 (1977), 804.
23. Yamamoto G, *J. atmos. Sci.*, 19 (1962), 182.
24. Spencer J W, *Council of scientific and industrial Research organization, Australia*, Div. Build. Res., Tech. paper 15, 1965.
25. Chandra M, *Indian J. Met. Hydrol. Geophys.*, 29 (1978), 667.

Indian Journal of Pure & Applied Physics
Vol. 18, June 1980, pp. 419-428

Laser Power Fluctuations due to Striations in a He-Ne Laser Operating at 6328 Å

V D Dandawate
Length Standard, National Physical Laboratory, New Delhi

Received 7 *May* 1979

The output radiation of a gas laser, in general, is associated with the undesirable noises of regular or irregular nature. Though a large number of factors are responsible for this noise, the generation of oscillations of kHz range in the discharge current stands out to be the most serious one. Study of the effect of these oscillations on the discharge tube current, the side light and laser output, has beeen carried out using number of discharge tubes having different dimensions and filled at different pressures of He-Ne gas mixture. The dependence of these oscillations on such factors as the discharge current, filling pressure, nature of cathode, etc. has been examined. Various theories put forward to explain the generation of the current oscillations, moving striations and modulation of laser output have been discussed and in the light of the present experimental results a unified picture of the mechanism involved is prescntcd.

1. Introduction

Laser power output, in general, is known to be noisy with several sources for its generation. Spontaneous emission noise,[1] mode interaction instabilities,[2-4] change in optical length of the cavity due to mechanical disturbances or other reasons,[5] electrical disturbance from power supply or interelectrode capacitance,[6-8] and plasma instabilities[9-13] are some of the causes for these noises.

Among these, the noises of both regular and irregular nature, arising from the modulation of current due to plasma oscillations, are found to be mainly responsible for the amplitude fluctuations in the laser power output.[11,14-17]

These plasma oscillations in discharge tubes have been observed and studied by several workers in the past.[18-21] A plasma discharge tube is also used, in a gas laser, to provide an amplifier medium and it is imperative that it should have minimum noise when a stable laser output is required. Such low-noise-laser-output is essential in many applications of laser, the laser standard of length is one such application.

Under the programme of development of frequency stabilized He-Ne laser, a study was carried out to determine the parameters on which this noise generation depends. The results of this study are reported in this paper with suitable explanations for the observed phenomena.

2. Experimental Arrangement

Fig. 1 gives the block diagram of the experimental set-up used during these investigations. The He-Ne laser discharge tube is excited by a high voltage dc power supply with suitable ballast resistances in series. To detect the oscillations in current, a resistance of 1kΩ is connected in series with the tube on the cathode side, and the output across this resistance is observed on one channel of a double beam oscilloscope.

The fluctuations in the laser power output are detected by passing the beam through an aperture, a red filter and a diffusor on to a photo-multiplier-tube (PMT). A second PMT with a fine vertical slit in front of it is used to examine the spontaneous light emitted through the side walls of the discharge tube The outputs of these two PMTs are observed on a double beam oscilloscope.

Laser discharge tubes with internal and external mirrors, with different types of cathodes, of different lengths and capillary diameters, filled at different

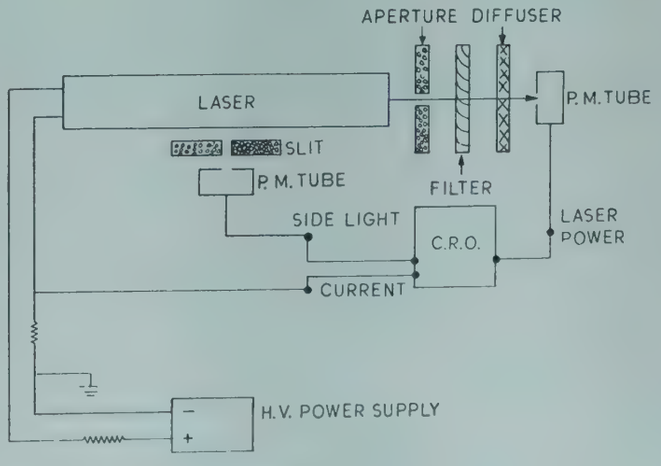

Fig. 1—Block-diagram of the experimental set-up

pressures of helium-neon mixture, were used in this investigation. These details of the different tubes and the observations made are reported in the next section.

3. Results

3.1 Tube No. 1

This is an internal mirror laser with cavity length 270mm and capillary diameter 1·7mm. The cathode is an aluminium tube 100mm long and 12mm internal diameter; a short nickel wire serves as the anode. The tube is filled with a mixture of helium and neon in 9:1 ratio, at a pressure of 2·5 torr. It is excited by a stabilized high voltage power supply with ripple content less than 35mV.

The discharge current is found to be modulated by two types of oscillations, one in the frequency range of 35 kHz and the other in 1 MHz range. The waveforms of these oscillations are shown in Figs. 2(a)-(c). The frequency and magnitude of the first type of oscillations vary with the current. The variation of peak-to-peak (P-to-P) amplitude of these oscillations and the percentage modulation due to them, are plotted against the discharge tube current, in Fig. 3.

It may be seen that the magnitude of these oscillations goes on decreasing from 0·55 mA to zero as the current is reduced from 10mA to 4·1mA. From 4·1mA to 3·0mA, the oscillation amplitude is practically zero. These oscillations again start appearing as the current is reduced further, and at 2·7mA, the amplitude is 0·52mA. Though the overall magnitude of these oscillations is same at 9mA as at 2·7mA, the percentage modulation is higher at lower currents.

The amplitude of the second type of oscillations in current (1MHz range) is nearly 1·5% at 10mA and it goes on decreasing with current and is nearly zero below 4·1mA.

Examination of the laser light (PMT output) shows that it is also modulated by similar types of oscillations as in current, and with a similar frequency range, i.e. 35 kHz and 1 MHz. This is shown in Fig. 4. It may be noted that the wave-forms of current and laser light are nearly similar. The only difference is that when current oscillation goes through the increasing part of the cycle, the laser light goes through the decreasing part of the cycle. This is because of the fact that at 7mA tube current, increase in tube current reduces the laser power. This can be seen from Fig. 5, where the variation of laser power as a function of tube current is depicted.

The amplitude of the 1MHz range oscillations in laser light is extremely small and could not be

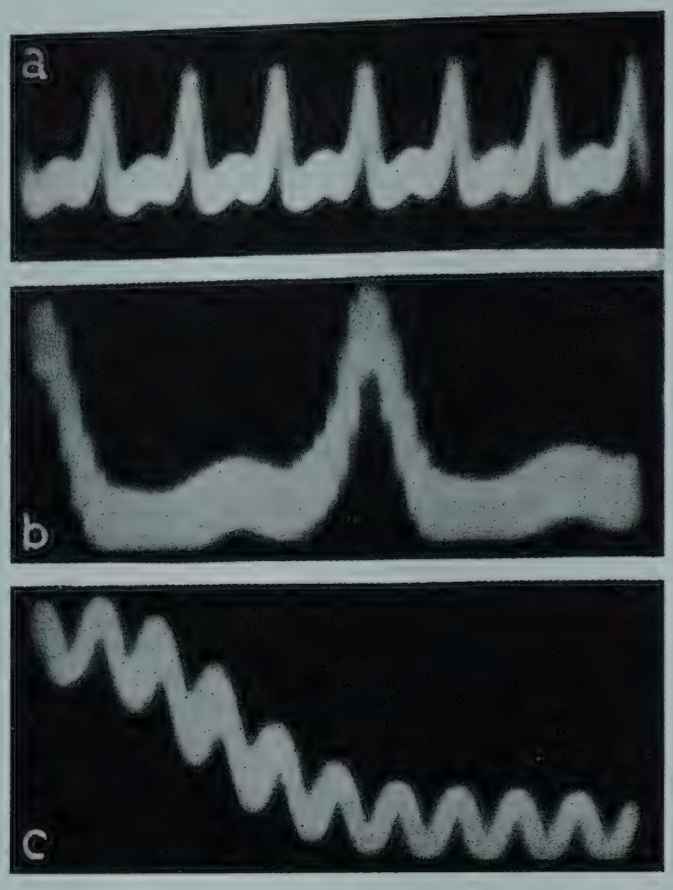

Fig. 2—Photographs showing oscillations in current in the ranges of 35 kHz and 1 MHz
[(a) Sweep duration (S D) 200 μ sec, 7 cycles of 35 kHz oscillations; (b) S D = 50 μ sec, one full and a part cycle of 35 kHz oscillations; (c) S D = 10 μ sec, part of the 35 kHz oscillation cycle showing 10 cycles of 1 MHz range]

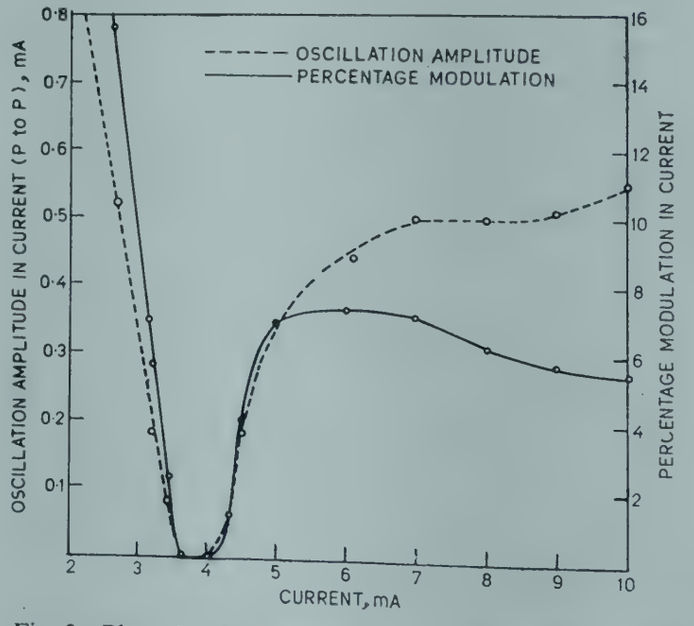

Fig. 3—Plots showing the variation of peak-to-peak (P-to-P) amplitude of current oscillations and percentage modulation in current due to them, with respect to the discharge tube current change

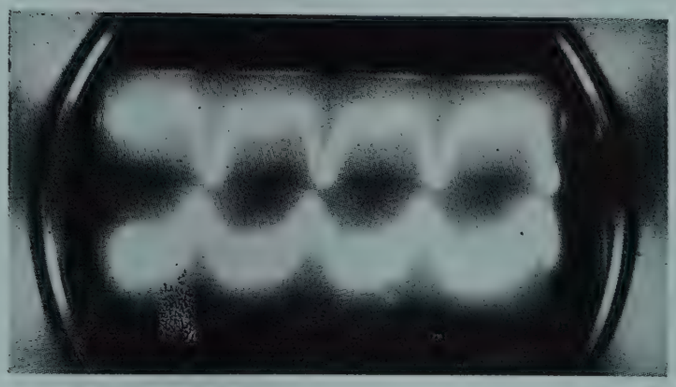

Fig. 4 –Photograph showing oscillations in laser light (upper trace) and in current (lower trace) (light and current both increase downward)

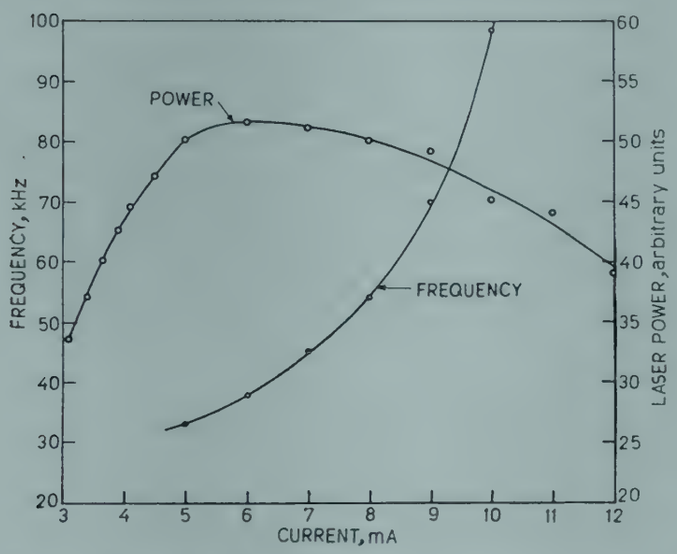

Fig. 5—Plot showing the variations of oscillations frequency and laser power with respect of the laser tube current change

measured. The amplitude of the 35kHz frequency range oscillations varies with current. This variation, and the percentage modulation of laser light, are plotted in Fig. 6 as the discharge tube current is varied from 2·7mA to 10mA. It may be noted that these oscillations are present from 4·1mA to 10mA and again between 3mA to 2·7mA. They are absent from 3mA to 4·1mA, when the current oscillations are also absent. The percentage modulation is larger on the lower current side than on the higher current side.

Examination of the side light also shows the presence of oscillations of 35kHz range; Fig. 7 shows the waveforms of side light (side PMT). There is a difference in the current and side light waveforms; the current waveform is nearly reactangular whereas the side light waveform is nearly sinusoidal.

The variation of the amplitude of the side light oscillations and of its percentage modulation are plotted in Fig. 8 with respect to the tube current changes from 2·7mA to 10mA. Oscillations are

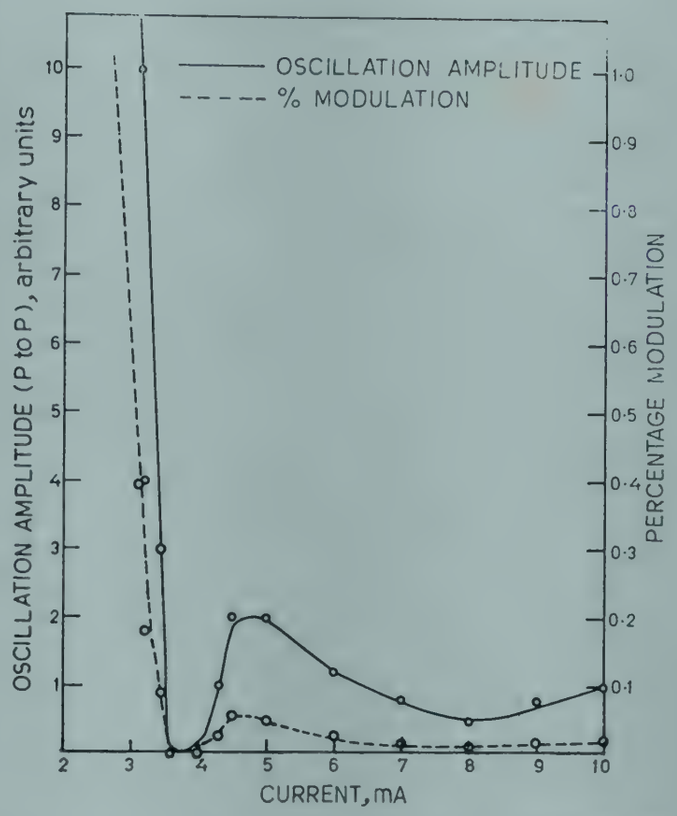

Fig. 6—Plots showing the variation of amplitude (P-to-P) of laser light oscillations and the corresponding percentage modulation due to them in laser light, with respect to the variation of laser tube current

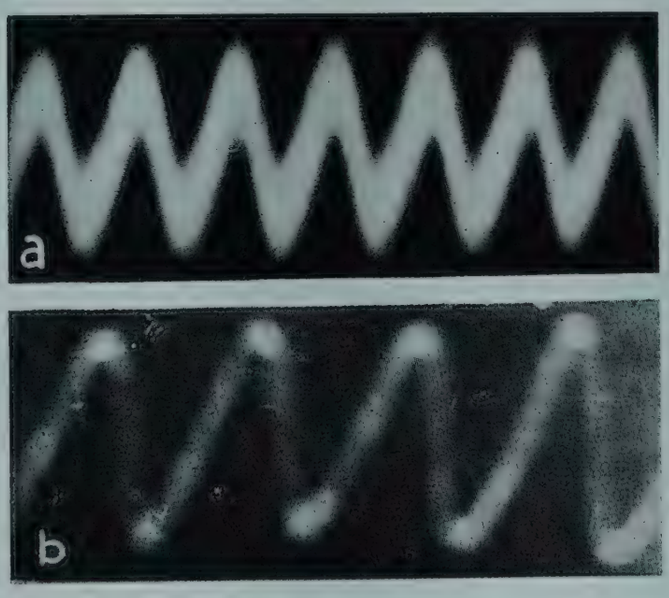

Fig. 7—Photographs showing the oscillations in side light S D = 200 μ sec (a) Number of sweeps superimposed over each other and (b) only one sweep change

again absent between 3·7mA and 4·1mA and their amplitude goes on increasing on either side of the current.

The above observations indicate that the oscillations of the kHz range in current, laser power, and side light, have same frequencies and variation in

their amplitudes follow more or less the same trend, when the tube current is changed. However, whereas the amplitudes of current (Fig. 3) and side light oscillations (Fig. 8) go on increasing from 4 to 10mA, the amplitude of laser light (Fig. 6) increases initially from 4 to 5mA and then drops down. It reaches a minimum value at 8mA and then remains costant. The percentage modulation in current increases from 4 to 6mA and decreases afterwards, (Fig. 3). On the other hand, percentage modulation in side light continues to increase from 4 to 10mA (Fig. 8).

The frequency change with the variation of tube current is plotted in Fig. 5. It is seen that the frequency increases with current, and above 10mA these regular oscillations become very irregular and finally noisy.

This type of strong correlation between oscillations in current, laser power and side light has been reported by a number of workers.[5,11,12] Because of such a strong correlationship, we were tempted to study the behaviour of the current oscillations in a few other laser discharge tubes of different designs.

3.2 Tube No. 2

This is an internal mirror laser tube 400mm long and 2mm bore diameter, filled at a pressure of 2 torr with a 9:1 He-Ne mixture, and excited by a dc power supply. The power supply has a 50 cycle ripple of about 3%.

The laser tube when operated, shows the presence of oscillations in the frequency range of about 60 kHz in current and side light. The modulation by these oscillations is measured quite separately

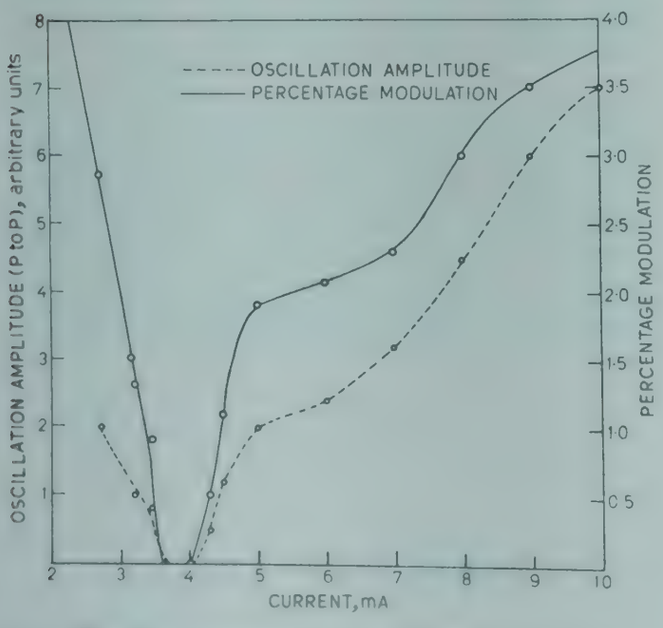

Fig. 8—Plots showing the variations of peak-to-peak (P-to-P) amplitude of oscillations in side light and the percentage modulation in the side light with respect to the variation of laser tube current

from the 50Hz ripple. In current, this modulation varies from 1·5 to 2·5% and in side light from 1 to 1·5%. The frequency oscillations increases with current and above 15mA starts getting noisy.

It was not possible to detect any high frequency oscillations in the laser light as generated by the current oscillations, possibly because of other noises. However, interestingly, it was noticed that when the laser was operated much above the threshold, the laser light occasionally showed the presence of unstable high frequency oscillations of a few hundred kHz which slowly changed to a few hundred Hz range in few seconds and then disappeared. It was ascertained that these oscillations were not due to any mechanical or acoustical disturbance.

Similar observations are reported by Hodara[2] and Zakharenko.[8] Oscillations of this type are attributed to the interaction and random beating among the various modes in which the laser is oscillating. These mode frequencies are not stable and their intermode beat frequencies or some time the beats among the beat frequencies, fall within the response time of the detector for small durations, and sweep through a frequency band.

3.3 Tube Nos. 3 and 4

A one metre long, 3mm bore diameter laser discharge tube (Tube No. 3) having an aluminium cathode (A) (l = 120mm, d = 20mm) and a nickel wire as anode and a second tube (Tube No. 4) 250mm in length and 2mm bore diameter with two different types of cathodes and a common anode were connected to the gas filling system. The two different types of cathodes in tube No. 4 were as follows : the first one (B) was an aluminium electrode of length 80 mm and diameter 17 mm and the second one (C) was the oxide coated 'neon sign' electrode of length 45 mm and diameter 7 mm.

The change in the amplitude of the current oscillations for these three cathodes (A, B, C) at four different gas pressures of He-Ne mixture and at currents ranging from 5 mA to 40 mA, was studied. The results are shown in Fig. 9(a)-(d). The frequencies of the oscillations at a particular current as measured from the oscilloscope traces are also indicated over the curves. The maximum current at which the generation of these oscillations just starts, hence-forth called as threshold current, is plotted as a function gas pressure for two electrodes B and C in Fig. 10.

On examining Figs. 9(a)-(d) and 10, the following conclusions are drawn.

Among the three electrodes considered, the behaviour of the 'neon sign' electrode (C) is best as far

as the threshold current for oscillation generation is concerned; next comes the bigger aluminium electrode (A) and then the smaller aluminium one (B). However, due consideration is also to be given to the pressure at which the laser tube is filled. For pressures up to 2·5 torr and current less than 12 mA the 'neon sign' electrode is better than the other electrodes. But if the filling pressure is above 2·5 torr and operating current more than 15 mA, then the large aluminium electrode generates less noise than the 'neon sign', one. Also, the maximum limit of the amplitude of these oscillations with increasing current, is much less for the electrode (A) than for the other two.

It is also noticed that for same discharge tube configuration, filling pressure and current, the frequency of oscillation depends upon the size of the electrode. A smaller electrode generates higher frequency and vice versa.

For a particular electrode and at a fixed tube current, the frequency of oscillations decreases with increase in pressure. The threshold current, decreases with increase in pressure.

The length of the electrode for a given diameter is known to determine the threshold[5] current; longer the electrode, higher the threshold current. However, with the two electrodes A and B because of the difference in their diameters and being located in different tubes, even with a difference in their length, the difference in threshold current, is negligible. Secondly, oscillations start at lower currents in tube No. 3 with electrode A, only because it is longer than the tube No. 4.[17]

The one meter long discharge tube (Tube No. 3) was operated with the aluminium electrode (A) as a common cathode against two tungstan electrodes located differently. One electrode was located at about 100 mm from the cathode but the discharge glow had to pass through a constriction of about 2 mm diameter and the second one was located at 600 mm from the cathode through a uniform tube of 10 mm diameter. It was noticed that oscillations were

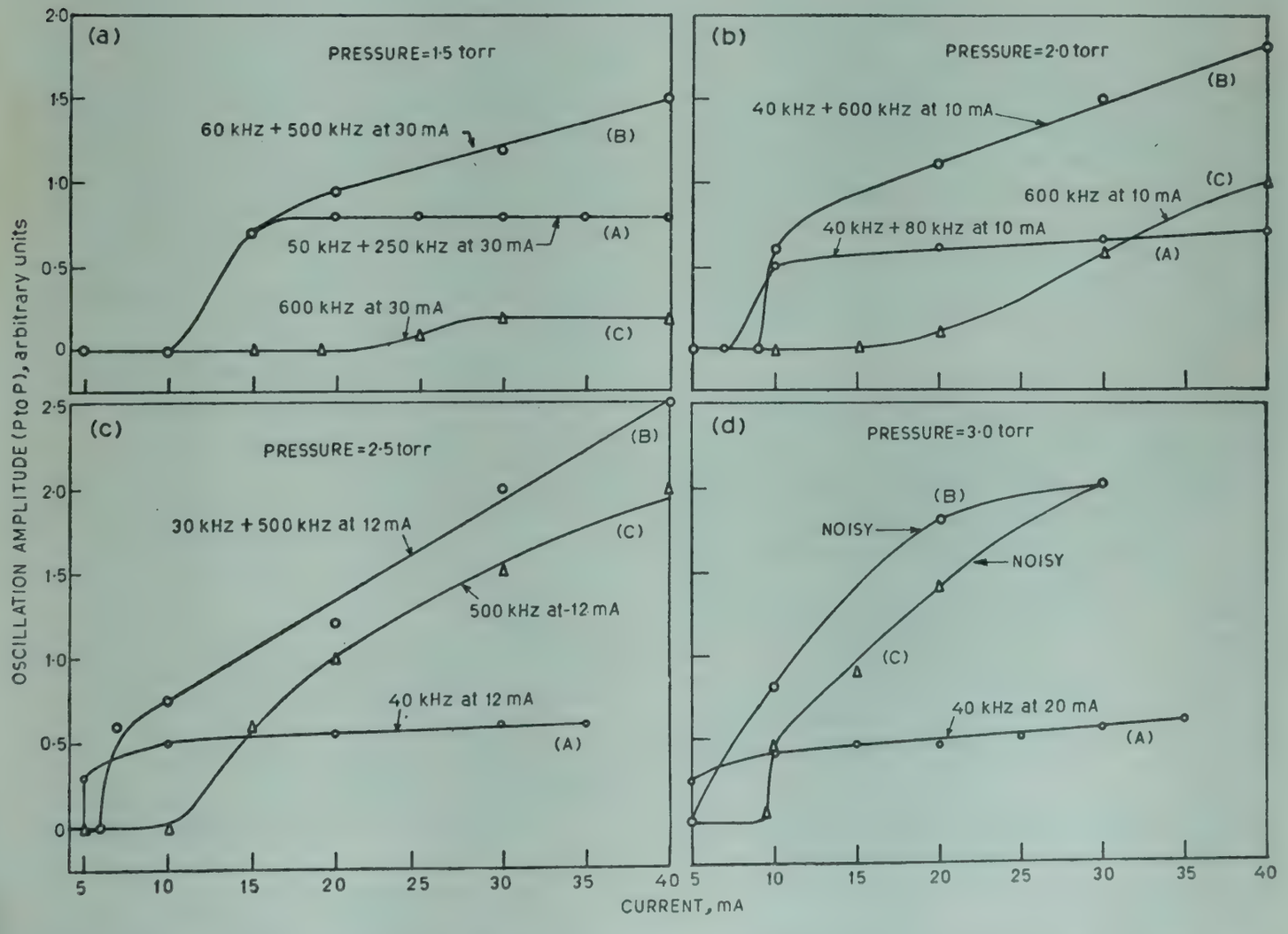

Fig. 9—Plots showing the change in the amplitude (P-to-P) of oscillations in current as the tube current is varied from 5 mA to 40 mA for three electrodes (A), (B) and (C) at pressures of (a) 1·5 torr, (b) 2·0 torr (c) 2·5 torr and (d) 3·0 torr

generated much earlier, had larger amplitude, and higher frequency for the same current and pressures in the first case than in the second one.

4. Discussion

Many theories and mechanisms have been put forward to explain the generation of the current oscillations, moving striations and modulation of laser output. In view of the experimental results of the present work, a coherent picture regarding their generation, factors determining their frequency, etc. is given. Suitable explanations for some phenomena observed earlier as well as in this experiment are also presented.

The primary cause of the generation of current oscillations is the cathode emission fluctuation especially prominent for cold cathodes, where emission is due to ion bombardment.[22] The ion bombardment leads to material transport in the cathode region, thereby changing the emission and corresponding rearrangement of the discharge configuration.

This is supported by the present observations regarding the dependence of these oscillations on the surface characteristics of the cathode, A 'neon-sign' electrode having oxide coated surface, is found to have a much higher threshold current for oscillation generation than a cold aluminium cathode. Also the higher threshold current for a larger area (bigger cathode), means a certain minimum magnitude of current density over the cathode surface, is necessary before the oscillations can start. Above this current density, some cathode instability starts and generates an excess of electrons.

The excess of electrons so generated are accelerated through the cathode fall region and they in turn generate more of positive ions.[13] The movement of this group of positive ions, which is termed as wave of stratification, proceeds towards the cathode. These positive ions, in turn, generate more electrons by secondary effects, and the process continues. Comparing the waveforms of the current oscillation (Figs. 2 and 4) which are more or less rectangular in nature, with the one given by Palmer[23] for the relaxation waveform, it appears that a similar mechanism must be responsible for these oscillations.

Another factor which must be considered is the part played by the atoms in the metastable states. These atoms provide a sizeable number of atoms at a level from where they are excited to higher energy states due to electron collision. But the population of these atoms also fluctuate due to the relaxation processes determined by volume and wall losses. This makes the frequency of oscillations dependent on the gas pressure and the diameter of the discharge tube. They also change the refractive index of the medium causing amplitude and frequency modulation of the laser output.[24]

In Fig. 10, we see that the threshold current for noise-free operation increases with decrease in pressure. A similar relation is obtained by Roza and Salamon[25] for different concentrations of helium and neon. It is seen that for a given gas pressure, the highest threshold current corresponds to the smallest neon concentration and also for a given composition of helium and neon, low pressure favours low-noise operation.

This indicates that a certain minimum concentration of neon atoms in metastable state has to be reached before the oscillations appear. The life-time of helium metastable state 2^1S is known to determine the critical response frequency, above which light output has very little effect.[16] However, their concentration appears to play no part in determining the threshold current or oscillation frequency.

The reason why the threshold current is determined by neon atom concentration and not by helium atoms, may be due to the lower excitation potential of neon metastable state $1s_5$ (13·4 eV) than that of helium 2^1S and 2^3S (16·7 and 16·0 eV). With the current increasing, the minium population of the metastable state atoms necessary for generating the oscillations is reached first for neon than for helium atoms and so the neon concentration determines the magnitude of the threshold current.

The dependence of the oscillation frequency on tube diameter was studied by Suzuki[17] and it

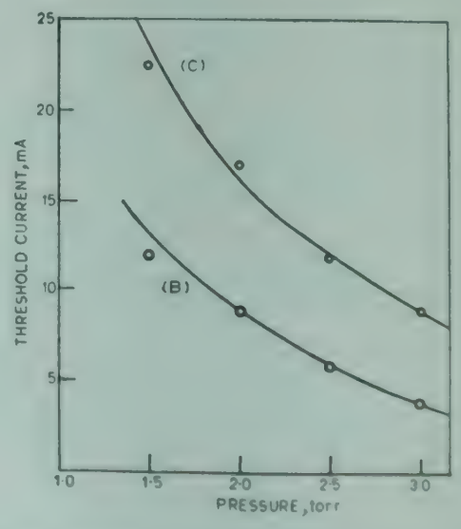

Fig 10—Plot showing the dependence of threshold current on the gas pressure for the two electrodes B and C

was found that the frequency is inversely proportional to the square of the tube diameter. This is due to the faster rate of loss of the metastable atoms in a smaller diameter tube than in a bigger diameter tube. A similar thing happens when there is a constriction in the path of the discharge. This explains the observations for the tube No. 3, as mentioned earlier, that the threshold current for oscillation generation with cathode 'A' is lower and frequency of oscillations higher when operated against the nearer anode with discharge-glow passing through a constriction, than when operated against the second anode with discharge glow passing through a 10 mm diameter tube. Partly, it is also due to an abrupt change in the discharge impedance.[22]

In view of the fact that for identical discharge columns, and identical pressure and current conditions but with different cathode surfaces and dimensions, the frequency of oscillation is different, the mechanism for their generation may be summed up as follows.

The initial cathode instability due to ion bombardment provides the initial signal of ionization wave with frequencies spread over a narrow frequency band, which is different for cathodes of different surface characteristics and dimensions. Within this band, only a few frequencies find the plasma conditions suitable for amplification, i.e. capable to provide enough positive feedback. These conditions are determined by the relaxation effect caused by the recombination energy transfer at the interface of the negative glow and cathode dark space, and also by the metastable state density and the rate at which they are lost at the walls. These ionization waves, thus amplified, travel along the length of the tube as moving striations. The moving striations when passing through the plasma, change the plasma parameters, viz. the electron temperature, the electron density and the electron energy distribution, and in effect the excitation rate of different energy states of the gas. Therefore, the light radiated through the side walls of the discharge tube show the modulation of light intensity at a particular transverse cross-section of the tube as these waves pass across it. This modulation does not come up in the axially emitted light due to the averaging effect. However, the laser light which is emitted along the axis shows this modulation. This is discussed later on.

It appears that most of the earlier work on these oscillations in relation with laser, is limited to the higher current range, from values where the regular oscillations turn into noise, to the value when these oscillations just disappear. Further, there are no data available on the quantitative relationship between the magnitude of current oscillations and laser oscillations.

We have observed that the range of the current over which oscillations are absent is of the order of 0·5 mA, at least for a particular tube (No. 1). For currents lower than this, oscillations are again found to be present (Figs. 3, 6, 8). The magnitude and percentage modulation of these current oscillations go on increasing with decrease in current; the side light oscillations and their percentage modulation vary more or less in the same way. But in the case of oscillations in the amplitude of laser light and its percentage modulation, this rise is very sharp.

The situation when the oscillations are absent has been explained by Palmer.[23] According to him, in all unstriated discharge, the number of electrons reaching the negative glow region are just sufficient to maintain the losses which occur through the several mechanisms in the positive column. On the other hand, in a striated column the number of electrons is more, which in turn generate more number of positive ions.

As the waveforms of current and laser light oscillations are similar, the current oscillations can be mainly considered responsible for the laser power oscillations (Fig 4). From Fig. 5, which shows the variation of laser power as a function of discharge current, one can calculate, for a given discharge current, the magnitude of percentage modulation in laser power as a result of a particular percentage of modulation in current.

On calculation from the curve of Fig. 5, at 3·4 mA discharge current, a modulation of 2·3% in current gives a 2·4% modulation in laser power. However, due to oscillations, the detected modulation in laser power is only 0·09% for 2·3% modulation in current. Similarly, at 7·5 mA discharge current, for 7% current, modulation, the laser power modulation should have been 1%, while the actually observed modulation is only 0·01%.

The explanation lies in the consideration of the part played by the metastable atoms of neon in the $1s_5$ state, in controlling and modulating the gain of the laser. As already indicated, a minimum population density of neon atoms in metastable state is necessary for starting the generation of oscillations. Also it is known, that their population goes on increasing with current and reaches a steady value at a certain current.[24] The reason for an optimum value of current for maximum laser power is due to the bottleneck of neon atoms in the $1s_5$ metastable

state. At lower currents, the excitation of neon atoms to $3s_2$ (the upper laser level) is not enough and an increase in current increases this population. However, for currents more than the optimum, the population at the $2p_4$ (lower laser level) starts increasing due to excitation from the $1s_5$ metastable state, which reduces the gain. The optimum current for the tube No. 1 is around 6 mA as shown in Fig. 5. The neon atom population in $1s_5$ state is saturated at this current and so the percentage modulation in laser light also saturates at this value (Fig. 6).

Similarly, the minimum density of neon atoms in the $1s_5$ state necessary for generating oscillations is attained at currents lower than or at the most, when equal to, the optimum value. Therefore, the magnitude of threshold current for noise generation must be less than or equal to the optimum current. This explains why the threshold current (4 mA) is less than the optimum current (6 mA) in tube No. 1 and is equal to the optimum current, as observed by Waksberg and Wood[7] and also by Herngvist.[22]

For quantitative accounting of the laser light modulation, one should consider the time for which the laser signal reverberates in the cavity, i e the number of passes this signal makes through the striated column during this time. One should also know the velocity and wavelength of the striations and the gain of the medium at that current (dc) which is modulated in space and time by ionization waves.

The expression for the practical gain/unit distance for the laser amplifier medium at the centre of the Doppler broadened line is given by:[26]

$$\alpha = \left(\frac{\log 2}{\pi}\right)^{1/2} \frac{g_2 A_{21}}{4\pi}\left(\frac{N_2}{g_2} - \frac{N_1}{g_1}\right)\frac{\lambda_0^2}{\Delta\nu_D}$$

where, λ_0 is the centre of frequency of the transion, $\Delta\nu_D$ the linewidth, A_{21} the Einstein coefficient for the spontaneous emission, N_2 and N_1 are the populations of the upper and lower energy levels of the laser transition, and, g_2, g_1 the statistical weights of those levels.

In an unstriated uniform column, α can be considered as an invariant along the axis of the column. If L represents the product of the tube length and the number of passes the signal makes before escaping out of the cavity, then the intensity of the signal that emerges out of the cavity is given by

$$I = I_0 e^{\alpha L} = I_0 (1 + \alpha L) \qquad \alpha \text{ being} < 1 \qquad (1)$$

When the column is striated by standing waves, the gain at each point along the gain column varies cyclically due to varying magnitude of $\frac{N_2}{g_2} - \frac{N_1}{g_1}$ over and above the dc component. At any point at a distance of x from the origin it may be represented by $\alpha + \Delta\alpha \sin \frac{2\pi}{\lambda} x$, where Δx is the modulation amplitude of the gain and is proportional to $\Delta\left(\frac{N_2}{g_2} - \frac{N_1}{g_1}\right)$ and λ is the wavelength of the striation. If the length L is taken as,

$$L = n\lambda + \delta$$

where n is an integer, and δ a small fractional wavelength distance, then the intensity of the emerging signal is given by,

$$I = I_0\left(1 + L\alpha + \frac{\lambda\Delta\alpha}{2\pi} - \frac{\lambda\Delta\alpha}{2\pi}\cos\frac{2\pi}{\lambda}\delta\right) \qquad \ldots(2)$$

This output signal is not temporally modulated and only changes in δ due to shift in origin (the point where the initial signal is considered to start) causes fluctuations in the intensity.

In the third case, when the gain column contains moving striations, the velocity of the moving striations is of the order of 5×10^5 cm/sec.[12,17] As the time for which the laser signal reverberates in the cavity is of the order of a fraction of a microsecond, the striations can be considered almost stationary for that time. Therefore, the intensity of the emerging signal is given by an expression similar to (2). However, due to moving nature of striations, δ in it changes continuously with the same frequency as that of the striations.

The dc component of the emerging laser signal is given by $I_0\left(1 + L\alpha + \frac{\lambda\Delta\alpha}{2\pi}\right)$ and a sinusodal component by $\frac{\lambda\Delta\alpha}{2\pi}\cos\frac{2\pi}{\lambda}\delta$. The percentage modulation comes out to be

$$\frac{\lambda\Delta\alpha/2\pi}{1 + L\alpha + \frac{\lambda\Delta\alpha}{2\pi}} \times 100 \qquad \ldots(3)$$

This shows that the percentage modulation directly depends on the wavelength and the difference in the amplification factor at the maxima and minima of the striation.

The change in laser output, due to change in dc current of same magnitude as that of the amplitude of current oscillation, can be calculated from Eq. (1).

Assuming the corresponding change in the amplification factor to be also given by $\Delta\alpha$, the magnitude of percentage modulation comes out to be,

$$\frac{L\Delta\alpha}{1+L\alpha} \times 100 \qquad \ldots(4)$$

Comparing Eqs. (3) and (4) we see that value obtained from Eq. (3) will always be smaller than that from Eq. (4).

This explains how the laser light is modulated due to the presence of moving striations and also why the modulation produced by current oscillations is much less than what is produced by change in dc discharge current as mentioned earlier.

In the case of striations due to standing waves, the emerging laser light will not show any systematic change as there is no systematic change in δ. Fluctuations of random nature, may occur due to random variation in the origin, that is the point where the signal is considered to originate. On the other hand, in the case of moving striations in addition to this random variation of origin, δ in Eq. (2) will also vary periodically due to the movement of the striations. This means that the laser output is more noisy in the case of moving striations than in the case of standing striations.

As the oscillations in current are due to fluctuations in the charge received by the electrode due to ionization waves, their effect on gain is included as $\Delta\alpha$ and so needs no separate consideration.

The side light from the laser discharge tube was examined through a monochromator. This was done to see if any difference existed in the modulation of different energy levels of neon and helium. It was noticed that practically all the spectral lines of helium and neon showed intensity modulation similar to that observed in the total light. There was no apparent difference in the waveshape of modulation for lines originating from different energy levels.

The mechanism involved in the generation of of oscillations below 3 mA in tube No. 1 appears to be different from that for higher currents. There is a complete reversal of phase in the waveform of the current oscillation to that shown in Fig. 2 or 4 and both the laser light and side-light oscillations are nearly sinusoidal in nature. The results of these oscillations are being analysed.

4. Conclusions

The noise generated in the output of a He-Ne gas laser, due to oscillations in kHz range in the current is found to depend upon a number of factors. The geometry of the discharge tube, filling pressure and mixture ratio of the gas, operating current, dimensions,[27,28] and surface characteristics of the electrodes, are some of these factors.

As the first four factors are governed by the requirement of the power output and other such considerations of the laser, it is the proper choice of electrodes which can be used to give noise-free or low noise laser operation. Thus, for tube lengths of the order of 300 mm, operating current less than 12 mA and filling pressure of 2·5 torr of He-Ne mixture, oxide-coated 'neon-sign' electrode as the cathode is quite satisfactory. For longer tubes, higher currents and lower filling pressure, a bigger aluminium electrode should be used.

It appears that for the latter types of tubes, a cathode bigger in size than the usual 'neon-sign' electrode, coated with an emissive coating may be better. However, these electrodes having oxide coated surfaces may have some detrimental effect on the life of the laser especially compared to the bigger aluminium electrodes.

It is noticed that for a particular laser tube there is a current region, where oscillations in current are practically absent. They are present for currents larger or smaller than this. The value of the current in this region is always less than or equal to the optimum current corresponding to the maximum laser power.

Thus, to have maximum laser power free from noise, it is necessary that the electrode parameters be so adjusted to have the low noise current region, as close to the optimum as possible.

The percentage modulation produced in the laser power output due to oscillations in current is usually less than what it is due to dc variation in the discharge current of the same magnitude. This percentage modulation also depends upon the magnitude of operating current of the tube.

Acknowledgement

The author is extremely thankful to Dr D Sen for his encouragement and valuable discussions during the course of this work and to Dr S R Das for many useful suggestions in the preparation of the manuscript. The paper is being published with the permission of the Director, National Physical Laboratory, New Delhi.

References

1. Prescott L J & Van Der Ziel A, *Physics Lett.*, 12 (1964), 317.
2. Hodara H, *IEEE J. Quant. Electron.*, QE-2 (1966), 337.
9. Harriott D R, *J. opt. Soc. Am.*, 52 (1962), 31.

4. Hongo S, Kubo U & Iniushi Y, *Technol. Rep. Osaka Univ.*, 19 (1969), 833.
5. Wallard A J & Woods P T, *J. Phys.*, E7 (1974), 209.
6. Guskov L N, Sologub V P & Troshin B I, *Opt. Spectrosc.*, 40 (1976), 94.
7. Waksberg A & Wood J, *Rev. scient. Instrum.*, 40 (1969), 1306.
8. Zakharenko U G & Privalov V E, *Opt. Spectrosc.*, 27 (1969), 447.
9. Garscadden J, *J. appl. Phys.*, 35 (1964), 3432.
10. Garscadden J, *Appl. Phys., Lett.*, 8 (1966), 85.
11. Prescott L J & Van Der Ziel A, *IEEE J. Quant. Electron.*, QE-2 (1966), 173.
12. Fargo G & Struit M J O, *Electron. Lett.*, 3 (1967), 423.
13. Galehouse D C, Ingard U, Ryan T J & Ezekiel S, *Appl. Phys. Lett.*, 18 (1971), 13.
14. Prescott L J & Van Der Ziel A, *Appl. Phys., Lett.*, 5 (1964), 48.
15. Bellisio J A, Freed C & Hans H A, *Appl. Phys. Lett.*, 4 (1964), 5.
16. Kubo U, Kawabe K & Inushi Y, *Japan J. appl. Phys.*, 5 (1966), 731.
17. Suzuki T, *Japan J. appl. Phys.*, 9 (1970), 309.
18. Roberston H S, *Phys. Rev.*, 105 (1957), 368.
19. Hakeem M A & Robertson H S, *J. appl. Phys.*, 31 (1960), 2063.
20. Donahue T M & Dieke G H, *Phys. Rev.*, 81 (1951), 248.
21. Pekarek L, *Usp. Fiz. Nauk.*, 94 (1968), 463.
22. Herngvist K G, *RCA Rev.*, 30 (1969), 429.
23. Palmer J D, *J. appl. Phys.*, 40 (1969), 369.
24. Arrathoon R & Siegman A E, *Appl. Phys. Lett.*, 13 (1968), 197.
25. Roza K & Salamon T, *Optics Laser Technol.*, 2 (1970), 151.
26. Willett C S, *Introduction to gas lasers population inversion mechanisms* (Pergmon Press, Oxford), 1974, 23.
27. Hochuli U & Haldmann P, *Rev. scient. Instrum.*, 36 (1965), 1493.
28. Hochuli U, Haldmann P & Hradwick D, *IEFE J. Quant. Electron.*, QE-3 (1967), 612.

Indian Journal of Pure & Applied Physics
Vol. 18, June 1980, pp. 429-435

The $\tilde{a}\,^3A''$—$\tilde{X}\,^1A'$ Phosphorescence of Chlorobenzaldehyde Vapours

M K Haque* & S N Thakur

Lasers & Spectroscopy Laboratory, Department of Physics
Banaras Hindu University, Varanasi 221 005

Received 4 *May* 1979 ; *revised received* 14 *June* 1979

The $T_1 \rightarrow S_0$ ($\tilde{a}\,^3A''$-$\tilde{X}\,^1A'$) electronic emission spectra of *o*-, *m*- and *p*-chlorobenzaldehyde have been studied in the vapour phase in an electric discharge with two specific aims, viz. (i) to get the data for as many ground state fundamental vibrations as possible and (ii) to gather information about the conformations of these molecules. It has been observed that the $\tilde{a}\,^3A''$—$\tilde{X}\,^1A'$ phosphorescence system of these molecules consists mainly of the bands involving the in-plane vibrations with only two or three out-of-plane vibrations. Evidences have been found for the trans-O conformation to be more stable in *o*- and *m*-chlorobenzaldehyde.

1. Introduction

The emission from benzaldehyde and its mono-derivatives in an electric discharge tube shows a deep blue colour and it was shown by Stockburger[1] that the emission consists predominantly of the $\tilde{a}$-$\tilde{X}$ phosphorescence with the $\tilde{A}$-$\tilde{X}$ fluorescence appearing only weakly. The strong $\tilde{a}$-$\tilde{X}$ emission from the $n\,\pi^*$ triplet state has been interpreted in terms of a very large rate constant for the singlet-triplet inter-system crossing.[2] It has also been observed that in the $\tilde{a}$-$\tilde{X}$ emission only two of the out-of-plane vibrations (ϕ-CHO torsion and ϕ-CHO wag) are weakly active both in the spectra of benzaldehyde[3] and *p*-fluoro-benzaldehyde.[4]

The electric discharge emission from the isomeric chlorobenzaldehyde vapours has been reported by Juyal and Singh,[5] but they have interpreted all the emission bands in terms of only one electronic transition ($S_1 \rightarrow S_0$). This erroneous interpretation stems from the fact that the separation between the fluorescence and the phosphorescence origin bands is almost equal to the frequency of the C=O stretching vibration in the ground state ($\sim$1700 cm^{-1}) as in the case of benzaldehyde.[1] Also these authors did not make any attempt to look for the emission bands due to two different rotamers, cis-O and trans-O.[6] in the spectra of *o*- and *m*-chloro-benzaldehyde. There are a number of investigations (see Ref. 6-8 for details) on the conformations of *o*- and *m*-chlorobenzaldehydes involving infrared, NMR studies, dipole moment measurements and theoretical calculations, and all of them agree that the trans-O rotamer is more stable in *o*-chlorobenzaldehyde but the conclusions about *m*-chlorobenzaldehyde differ. The main problem with these methods is, however, the interpretation of the experimental data which are based on an average temperature dependent mixture of the two conformers.

The present investigation was started with two specific aims (i) to collect data for as many a ground state vibrational frequencies as possible in the vapour phase and (ii) to gather information about the conformations of *o*- and *m*-chlorobenzaldehyde that give rise to the electronic emission. The $\tilde{a}$-$\tilde{X}$ phosphorescence spectrum is ideally suited for this sort of studies under low resolution because the vibronic bands in this system are much sharper than the fluorescence bands. The ground state vibrational frequencies are available from the $\tilde{A} \rightarrow \tilde{X}$ fluorescence spectrum[9] and together with the $\tilde{A} \leftarrow \tilde{X}$ absorption data[10] it would be possible to supplement the observations from the phosphorescence measurements.

2. Experimental Details

The emission spectra were excited in a Schüler type transformer discharge and experimental details were the same as in the case of *p*-fluorobenzaldehyde.[4] The samples of *o*- and *p*-chlorobenzaldehyde were purchased from M/s Merk-Schuchardt (Germany) and that of *m*-chlorobenzaldehyde from M/s Koch-Light (UK) and these samples were used as such in our in-

*On leave from Bhagalpur University, Bhagalpur 812 007

vestigations. In the case of *o*- and *m*-chlorobenzaldehyde, the sample arm was kept at 0°C in a water bath and the benzene arm was kept at −10°C in a freezing mixture. In the case of *p*-chlorobenzaldehyde, the sample arm had to be heated to 80-100°C while keeping the benzene arm in the freezing mixture. The spectra were recorded on a Fuess glass spectrograph with a slit width of 50 μm on Ilford HP3 photographic plates. Exposures of 7, 9 and 10 hr were required to develop good spectra for *o*-, *m*- and *p*-chlorobenzaldehydes respectively. The iron arc spectra in air were super-imposed in every case as the standard using a slit width of 20 μm and an exposure of 2 sec. The photographic plates were measured on a E 3A-2 Russian comparator with a least count of 0·0001 cm and the uncertainty of measurements is 5 cm^{-1} for the strong bands and 10 cm^{-1} for the weak ones.

3. Description of the Observed Spectra

The vapour emission spectra of all the three molecules show a characteristically strong progression in the ground state C=O stretching vibration (ν_6) upto $v''=4$ in this normal coordinate. The most intense member of the progression corresponds to $v''=1$ in each case (Fig. 1). This observation is in agreement with the theoretical interpretation of McMurry[11] and implies a slight elongation of the C=O bond in the excited electronic state. The pattern of bands lying in the region between the 0_0^0 band and the 6_1^0 band is repeated almost without any change in the regions between the consecutive members of the progression in the C=O stretch (ν_6) as can be seen in Fig. 1. The ground state C=O stretching frequency interval decreases in going to the higher vibrational levels thus indicating that this vibration is not harmonic.

The chlorobenzaldehyde samples used in the present investigation were 98% pure, but the phosphorescence origin band of benzaldehyde and the members of the progression of the C=O stretch also appear weakly in all the three spectra and these have been identified and marked in Table 1 as well as on the prints in Fig. 1 as BZ. No other bands of benzaldehyde, however, appear as impurity bands.

We have identified the 0_0^0 bands of *o*-, *m*- and *p*-chlorobenzaldehyde at 24178, 24949 and 25066 cm^{-1} respectively in good agreement with the corresponding liquid absorption values of 24240, 24940 and 25090 cm^{-1} (Ref. 12) respectively. Most of the intense bands of all the three spectra show two components with a separation of 23 or 24 cm^{-1}. We have taken the higher wavenumber component in each case to correspond to the main band and the other component to be a sequence band.

4. Vibrational Assignments

We have assumed a planar geometry for the three isomeric chlorobenzaldehydes in both the electronic states with the upper electronic state designated as $^3A''$ and the ground state as $^1A'$ in the C_s point group notation. The upper state results from the excitation of an electron from an *n* orbital to a π^* orbital and the transition $^3A''\rightarrow{}^1A'$ ($T_1\rightarrow S_0$) is spin-forbidden. The intensity of the 0_0^0 band of this system is 100 times the intensity of the 0_0^0 band of the $^1A''\rightarrow{}^1A'$ ($S_1\rightarrow S_0$) fluorescence system[9] and this is probably due to a strong spin-orbit coupling as in the case of benzaldehyde.

The bands in the $T_1\rightarrow S_0$ (phosphorescence) emission spectrum of the three molecules have been assigned on the basis of the infrared and Raman spectral studies in the liquid phase,[13] far infrared[6] and ultraviolet absorption[10] studies in the vapour phase. The vibrational numbering is due to Mulliken[14] and differs from that given by Green and Harrison[13] in a few places where we have changed the assignments given by these authors. The main vibronic bands and their assignments are given in Table 1.

4.1 *o*-Chlorobenzaldehyde

The vibronic bands of the $T_1\rightarrow S_0$ emission system can be interpreted in terms of the ground state vibrational intervals due to only one rotamer. At this stage we shall discuss only the intense vibronic bands and the question of rotational isomerism will be taken up in Sec 5. The vibronic assignments are shown in Table 1.

The torsional vibration does not appear in the $T_1\rightarrow S_0$ emission, but a band at 25798 cm^{-1} in the $S_1\leftarrow S_0$ absorption[10] has been identified as due to this vibration giving a ground state vibrational frequency of 103 cm^{-1} in good agreement with 106 cm^{-1} observed in the vapour phase far infrared spectrum by Miller *et al.*[6] who attribute it to the more stable trans-O rotamer.

The vibronic band at at 23969 cm^{-1} is moderately intense and involves a ground state vibrational interval of 209 cm^{-1} and is assigned to the out-of-plane ϕ-CHO wag. This is in good agreement with the values of 211 cm^{-1} obtained from the $S_1\leftarrow S_0$ absorption spectrum[10] and 201 cm^{-1} obtained from the infrared spectrum.[13] Green and Harrison[13] also assign this vibration to an out-of-plane bending mode.

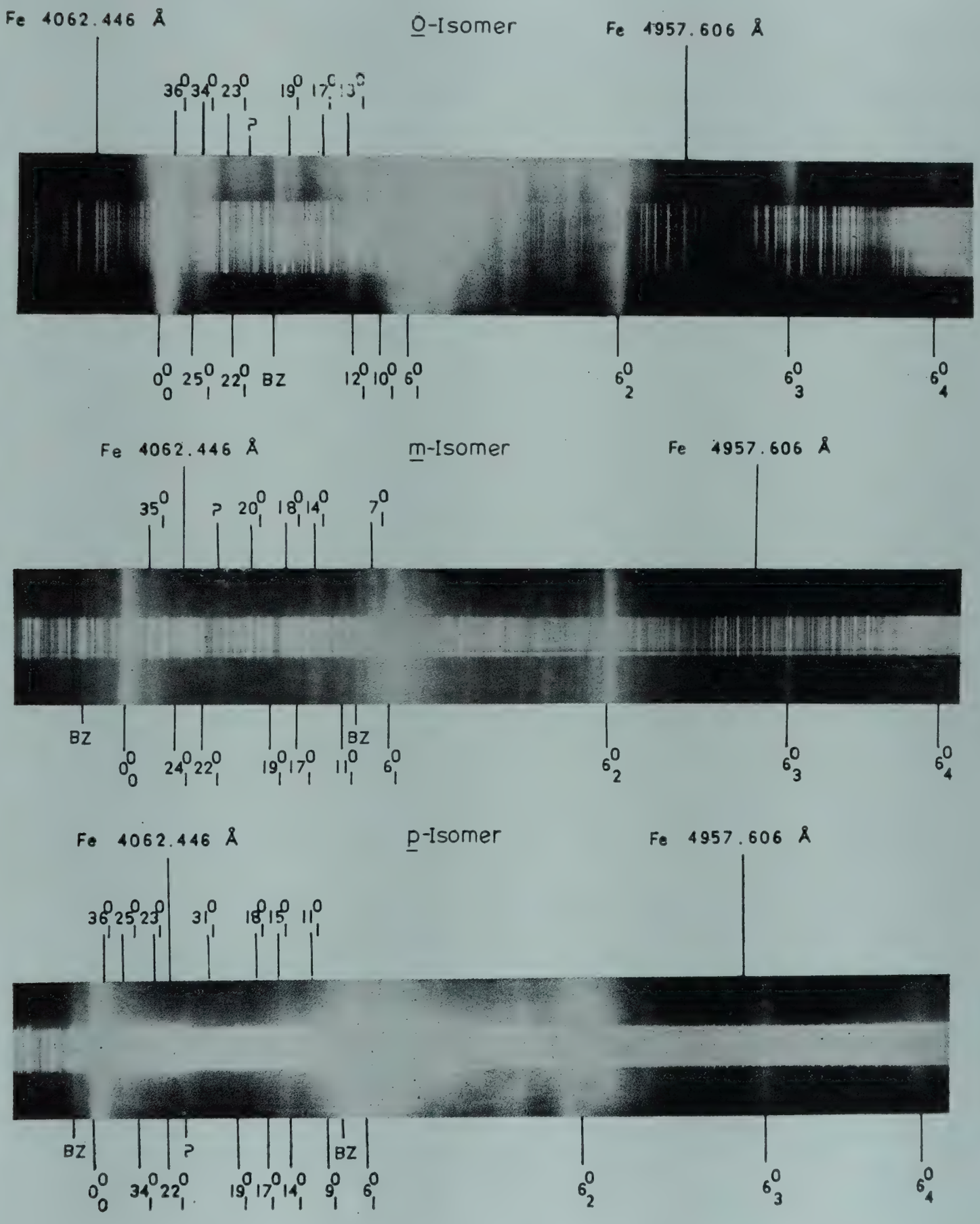

Fig. 1—The $\tilde{a}$-$\tilde{X}$ phosphorescence emission spectrum of *o*-, *m* and *p*-chlorobenzaldehyde

Table 1—Wavenumbers and Assignments of the Principal Band Groups in the $\tilde{a}$-$\tilde{X}$ Phosphorescence Emission Spectrum of *o*-,*m*- and *p*-Chlorobenzaldehydes

Wavenumber* (cm^{-1})	Separation from 0_0^0 band (cm^{-1})	Assignment**	Wavenumber* (cm^{-1})	Separation from 0_0^0 band (cm^{-1})	Assignment**
	o-Chlorobenzaldehyde			*m*-Chlorobenzaldehyde	
24368 (3)	+190	35_0^1	25183 (3·5)		BZ
232 (7)	+54	36_2^2	163 (2·5)		BZ
204 (9)	+26	36_1^1	25102 (3)	+153	35_0^1
178 (10)	0	0_0^0	25071 (4)	+122	25_0^1
154 (9)	−24	35_1^1	24949 (9)	0	0_0^0
125 (7)	−53	35_2^2	26 (8)	−23	35_1^1
23996 (4)	−182	25_1^0	10 (3)	−39	25_1^1
969 (5)	−209	35_1^0	24771 (4·5)	−178	35_1^0
939 (4)	−239	34_1^0	24620 (1)	−329	24_1^0
847 (1)	−337	24_1^0	24570 (1)	−379	23_1^0
765 (2·5)	−413	23_1^0	24492 (0·5)	−457	22_1^0
733 (3)	−445	22_1^0	24374 (3·5)	−575	?
619 (2·5)	−559	?	41 (2·5)	−608	?
580 (2)	−598	?	24264 (0·5)	−685	31_1^0
451 (5)		BZ	24182 (1)	−767	20_1^0
426 (4)		BZ	24082 (1)	−867	19_1^0
339 (4)	−839	19_1^0	21 (1)	−928	27_1^0
316 (2)	−862	29_1^0	23951 (2·5)	−998	18_1^0
157 (2·5)	−1021	18_1^0	23887 (2)	−1062	17_1^0
120 (2)	−1058	17_1^0	50 (1·5)	−1099	16_1^0
064 (1)	−1114	16_1^0	23760 (2)	−1189	15_1^0
22933 (4·5)	−1245	14_1^0	32 (4·5)	−1217	14_1^0
905 (5)	−1273	13_1^0	23644 (1)	−1305	12_1^0
883 (2)	−1295	12_1^0	23565 (2·5)	−1384	11_1^0
757 (3)	−1421	10_1^0	23461 (4·5)		BZ
706 (2)	−1472	9_1^0	433 (3·5)		BZ
604 (5)	−15 4	8_1^0	23358 (6)	−1591	7_1^0
569 (3)	−1609	7_1^0	23229 (10)	−1720	6_1^0
491 (8)	−1687	$6_1^0;36_1^1$	21516 (9)	−3433	6_2^0
465 (9)	−1713	6_1^0	19827 (6)	−5122	6_3^0
20764 (8)	−3414	6_2^0	18161 (3·5)	−6788	6_4^0
19084 (5)	−5094	6_3^0	16519 (1)	−8430	6_5^0
17457 (3)	−6721	6_4^0			

Contd.

Table 1—Wavenumbers and Assignments of the Principal Band Groups in the $\tilde{a}$-$\tilde{X}$ Phosphorescence Emission Spectrum of *o*-,*m*- and *p*-Chlorobenzaldehydes Contd.

Wavenumber* (cm^{-1})	Separation from 0_0^0 band (cm^{-1}) *p*-Chlorobenzaldehyde	Assignment**	Wavenumber* (cm^{-1})	Separation from 0_0^0 band (cm^{-1}) *p*-Chlorobenzaldehyde	Assignment**
25183 (4)		BZ	24210 (0·5)	−856	19_1^0
58 (3)		BZ	24061 (1)	−1005	$18_1^0;26_j^0$
25066 (8)	0	0_0^0	23984 (1)	−1082	17_1^0
42 (7)	−24	25_1^1	60 (1)	−1106	16_1^0
13 (6)	−53	25_2^2	03 (3)	−1163	15_1^0
24986 (6)	−80	36_1^0	23862 (3)	−1204	14_1^0
24894 (4)	−172	25_1^0	23763 (1)	−1303	12_1^0
57 (3)	−209	35_1^0	23695 (2)	−1371	11_1^0
20 (2)	−246	34_1^0	61 (2)	−1405	10_1^0
24742 (0·5)	−324	24_1^0	23591 (2·5)	−1475	9_1^0
06 (1)	−360	23_1^0	23456 (2)		BZ
24662 (0·5)	−404	33_1^0	25 (1·5)		BZ
03 (1)	−463	22_1^0	23342 (10)	−1724	6_1^0
24514 (2)	−552	?	21630 (9)	−3436	6_2^0
24483 (3)	−583	?	19952 (4)	−5114	6_3^0
24372 (0·5)	−694	31_1^0	18293 (2)	−6773	6_4^0

*Values in parentheses represent the relative intensities of bands.

BZ stands for benzaldehyde

**The notation K_i^j stands for a vibronic band which involves *j* quanta of the *K*th vibration in the excited state and *i* quanta of the same vibration in the ground state.

The vibrational intervals of 1273 cm^{-1} (ν_{13}) and 1245 cm^{-1} (ν_{14}) are associated with very sharp bands at 22905 and 22933 cm^{-1} respectively, the corresponding infrared frequencies being 1269 and 1202 cm^{-1} respectively.

The C=O stretching vibration is anharmonic and the first four vibrational intervals determined from the present studies are 1713, 1701, 1680 and 1627 cm^{-1} respectively.

4.2 *m*-Chlorobenzaldehyde

In this case also, the observed bands can be interpreted in terms of only one rotamer as shown in Table 1 for the $T_1 \rightarrow S_0$ emission. We could not detect any band in the region where the torsional vibration is expected to appear. Miller *et al.*[6] have found a band at 105 cm^{-1} in the gas phase far infrared spectrum and this value has been taken to represent the ϕ-CHO torsion.

The lowest ground state fundamental observed in the $S_1 \leftarrow S_0$ absorption spectrum[10] is 162 cm^{-1} in good agreement with the liquid infrared band at 165 cm^{-1} (Ref. 13). There is no band at this interval in the $T_1 \rightarrow S_0$ emission spectrum although from Juyal's measurements[9] there should be one at 0-155 cm^{-1} which is associated with a weak band.

A moderately strong band at 24771 cm^{-1} in the $T_1 \rightarrow S_0$ emission spectrum gives a vibrational frequency of 178 cm^{-1} in good agreement with the infrared value of 181 cm^{-1} (Ref. 13) and a frequency of 179 cm^{-1} observed in the $S_1 \leftarrow S_0$ absorption.[10]

The first four vibrational intervals of the C=O stretch obtained from a strong progression in this vibration are 1720, 1713, 1689 and 1666 cm^{-1} respectively.

4.3 *p*-Chlorobenzaldehyde

The vibronic bands observed in the $T_1 \rightarrow S_0$ emission of this molecule are given with the vibrational assignments in Table 1. The torsional vibration has a frequency of 80 cm^{-1} and is associated with a strong band at 24986 cm^{-1}. This agrees well with the values of 83 cm^{-1} obtained from $S_1 \leftarrow S_0$ absorption[10] and 81·5 cm^{-1} obtained from vapour phase infrared spectrum.[6]

The bands at 24894 and 24857 cm^{-1} involve ground state frequencies of 172 and 209 cm^{-1} respectively. We have assigned the former to a planar vibration and the latter to a non-planar vibration in view of a slightly higher intensity of the former. The vapour phase infrared value of 178 cm^{-1} (Ref. 6) and the $S_1 \leftarrow S_0$ absorption value of 175 cm^{-1} (Ref. 10) are in good agreement with the interval of 172 cm^{-1} obtained from the present work.

The C=O stretching vibration is again found to be anharmonic and the frequencies associated with the first four intervals are 1724, 1712, 1678 and 1659 cm^{-1} respectively.

A study of vibrational spectra of isotopic species of this molecule by Hankin *et al.*[15] reveals close doublets in the regions of 310 and 1700 cm^{-1}. The doublet at 310 cm^{-1} has been interpreted as representi g the out-of-plane C—Cl bending and a coupled mode involving in-plane C—CHO and C—Cl bending. The doublet near 1700 cm^{-1} has been explained in terms of a Fermi resonance. We, however, do not see d oublet structures in these regions on our plates.

5. Results and Discussion

We summarize in Table 2 the vapour phase ground state vibrational frequencies of *o*-, *m*- and *p*-chlorobenzaldehydes obtained from the present study. Some of the vibrational frequencies that could not be observed in the vapour phase electronic spectra have been taken from the electronic absorption of the vapour,[10] liquid phase infrared or Raman spectra[13] or from the vapour phase infrared spectrum,[6] as indicated in the foot-notes of Table 2. In the notations used in Table 2, vibrations 1 to 25 are planar and those from 26 to 36 are non-planar.

It can be seen from Tables 1 and 2 that only two or three out-of-plane vibrations appear in the $T_1 \rightarrow S_0$ emission, and it may be taken as an indication that the molecule does not deviate from planarity significantly in either of the two electronic states.[3,4]

There is a pair of strong bands in each of the three spectra for which we do not find a satisfactory ground state frequency from the infrared or Raman spectra. These bands are at 0-559 and 0-598 cm^{-1} in *o*-chlorobenzaldehyde, at 0-575 and 0-608 cm^{-1} in *m*-chlorobenzaldehyde, and at 0-552 and 0-583 cm^{-1} in *p*-chlorobenzaldehyde spectra. Similar pairs of unexplained intense bands have been observed in the $T_1 \rightarrow S_0$ emissions of benzaldehyde[8] and *o*-, *m*- and *p*-fluorobenzaldehyde[10] also.

The 0_0^0 bands of *o*- and *m*-chlorobenzaldehydes observed in the fluorescence spectra by Juyal[9] coincide with their 0_0^0 bands observed in the absorption spectra.[10] This shows that these electronic bands arise due to only one rotamer. The rotamer which is more stable in the excited singlet state is also expected to be so in the triplet electronic state in view of the results obtained in the cases of *o*- and *m*-fluorobenzaldehydes.[10] The prominent vibronic bands in the spectra of both the molecules have been assigned to the trans-O rotamer on the basis of the arguments presented in the following paragraphs.

5.1 *o*-Chlorobenzaldehyde

(1) The ground state torsional vibration has a frequency of 103 cm^{-1} which agrees well with that of the more stable trans-O rotamer observed in the far infrared spectrum.[6]

(2) In the trans-O rotamer, the C=O stretching frequency in the electronic ground state is expected to decrease from its value in benzaldehyde due to an intramolecular hydrogen bonding as in the case of *o*-fluorobenzaldehyde.[10] The observed value of 1713 cm^{-1} against the corresponding values of 1728 cm^{-1} in benzaldehyde and 1724 cm^{-1} in *p*-chlorobenzaldehyde favours the trans-O conformation.

(3) Due to the hydrogen bonding, as mentioned above, the in-plane bending vibration of the hydrogen atom in the aldehyde group should have a higher frequency than that in benzaldehyde. The observed frequency of 1394 cm^{-1} in *o*-chlorobenzaldehyde against the corresponding frequencies of 1389 cm^{-1} in benzaldehyde and 1383 cm^{-1} in *p*-chlorobenzaldehyde again suggests that it belongs to the trans-O rotamer.

5.2 *m*-Chlorobenzaldehyde

(1) Crowder and Northam[7] interpreted the liquid phase infrared spectrum of *m*-chlorobenzaldehyde in terms of two C=O stretching vibrations at 1696 and 1703 cm^{-1}. On the basis of the variation of intensity with solvent polarity they concluded that the vibrational frequency of 1703 cm^{-1} belongs to the less polar trans-O rotamer. They also reported that the vibrational frequencies obtained for the two rotamers in the gas phase differ by about 20 cm^{-1} (Ref. 7). A value of 1720 cm^{-1} obtained for this vibration in the present investigation corresponds to

Table 2—Ground State Vibrational Frequencies in *o*-, *m*- and *p*-Chlorobenzaldehydes

Vibration (Ref. 13, 14)	Wavenumber (cm^{-1}) *o*-Chloro-benzal-dehyde	*m*-Chloro-benzal-dehyde	*p*-Chloro-benzal-dehyde	Assignment
1	3090*	3085*	3085*	C—H stretch
2	3074*	3064*	3068*	C—H stretch
3		3023*	3048*	C—H stretch
4	3025*		3032*	C—H stretch
5	2871*	2825*	2829*	C—H stretch
6	1713	1720	1724*	C=O stretch
7	1609	1591	1597**	C—C stretch
8	1574	1573*	1576*	C—C stretch
9	1472	1476*	1475	C—C stretch
10	1421	1440*	1405	C—C stretch
11	1394**	1384	1383*	aldehyde C—H bend
12	1295	1305	1303	i.p. C—H bend
13	1273	1267*	1284*	C—C stretch
14	1245	1217	1204	ring—CHO stretch
15	1162*	1160*	1163	i.p. C—H bend
16	1114	1099	1106	i.p. C—H bend
17	1058	1062	1082	
18	1021	998	1005	i. p. C—H bend
19	839	867	856	
20	754**	767	751**	C—Cl stretch
21	637**	644*	626*	
22	445	457	463	
23	413	379	360	
24	337	329	324	i.p. C—Cl bend
25	182	162	175**	i.p. ring—CHO bend
26	1003*	1001*	1014*	aldehyde—H wag
27	978**	939*	967*	o.p. C—H bend
28	954**	916††	949**	o.p. C—H bend
29	862	874***†	824**	o.p. C—H bend
30	776***†	782*	787**	o.p. C—H bend
31	693**	685	694	o.p. ring bend
32	501**	555*	506**	o.p. ring bend
33	401**	426*	404	o.p. ring bend
34	239	242***†	246	o.p. C—Cl bend
35	209	178	209	ϕ-CHO wag
36	103**	105†	80	ϕ-CHO torsion

*Infrared values[13]; **$S_1 \leftarrow S_0$ absorption values[10]; ***$S_1 \rightarrow S_0$ emission values[9]; †Infrared values[6]; and ††Raman values[13]

the higher frequency component of the above pair and has been assigned to the trans-O rotamer as in the case of *m*-fluorobenzaldehyde.[10]

(2) On the basis of their infrared studies, Crowder and Northam[7] assigned a number of vibrational bands to the trans-O rotamer in the mid-infrared region. Two of these frequencies are 1096 and 869 cm^{-1} whereas the corresponding frequencies observed in the present investigation are 1099 and 867 cm^{-1} respectively. This fact also indicates that the trans-O rotamer is the emitter.

This conclusion about the trans-O rotamer of *m*-chlorobenzaldehyde being more stable than the cis-O rotamer is in disagreement with those of Miller *et al.*[6] and Crowder and Northam.[7]

The triplet-singlet emission of *p*-chlorobenzaldehyde is similar to those of benzaldehyde and *p*-fluorobenzaldehyde. The most active vibration arising due to Herzberg-Teller type interaction has been theoretically predicted to be ν_{31} (Ref. 16). This vibration appears weakly in the triplet-singlet emissions of both *p*- and *m*-chlorobenzaldehydes. This observation may be compared with the presence of this vibration in the $T_1 \rightarrow S_0$ emission of *m*-fluorobenzaldehyde[10] and its absence from the corresponding spectrum of *p*-fluorobenzaldehyde.[4]

Acknowledgement

We are thankful to Prof. D K Rai for his interest in this work. One of us (MKH) is thankful to the University Grants Commission, New Delhi, for providing the financial assistance during the investigation and also to the Bhagalpur University, Bhagalpur, for granting him the necessary leave.

References

1. Stockburger M, *Z. phys. Chem.*, **31** (1962), 350.
2. Stockburger M, cited in *Organic molecular photophysics*, Vol. 1-*Fluorescence of aromatic molecular vapours*, edited by J B Birks (Wiley, New York), 1973, 57.
3. Hollas J M & Thakur S N, *Chem. Phys.*, **1** (1973), 385.
4. Haque M K & Thakur S N, *Chem. Phys.*, **32** (1978), 305.

5. Juyal D P & Singh N L, *Curr. Sci.*, **34** (1965), 175.
6. Miller F A, Fateley W G & Witkowski R E, *Spectrochim. Acta*, **23A** (1967), 891.
7. Crowder G A & Northam F, *J. chem. Phys.*, **50** (1969), 4865.
8. Drakenberg T, Jost R & Sommer J M, *J. chem. Soc. Perkin II*, (1975), 1682.
9. Juyal D P, *Spectroscopic studies of organic molecules: Isomeric chlorobenzaldehydes*, Ph D thesis, Banaras Hindu University, Varanasi, 1966.
10. Haque M K, *Electronic spectra of fluoro- and chlorobenzaldehydes*, Ph D thesis, Banaras Hindu University, Varanasi, 1979.
11. McMurry H L, *J. chem. Phys.*, 9 (1941), 241.
12. Vander Donckt E & Vogels C, *Spectrochim. Acta*, **28A** (1972).
13. Green J H S & Harrison D J, *Spectrochim. Acta*, **32A** (1976), 1265.
14. Mulliken R S, *J. chem. Phys.*, 23 (1955), 1997.
15. Hankin S H W, Khalil O S & Goodman L, *J. molec. Spectrosc.*, 72 (1978), 383.
16. Zwarich R & Goodman L, *Chem. Phys. Lett.*, 7 (1970), 609.

Note Added at Proof Stage

The bands followed by question marks in Table 1 may be assigned as sequence bands following the recent work of Koyanagi and Goodman as deurteated benzaldehydes [*J. chem. Phys.*, **39** (1979), 237].

Indian Journal of Pure & Applied Physics
Vol. 18, June 1980, pp. 437-440

A Method of Absolute Spectroscopic Analysis Using X-ray Fluorescence Technique

T V KRISHNAN
R & D Centre, Indian Oil Corporation Ltd, Sector 13, Faridabad 121 002

Received 17 *May* 1979; *revised received* 1 *September* 1979

X-ray fluorescence analysis, like any other spectroscopic method, is normally performed by comparing samples with reference standards. Without proper matching of samples and standards, matrix effects can cause large errors in analysis. It is shown that in a new method developed not only matrix corrections can be taken care of and comparative analysis possible, but even absolute analysis can be performed using X-ray fluorescence technique in the higer concentration ranges. Any single set of standards can be checked for purity or even samples analyzed without reference standards using only the sample and two of its dilutions. The unknown concentration is solved from a quadratic equation obtained from three equations relating normalized intensities and known dilution factors (or concentration ratios) only, irrespective of the matrix of the sample or any of its dilutions.

1. Introduction

Spectroscopic analysis is usually taken as a comparative method. No matter what technique is used for excitation and detection, the intensities of spectral lines from the sample are compared with those from known standards. One of the problems that often confront a laboratory is to check the purity of a set of standards. It is attempted to solve this problem by a method of 'absolute analysis', i.e. analysis without reference to another set of standards and without assuming any single set of data as the accurate one. This is now possible at least for the high concentration ranges by using X-ray fluorescence technique. This method is useful even for cases when standards are not available.

2. Difficulties of Using XRF as an Absolute Method of Analysis

Even when good standards are available in a particular matrix, accurate determination of concentration of an element from observed intensities is difficult especially when the sample is totally unknown. Conversion of intensities measured with standards in one matrix into intensities in another matrix, correction for enhancement and suppression, particle size effect, quantity and similar problems by the method of normalization have been discussed in earlier papers.[1,2]

It has also been shown that the normalized intensities can be related to values of concentration by three relations depending on the working condition and the range of concentrations.[3] After the application of blank correction to the normalized intensities, if I_N is the intensity normalized to any particular matrix and C the concentration of the analyte, the relations between I_N and C can be broadly divided into three regions as follows:

(1) I_N is proportional to C for low concentration ranges;

(2) $\log I_N$ is proportional to $\log C$ for still higher ranges; and

(3) $\log I_N = a \log C - b (\log C)^2$ for the high concentration ranges.

The regions overlap and the decision to use the first, the second or the third relation has to be made on the basis of the type of relation that really holds good for that particular range. This also depends on the normalization factor which depends on the matrix to which all the observed intensities are transformed and for a particular matrix, on the working conditions such as voltage and current. If the normalized counts are increased by the working conditions, by using a light matrix or normalizing to a light matrix, the regions will be shifted and nonlinearity of intensity with concentration will be obtained faster. Similarly, by decreasing the normalized intensity for the same concentration, the constants a and b in relation (3) will be altered and linear relations obtained for high ranges of concentration.

As one obtains totally different intensities without normalization even for the same concentration range, any attempt to obtain a relation between intensity and concentration when widely different matrices are used can be successful only if one can apply the matrix corrections accurately. Two examples are given in Table 1 where the concentration of Ni and Co is the same, viz. 0·5 g of sulphates in both, but 3·5 g of potassium dichromate and 0·5 g of

ammonium ferrous sulphate were taken in sample-1 whereas in sample-2, 3·5 g of ammonium ferrous sulphate and 0·5 g of potassium dichromate were taken. It is noted from Table 1 that the observed intensities of Ni and Co K_α lines vary very widely for the two samples though their concentrations are the same in both the samples. However, when intensities of these lines obtained from sample-2 are normalized to the background values of sample-1, the error is very much reduced. These results are given in Table 1.

Even after the first problem of matrix correction is solved, the second problem is the linear working curves used in spectroscopy. It is a paradox that while all efforts are made to obtain a linear relation between concentration and intensity, it is essentially this linearity that makes spectroscopic methods non-absolute, i.e. a method of analysis by comparison with standards. Linear relations between concentration and intensity can be obtained for a set of three values of intensity and their corresponding values of concentrations, C_1, C_2 and C_3. It is also possible to get a linear relation for the same intensities even if there had been systematic errors in the concentration values such that they are $C_1 + \Delta C$, $C_2 + \Delta C$, and $C_3 + \Delta C$ or nC_1, nC_2 and nC_3 where ΔC and n are constants. There is no way of detecting these systematic errors without comparing these samples with 'standards' outside the system and these 'standards' are in turn checked by instruments.* In case a linear relation is obtained in log-log scale, a systematic increase of three values of C (e.g. $C_1 + \Delta C$, $C_2 + \Delta C$ and $C_3 + \Delta C$ as mentioned above) will definitely disturb the linearity, but a change of values to nC_1, nC_2 and nC_3 will keep the slope of the curve the same. Again, their actual values can be determined only by comparison with a standard.

3. Limitations of the Method of Analysis by Comparison

The necessity for evolving a method of absolute analysis is made clear by attempting to solve the following problem, viz. the comparison of three sets of standards, actually having different concentrations but nominally the same. Batch I consists of sample-1, a 900 ppm Conostan lube oil standard for lead in a twenty-element standard; sample-2, a 17·6957% lead standard as a naphthanate in lube oil and sample-3, a 62·3572% lead standard as pure lead nitrate. Let there be two more hypothetical sets with batch II having 4/5 the concentration of batch I and batch III having 5/4 the concentration of batch I. Their normalized intensities obtained by calculation* from the experimental values of batch I are also given in Table 2. If all the three sets claim to have the same nominal concentrations, one can easily notice that the intensities for the three sets are different. For each batch, let the nominal values for samples-1 and 3 be assumed to be correct and the concentration of lead determined in sample-2. Table 2 shows that the expected value is obtained only for batch I, and batches II and III show large errors from the nominal values. This by itself is not sufficient to prove which set is having the correct values for samples-1 and 3. The inability to check the correctness of a set of standards without assuming some set as the correct one is essentially the limitation of the method of analysis by comparison with standards.

*This situation is similar to the one described by Cohen, Crowe and Du Mond in the context of measurement of fundamental constants. Cohen E R, Crowe K M and Du Mond J M, the *Fundamental Constants of Physics*, (Interscience, New York), 1957, p VI-VII.

Table 1—Comparison of Intensities for the Same Concentration in Different Matrices

Analyte line	Observed counts		Error, %	Normalized to matrix of Sample-1		
	Sample-1	Sample-2		Sample-1	Sample-2	Error, %
Co K_α	321296	634516	97·5	321296	316200	1·6
Ni K_α	169122	259827	53·6	169122	180033	6·5

Experimental conditions: Philips 1410 spectrometer with W tube, 30 kV, 20mA, LiF (first order), base 400, window 400 (100%), att. 2

Table 2—X-ray Fluorescence Analysis as a Comparative Method

Batch	Sample No.	Actual conc., ppm	Assumed conc., ppm	Norm. counts	Conc. determined, ppm	Error, %
I	1.	900	900	66467	Std.	—
	2.	176957	176957	3372051	176278	0·38
	3.	623572	623572	4701046	Std.	—
II	1.	720	900	52146	Std.	—
	2.	141566	176957	3107863	190937	35
	3.	498858	623572	4509436	Std.	—
III	1.	1125	900	85258	Std.	—
	2.	221196	176957	3641947	400050	81
	3.	779465	623572	485037	Std.	—

Note: It is assumed that the first standard in every batch is 900 ppm and the third is 623572 ppm lead

4. An Absolute Method by X-ray Fluorescence

In this method, the second degree relation between the logarithm of normalized intensity and logarithm of concentration, which is valid for high concentration ranges is made use of to solve the same problem given in Sec. 3, by an absolute method of analysis, in the sense that analysis is performed without assuming any single set as the correct set of standards and hence without comparison with any standard outside the system. Tertian has extensively used the sample and its dilutions for the determination of the matrix effect and then the concentration of the unknown sample.[4,5] Analysis by a set of linear equations has been tried by Sherman and others.[6]

Using the equations given earlier, if I_1, I_2, I_3 are the normalized intensities obtained for concentration C, n_1C and n_2C respectively then,

$$\log I_1 = a \log C - b (\log C)^2$$
$$\log I_2 = a \log (n_1C) - b (\log n_1C)^2$$
$$\log I_3 = a \log (n_2C) - b (\log n_2C)^2 \quad \ldots(1)$$

In the set of Eq (1), a, b and concentration C are unknown, n_1 and n_2 being known dilution factors (or known ratio of concentrations for checking the accuracy of standards).

Solving these equations, and eliminating a and b one gets

$$(\log C)^2 \{\log n_2 (\log I_1 - \log I_2) - \log n_1 (\log I_1 - \log I_3)\} + (\log C) \{(\log n_2)^2 (\log I_1 - \log I_2) - (\log n_1)^2 (\log I_1 - \log I_3)\} + \{(\log I_1 \log n_1 \log n_2 (\log n_2 - \log n_1)\} = 0 \quad \ldots(2)$$

This equation is of the satndard form:

$$A X^2 + B X + C = 0$$

and hence can be solved as a quadratic equation in $\log C$.

The experimental conditions or the normalization factors should be so adjusted that the maximum intensity of the second degree equation corresponds for a concentration above 10^6 ppm (i.e. 100%), i.e. $\log C_{max} = a/2b > 6$. In such a case, the larger value of the two solutions obtained for the quadratic equation can be rejected as physically not significant.[7]

The problem of comparison of the three batches of samples given in Sec. 3 is now solved without comparison with standards outside the system. Knowing only the intensities and dilution factors, it is seen from Table 3, that the three batches are different. For sample-1, in the first batch, the concentration of the element is calculated to be 908 ppm giving an error of 0·9% from the nominal value. In the second batch, this is found to be 734 ppm (error 1·9%) and in the third batch, the value is exactly 1125 ppm, agreeing with the actual value. Using the known dilution factor, the concentrations of element in sample-2 are 17·8530%, 14·4318% and 22·1196%, respectively in batches I-III whereas the actual values are 17·6957%, 14·1196% and 22·1196%. Thus it is seen that the errors in the evaluation of concentration of lead in sample-2 of batches I-III are 0·9%, 1·9% and 0·0% respectively. It needs to be pointed out that when it was assumed that samples-1 and 2 have concentrations of the element 900 ppm and 62·3572% in each batch, the determination of concentration of the element in sample-2 by the comparative method (Table 2) gave an error of 35% for batch II and 81% for batch III.

The absolute method has been checked using Pb, Ba, Fe, Cu, Ag, Cd and Nd standards. Some of the results are reported in Table 4. The analysis of neodymium oxide was performed by using only the sample and two of its dilutions. The errors range from 0·8% to 25% depending on the purity of the sample, apart from other factors such as the fluctuations in counts due to voltage fluctuations and other experimental errors.

5. Conclusions

This method can be applied to any sample that can be diluted. In the case of standards whose nominal values are known, taking only the ratios of concentrations as correct, their absolute accuracy can be checked even if the standards are in organic, inorganic or metal forms, or as solids or liquids. Thus it can be used as a very handy technique to

Table 3—XRF as an Absolute Method of Analysis

Batch	Sample	Intensity (Normalized)	Conc. determined ppm	Conc. actual ppm	Error (%)
I	1.	66467	908	900	0·9
	2.	3372051	178530	176957	0·9
	3.	4701046	629115	623572	0·9
II	1.	52146	734	720	1·9
	2.	3107863	144318	141566	1·9
	3.	4509436	508558	498858	1·9
III	1.	85258	1125	1125	0·0
	2.	3641947	221196	221196	0·0
	3.	4865037	779465	779465	0·0

Note: The concentration ratios in batches II and III are the same as that in I, viz. 196·6189 and 692·8578

Table 4—Concentrations Determined from Dilution Factors and Intensities by the Absolute Method

Element	Conc. ratio	I_N	C determined (ppm)	C nominal (ppm)	Error %	Matrix
1. Nd	1	109075	7052	9456	25	Oxide in boric acid
	3·4678	285010	23966	32136	,,	-do-
	92·5161	176,5485	639384	857347	,,	Pure oxide
2. Ba	1	29753	818	900	9	Std. in lube oil
	5·5556	181897	4544	5000	,,	-do-
	624·8289	4706548	511110	562346	,,	Barium chloride salt
3. Ba	1	26830	893	900	8	Std. in lube oil
	111·111	2187780	99222	10,0000	,,	Chloride+ boric acid
	624·8289	4315637	557972	56,2346	,,	Chloride
4. Cu	1	74483	1005	900	12	Std. in lube oil
	11·6667	775866	11725	10500	,,	-do-
	282·7511	4491845	284165	254476	,,	Copper sulphate

evaluate the absolute purity of the standards supplied by various sources. The standards need not be in a form fit for dilution.

This method is applicable to concentration ranges in the nonlinear portion of the working curve of log normalized intensity vs log concentration, for concentrations of element from about 1000 ppm to 100%. To check the standards in lower concentration ranges, the absolute method is not directly applicable as shown in Sec. 2. However, using good standards (checked by this method) in higher concentration ranges and the given standards in the lower concentration ranges, the elongated S-shaped Siedel-like curve can be plotted.[8] If there is no discontinuity in the curve for both the sets of standards, this can be taken as a test for the correctness of the standards, though this is not an absolute test in the earlier sense.

At least for the high concentration ranges, X-ray fluorescence spectroscopy can be made use of as an absolute method, by which, independent of other techniques it can perform analysis without reference to standards using only the sample and its dilutions in any convenient matrix. Just as the methods of normalization and check ratios are applicable to other branches of spectroscopy,[2] this method is in principle, applicable to any spectroscopic system where the relation between the intensity and concentration is given by at least a second degree equation.

Acknowledgement

The author is grateful to Dr J S Ahluwalia, Head, Research and Development Centre for his kind encouragement and keen interest in this work, Dr H S Rao, Head, Analytical Division for the facilities provided and Shri P K Goel, Head, Coordination Division for kindly going through the calculations and useful discussions and Prof. R K Asundi and Prof. J Despujols (Reims Univ.) for their valuable comments. Thanks are also due to (Mrs) Rita Ayyar and Shri K V Rao for their assistance.

References

1. Krishnan T V, *Indian J. pure appl. Phys.*, 15 (1977), 345.
2. Krishnan T V, *Indian J. pure appl. Phys.*, 17 (1979), 178.
3. Krishnan T V, *Indian J. pure appl. Phys.*, 15 (1977), 842.
4. Tertian R, *Fluorescence X, Theorie et Pratique de Analyse Des Solutions, Liquides ou Solids Par Une Methods De Double Measure*, These de Doctorat D' Etat, Es Sciences Physiques, University of Paris, 1972.
5. Tertian R, *Advances in X-ray analysis*, (Plenum Press, New York), 12 (1969), 546.
6. Müller R O, *Spectrochemical analysis by X-ray fluorescence* (Plenum Press, New York), Translated by Klaus Keil, 1972, Ch. 16 and 17.
7. Krishnan T V, *Indian J. pure appl. Phys.*, 16 (1978), 616.
8. Krishnan T V, *Intensity measurements in X-ray fluorescence analysis*, Paper presented at Amer. Nucl. Soc. Conf. Atlanta, 3-8 June 1979, *Trans. Am. Nucl. Soc.*, 32 (1979), 212.

Indian Journal of Pure & Applied Physics
Vol. 18, June 1980, pp. 441-448

Acquisition Behaviour of Phase Locked Loops in the Face of Rayleigh & Lognormal Fading Signals

B C Sarkar, A K Bhattacharya, S K Ray & B N Biswas
Radionics Laboratory, Physics Department, Burdwan University, Burdwan 713 104

Received 12 *March* 1979; *revised received* 10 *January* 1980

Acquisition analysis of a phase locked loop (PLL) with Rayleigh and lognormal fading input signals embedded in white Gaussian noise has been reported. A convenient method for evaluating the locking range and locking time of a second order PLL has been developed. A simple but useful technique of solving higher order Fokker-Planck Kolmogorov (FPK) equation has been suggested. Experimental results have been supplemented to support the theoretical predictions.

1. Introduction

The study of acquisition behaviour of a phase locked loop (PLL) receiver is of considerable importance in the age of deep space communication since a PLL is the main building block of the tracking system. In the hitherto available literature,[1] much work can be observed on the acquisition analysis of a PLL in the face of a modulated or unmodulated signal, either noisefree or embedded in additive white Gaussian noise (AWGN), but little work has been done with a fading input signal where the amplitude and the phase part of the signal have been randomly perturbed due to the propagation of the signal through some time-varying medium. Recently, Weber[2] has studied the performance of a first order PLL with fading signal by Fokker-Planck-Kolmogorov (FPK) apparatus but this method becomes mathematically intractable for higher loops. The acquisition characteristics of a second order PLL in the face of Rician type fading signal in an AWGN environment has been reported by us using quasilinear technique of nonlinear analysis.[3] In this paper, the capture capability of a practical second order PLL has been investigated with Rayleigh and lognormal fading input signals.[2]

The main contribution of the paper, besides providing the expressions for locking range and locking time of the PLL in such a situation, is to formulate a simple but useful method of solving higher order FPK equation. The experimental results of locking range of a second order PLL with simulated Rayleigh and lognormal fading input signals are also reported.

2. Channel Characterization and System Equation

The received fading signal for carrier tracking loop can be conveniently written as,

$$s(t) = a(t) \sin [(\omega_i t + \theta_1 + d(t) + \theta(t)] + n(t) \quad \ldots (1)$$

where $d(t)$ stands for Doppler shift and $n(t)$ is the AWGN of variance σ^2, $a(t)$ and $\theta(t)$ are the amplitude and phase parts of the faded signal and their character determines the kind of the fading channel. When the received signal propagates through the helios corona, $a(t)$ and $\theta(t)$ are given by[4]

$$a(t) = \sqrt{\{A + X_s(t)\}^2 + \{X_c(t)\}^2}$$

$$\text{and } \theta(t) = \arctan \frac{X_c(t)}{A + X_s(t)}$$

where A is the specular part of the received signal and $X_s(t)$ and $X_c(t)$ are the inphase and quadrature components of the narrow band fading noise of of variance σ_s^2. For a Rayleigh fading signal, A is almost absent, hence,

$$a(t) = \sqrt{X_s^2(t) + X^2(t)}$$

$$\text{and } \theta(t) = \arctan \frac{X_c(t)}{X_s(t)} \quad \ldots (2)$$

and $a(t)$ obeys the Rayleigh distribution law.

When the propagation medium of the transmitted signal (amplitude A_0) is a Venusian atmosphere, the received signal would be a lognormal one,[5] and

$$a(t) = A_0 e^{\gamma(t)} \quad \ldots (3)$$

$\gamma(t)$ is a random Gaussian process [mean, m_γ; variance, σ_γ^2] so that logarithm of $a(t)$ is a normal process and the phase part $\theta(t)$ is a Gaussian process almost uncorrelated with $a(t)$; $a(t)$ obeys lognormal distribution law. Referring to Fig. 1, if the reference signal of the voltage controlled oscillator (VCO) be assumed to be of the form

$2\cos\{\omega_r t+\hat{\theta}(t)\}$, ω_r being the free running angular frequency of the VCO, the phase equation of the PLL in mixed notation will be [with linear Doppler shift, i.e. $d\ d(t)/dt = 0$],

$$d\psi/dt = \Omega - KF(s)\,[a(t)\sin\psi + N(t)] + d\theta(t)/dt \quad ...(4)$$

where $\Omega = (\omega_t - \omega_r)$ is the open loop frequency error, $F(s)$ the transfer function of the loop filter. K the VCO sensitivity, $N(t)$ the low frequency version of $n(t)$ having same bandwidth and variance and ψ the loop phase error given by,

$$\psi = \Omega t + \theta(t) + \theta_1 + d(t) - \hat{\theta}(t) \quad ...(5)$$

The solution of the loop phase equation [Eq. (4)] is heuristically assumed in the unlocked condition[3] as

$$\psi = \omega t + \alpha(t) + m(t)\sin\omega t + \psi_n(t) + \psi_\theta(t) \quad ...(6)$$

Here ω is the beat angular frequency which gradually diminishes in the pull-in process; $\alpha(t)$ the constant of integration and $m(t)$ the phase modulation index, are slowly-varying functions of time which make locking possible; $\psi_n(t)$ and $\psi_\theta(t)$ are the phase jitter terms due to AWGN and fading phase noise respectively; the complete characterization of $\psi_n(t)$ and $\psi_\theta(t)$ processes is necessary for the solution of the problem. Since we are interested in acquisition properties of the PLL, we start from an unlocked solution and then extend the solution towards the lock-in condition. Substituting Eq. (6) in Eq. (4) and then by harmonic balance we get the following set of equations that determine the loop behaviour in unlocked condition:

$$d\alpha/dt = \Omega - \omega + aKF(0)J_1(m)\cos\psi_n\cos\psi_\theta\sin\alpha \quad ...(7a)$$

$$m\omega = aKF(\omega)\cos\psi_n\cos\psi_\theta\,[J_0(m)\sin(\alpha+\psi_f) + J_2(m)\sin(\alpha-\psi_f)] \quad ...(7b)$$

$$dm/dt = -a\dot{K}F(\omega)\cos\psi_n\cos\psi_\theta\,[J_0(m)\cos(\alpha+\psi_f) - J_2(m)\cos(\alpha-\psi_f)] \quad ...(7c)$$

$$s\psi_n = -aKF(s)J_1(m)\cos\alpha\sin\psi_n\cos\psi_\theta + KF(s)\,n(t) \quad ...(7d)$$

$$s\psi_\theta = -aKF(s)\,J_1(m)\cos\alpha\cos\psi_n\sin\psi_\theta + \dot{\theta}(t) \quad ...(7e)$$

where

$F(s) = F(\omega)\exp(-j\psi_f)$ and $J_n(x)$ is the Bessel function of order n and argument x, s is the Heaviside operator. From the analysis of the first order loop[3] in noise-free situation, we see that the final value of m is either $+1$ or -1 during the process of locking. But when unwanted random disturbances are present with the signal, the final value of m would fluctuate around $+1$ or -1 and hence it would be wise to consider average frequency error instead of instantaneous frequency drift $\left\langle \frac{d\alpha}{dt} \right\rangle$ to study the acquisition behaviour of the system.

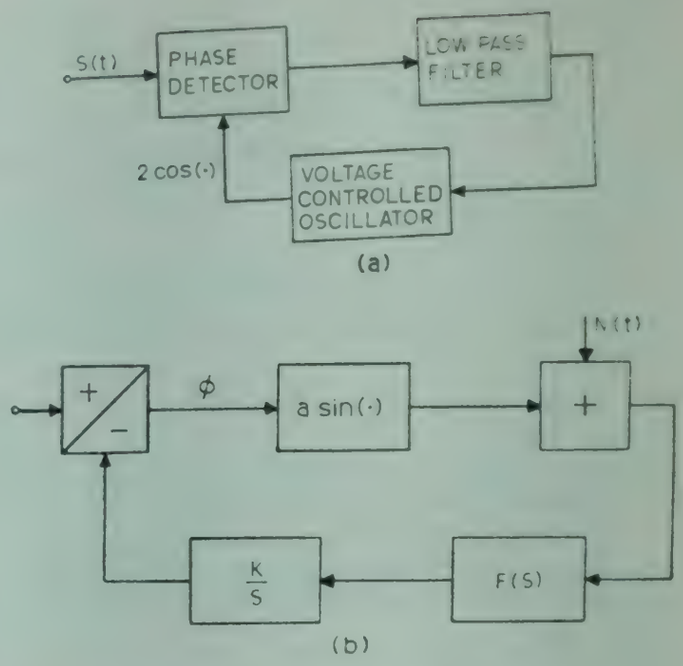

Fig. 1—(a) Block diagram of PLL (b) Equivalent diagram of PLL.

3. System Analysis

The acquisition behaviour of the PLL is now studied with Rayleigh and lognormal fading input signals embedded in AWGN separately. The analytical approach is slightly different in the two cases. For a Rayleigh fading input, the variances of ψ_n and ψ_θ processes are evaluated from the respective probability density functions (pdf) obtained by solving the respective FPK equations of the two processes. A new method of solution of these higher order FPK equations has been suggested in this paper. For a lognormal fading signal, the approach is the same as followed for a Rician fading signal.[3]

3.1 Rayleigh Fading Input Signal

For this case, the system behaviour is described by Eq. (4), where $a(t)$ and $\theta(t)$ are given by Eqs (2a) and (2b). So,

$$\dot{\theta}(t) = \frac{d}{dt}\left[\arctan\left(\frac{X_c}{X_s}\right)\right] = \dot{X}_c\left[\frac{X_s}{X_s^2+X_c^2}\right] - \dot{X}_s\left[\frac{X_c}{X_s^2+X_c^2}\right] \quad ...(8)$$

The joint probability distribution function (pdf) of $a(t)$ and $\dot{\theta}(t)$ is given by,

$$P(a,\dot{\theta}) = \frac{2\pi\sqrt{2\pi\sigma_{\dot{s}}^2}}{(2\pi\sigma_{\dot{s}\sigma})^2} a^2 \exp\left(-\frac{a^2}{2\sigma_{\dot{s}}^2}\right)$$

$$\exp\left(-\frac{a^2\dot{\theta}^2}{2\sigma_{\dot{s}}^2}\right) \quad ...(9)$$

where

$$\sigma_{\dot{s}}^2 = (2\pi)^2 \int_0^\infty 2(f-f_0)^2 S_n(f)\, df \quad ...(10)$$

$\sigma_{\dot{s}}^2$ denotes the variance of fading noise process and $S_n(f)$ is the spectral density of $\dot{\theta}$ process.
In this situation, no simple approximation can be made with regard to the relative magnitudes of any of the terms, $a(t)$ or $\theta(t)$, and therefore, $\dot{\theta}(t)$ process would have to be dealt with in some approximate fashion.

The modelling of $\dot{\theta}(t)$ process can be done in the light of the original work of Rice[6] on the noise output of a FM demodulator. Following the tedious calculations of Rice, the auto-correlation function for the $\dot{\theta}$ process $R_{\dot{\theta}}(\tau)$ and hence the normalized one-sided frequency spectrum of the process $S_{\dot{\theta}}(f)/4\pi B_s$, ($B_s$ being the two-sided bandwidth of fading spectrum) can be obtained.[2] This spectrum can be approximated by a rotational spectrum using low pass first order Butterworth filter representation,[1] given as,

$$G(f) = \frac{C_1}{1 + \left(\frac{f}{B_s C_2}\right)^2} \quad ...(11)$$

where C_1 and C_2 are the constants to be determined on the basis that C_1 equals $S_{\dot{\theta}}(0)/4\pi B_s$ and C_2 can then be obtained by the least square fit principle to the spectrum. Considering the frequency range of the approximating spectrum to be ten times the fading frequency, the values of C_1 and C_2 have been found to be 0·82 and 1·4 respectively. Thus the $\dot{\theta}$ process can be generated by passing a white Gaussian noise process [$u(t)$] of unit power spectral density through a network having transfer function

$$H_1(s) = \frac{(2\pi B_s)^{3/2} C_2 \sqrt{C_1}}{s + 2\pi B_s C_2} \quad ...(12)$$

However, the accuracy can be increased by taking higher order filter transfer function in place of this first order function. To proceed further, we make two assumptions, namely, (i) $a(t)$ and $\theta(t)$ processes are independent of each other, and (ii) $a(t)$ process is taken to be fairly constant throughout a period which is long with respect to the ψ process. Though these assumptions make the analysis a bit restricted, for all practical purposes $a(t)$ can be considered as a constant over the loop operating region since the PLL fails to remain in synchronism when the fading noise bandwidth exceeds the loop band. For a fixed amplitude a, conditional locking range would be obtained and then it would be averaged with respect to the pdf of the incoming signal amplitude to get the average locking range. Then considering

$$\left.\begin{array}{l}\dot{\theta}(t) = H_1(s)\, u(t) \\ \text{and} \quad a(t) \simeq \text{constant}\end{array}\right\} \quad ...(13)$$

and with the method of quasilinearization by replacing the nonlinear terms $\cos\psi_n$ and $\cos\psi_\theta$ in Eq. (7) by $\exp(-\sigma_n^2/2)$ and $\exp(-\sigma_\theta^2/2)$ respectively, the average drift in frequency on the verge of synchronization is given by

$$\left\langle \frac{d\alpha}{dt} \right\rangle = \Omega - 0{\cdot}8\, a\, K \exp\left(-\frac{\sigma_n^2 + \sigma_\theta^2}{2}\right) \overline{F(\Omega)}$$

$$-0{\cdot}2aK \exp\left(-\frac{\sigma_n^2 + \sigma_\theta^2}{2}\right) \sin\alpha \quad ...(14)$$

where

$$\overline{F(\Omega)} = \frac{1}{\Omega}\int_0^\Omega F(w)\, dw \quad ..(15)$$

In Eq. (14), σ_n^2 and σ_θ^2 are the variances of ψ_n and ψ_θ processes which are to be obtained from Eqs. (7d) and (7e) respectively in conjunction with Eq. (13) with the aid of FPK apparatus. Incidentally, it may be noted that it is almost impossible to have an exact closed form solution of a generalized higher order FPK equation in this situation. However, Lindsey[1] has developed an approximate method for the determination of pdf of phase error by computer simulation result. We have developed another approximate method to get $p(\psi_n \mid \psi_\theta, a)$ and $p(\psi_\theta \mid \psi_n, a)$ from higher order FPK equations and found that this simple method would lead to exactly the same forms of solutions for the pdfs of loop phase error processes for Viterbi and Tikhonov filter net works.[7,8] In this method, we first linearize the system Eqs. (7d) and (7e) to have n-dimensional linearized FPK equations, the solutions of which can easily be obtained. The linear terms in the final results would be replaced by their respective nonlinear analogues in a bid to maintain the generality. Thus the total loop variance would be given by,

$$\sigma_\psi^2 = \sigma_n^2 + \sigma_\theta^2 = \int_{-\pi}^{\pi} \psi_n^2\, p(\psi_n \mid a)\, d\psi_n$$

$$+ \int_{-\pi}^{\pi} \psi_\theta^2\, p(\psi_\theta \mid a)\, \psi_\theta\, d \quad .. (16)$$

where $p(\psi_n \mid a)$ denotes the pdf $\psi_n(t)$ process on the condition that $\psi_\theta(t)$ and a are constant and $p(\psi_\theta \mid a)$ is the same for the $\psi_\theta(t)$ process when $\psi_n(t)$

and a are kept constant. With this value of σ_ψ^2 at a particular instant the conditional locking range can be determined from Eq. (14) as,

$$\Omega = aK \exp(-\sigma_\psi^2/2)\ \overline{F(\Omega)} \qquad ...(17)$$

with $\left\langle \frac{d\alpha}{dt} \right\rangle = 0$

and $\alpha_{final} = \sin^{-1}\left[\frac{\Omega}{aK \exp(-\sigma_\psi^2/2)} \right]$

Hence the average locking range in face of Rayleigh fading signal can be achieved by performing the integration of the instantaneous ranges over all possible values of a, i.e.

$$\left\langle \Omega \right\rangle = \int_0^\infty \Omega\ p(a)\ da \qquad ...(18)$$

where $p(a)$ is the Rayleigh density function.

The first basic assumption, viz. considering $a(t)$ and $\dot{\theta}(t)$ as independent, affects the accuracy of the final result. Due to this assumption, both $a(t)$ and $\dot{\theta}(t)$ may increase or decrease at the same instant and thus lessen the effect of $\dot{\theta}(t)$ process; this results in larger magnitude of the calculated locking range. But the independence of $a(t)$ and $\dot{\theta}(t)$ is not the actual case [refer Eq. (9)]. Therefore, the actual average locking range would have smaller values. The process of approximating $\dot{\theta}(t)$ process also affects the accuracy of the final result.

3.2 Lognormal Fading Input Signal

For this case the system governing equation is Eq. (4) with $a(t)$ given by Eq. (3) and $\theta(t)$ is a completely uncorrelated Gaussian process of narrow bandwidth compared with that of the additive Gaussian process. In this situation, we would analyze the system behaviour in different conditions depending on the bandwidths of $a(t)$ and $\theta(t)$ processes. Consider the bandwidths of $\gamma(t)$ and $\theta(t)$ as small compared with the loop bandwidths so that $a(t)$ and $\theta(t)$ are slowly-varying processes. In the slow-fading condition, $\theta(t)$ process is considered to be so slow compared with $a(t)$ that $\dot{\theta}(t)$ is taken to be equal to zero and so loop phase jitter $\psi_\theta(t)$ is zero. Thus, in this condition, applying the method of quasilinearization we can have the instantaneous locking range for a particular amplitude a as

$$\Omega = aK \exp(-\sigma_\psi^2/2)\ \overline{F(\Omega)}, \qquad ...(19)$$

proceeding as in the case of Rayleigh fading signal. The difference is in the expression of loop phase error variance σ_ψ^2 which is only due to AWGN and can be obtained from Eq. (7d) through the solution of FPK equation. The average locking range in this case is

$$\left\langle \Omega \right\rangle = \int_0^\infty \Omega\ p(a)\ da \qquad ...(20)$$

where $p(a)$ is the lognormal distribution function,

$$p(a/A_0) = \frac{A_0}{a} \cdot \frac{1}{2\pi\sigma_\gamma^2} \exp\left[- \frac{\{\ln(a/A_0) - m_\gamma\}^2}{2\sigma_\gamma^2} \right] \qquad ...(21)$$

It may be noted that for conservation of total power $m_\gamma = -\sigma_\gamma^2$.

In the weak amplitude fluctuation condition, we consider $a(t)$ to be nearly constant, i.e. $a(t) \simeq A$ (constant). Only the random perturbation in the phase part is considered where $\theta(t)$ is a narrow band zero-mean Gaussian process. To make the problem tractable, $\theta(t)$ is assumed to be generated by passing a white Gaussian process $V(t)$ of unit spectral density through a first order Butterworth filter of transfer function,[3]

$$H(s) = \frac{w_s b}{s + w_s}$$

where $w_s = 2B_\theta$ and $b^2\ \sigma_s^2/B_\theta$ and
B_θ and σ_s^2 are the fading bandwidth and fading noise power respectively.
Thus,

$$\theta(t) = \frac{w_s\, b}{(s + w_s)}\ V(t) \qquad ...(22)$$

With this model and applying the quasilinearization technique, we can have the expression of average drift in frequency on the verge of locking as

$$\left\langle \frac{d\alpha}{dt} \right\rangle = \Omega - 0{\cdot}8\ AK \exp\left(- \frac{\sigma_n^2 + \sigma_\theta^2}{2} \right) \overline{F(\Omega)} - 0{\cdot}2\ AK \exp\left(- \frac{\sigma_n^2 + \sigma_\theta^2}{2} \right) \sin\alpha \qquad ...(23)$$

where $\overline{F(\Omega)}$ is defined as before and σ_n^2 and σ_θ^2 are the variances of phase error process due to AWGN and fading noise respectively, which can be derived by the spectral analysis method from Eqs. (7d) and (7e) with the help of Eq. (22). Then the locking range (Ω) and locking time (T_L) are respectively given as,

$$\Omega = AK \exp(-\sigma_\psi^2/2)\ \overline{F(\Omega)} \qquad ...(24a)$$

and $T_L =$

$$\int_{\alpha_i}^{\alpha_f} d\alpha / \{\Omega - 0{\cdot}8\ AK \exp(-\sigma_\psi^2/2) - 0{\cdot}2\ AK \times \exp(-\sigma_\psi^2/2) \sin\alpha\} \qquad ...(24b)$$

where $\alpha_i = \pi/2 - \psi_f(\Omega)$

$$\text{and } \alpha_f = \arcsin \frac{\Omega}{A\,K \exp(-\sigma_\psi^2/2)\,F(0)} \quad ...(25)$$

We can consider another situation where the bandwidth (B_γ) of $\gamma(t)$ process is large compared with the loop band of the PLL (B_L) but the bandwidth of $\theta(t)$ process (B_θ) assumes any value. This is the case of fast fading where the loop will see only the average value of the incoming signal amplitude given as,

$$E(a) = A_0 \exp(-\sigma_\gamma^2/2) \quad ...(26)$$

Hence we can get the expression of locking range and locking time from Eq. (24) by replacing A by $E(a)$. This shows that the increase of variance of amplitude fluctuating process would reduce the effective signal strength and hence the locking range accordingly.

4. Examples with Fading Signals

We shall now consider a proportional plus integral type filter incorporated in the loop and find the expressions of locking range and locking time for the Rayleigh and lognormal fading signals using the method suggested by us. The filter transfer function is,

$$F(s) = \frac{1 + F_0\,sT}{1+sT} \quad ...(27)$$

$$\text{whence, } F(w) = \sqrt{\frac{1+F_0^2\,w^2T^2}{1+w^2\,T^2}} \text{ and}$$

$$\psi_f = \arctan \frac{(1-F_0)\,wT}{1+F_0\,w^2T^2} \quad ...(28)$$

4.1 Rayleigh Fading Signal

With Eq. (27), the phase governing Eqs. (7d) and (7e) for ψ_n and ψ_θ reduce to

$$\ddot{\psi}_n + [1/T + \tfrac{1}{2}\,aKF_0 \cos\psi_\theta \cos\psi_n]\,\dot{\psi}_n + \tfrac{1}{2}(aK/T) \cos\psi_\theta \sin\psi_n = (K/T)(1 + F_0T\,d/dt)\,N(t) \quad (29a)$$

$$\text{and } \ddot{\psi}_\theta + [1/T + \tfrac{1}{2}\,aKF_0 \cos\psi_n \cos\psi_\theta]\,\dot{\psi}_\theta + \tfrac{1}{2}(aK/T) \cos\psi_n \sin\psi_\theta = (1/T + d/dt)\,H_1(s)\,u(t). \quad (29b)$$

The linearized versions of these equations are

$$\ddot{\psi}_n + [1/T + \tfrac{1}{2}\,aKF_0]\,\dot{\psi}_n + \tfrac{1}{2}(aK/T)\,\psi = n'(t) \quad ...(30a)$$

$$\text{and } \ddot{\psi}_\theta + [1/T + \tfrac{1}{2}\,aKF_0]\,\dot{\psi}_\theta + \tfrac{1}{2}(aK/T)\,\psi_\theta = \theta'(t) \quad ...(30b)$$

where $n'(t)$ $\left[= \dfrac{K}{T}\left(1 + F_0\,T\dfrac{d}{dt}\right) N(t) \right]$ and $\theta'(t)$ $\left[= \left(\dfrac{1}{T} + \dfrac{d}{dt}\right) H_1(s)\,u(t) \right]$ are the new noise processes to be characterized. The autocorrelation function of the process $n'(t)$ is,

$$R_n'(\tau) = \frac{N_0K^2}{2T^2} \int_{-\pi W}^{\pi W} (1+F_0^2\,w^2\,T^2) \cos w\tau\, dw$$

$$= \frac{N_0K^2}{2T^2}\left[(1+F_0^2\,W^2\,T^2)\int_{-\pi W}^{\pi W}\{\cos w\tau\, dw\} + 2F_0^2(T/\tau)^2\left\{2W\cos W\tau - 2\frac{\sin \pi W\tau}{\tau}\right\}\right] \quad ...(31)$$

But the contribution of the last terms to the net result is insignificant, particularly when the input noise band (W) tends to infinity, and hence the correlation function reduces to

$$R_n'(\tau) \simeq \frac{N_0K^2}{2T^2}\,(1+F_0^2\,W^2\,T^2)\,\delta(\tau) \quad ...(32)$$

Thus the $n'(t)$ process is a δ-correlated process of two-sided power spectral density $(N_0\,K^2/2T^2)$ $(1+F_0^2\,W^2\,T^2)$. Again the auto-correlation function for $\theta'(t)$ process is given by

$$R_\theta'(\tau) = \frac{1{\cdot}6072}{2\pi}\,(2\pi B_s)^3\left[\delta(\tau) + (1-p^2)\,\frac{1}{pT}\,\pi e^{-p/T}\right] \quad ...(33)$$

where $p = 1{\cdot}4\ (2\pi B_s)$. This derivation assumes the input band to be extended up to infinity and $p.\tau/T > 0$. In Eq. (33) also, the contribution of the second part decreases rapidly in the present situation and so power spectral density of the nearly δ-correlated process $\theta'(t)$ may be approximated to be $1{\cdot}6072/2\pi\ (2\pi B_s)^3$. With these considerations regarding $n'(t)$ and $\theta(t)$ processes, two-dimensional steady state FPK equations for ψ_n and ψ_θ can easily be set up from Eqs. (30a) and (30b) respectively. And the solution for the pdf for ψ_n process can be taken as,

$$p(\dot{\psi}_n, \psi_n) = C \exp\left[-\frac{y}{2x}\,\dot{\psi}_n^2 - \frac{yz}{2x}\,\psi_n^2\right] \quad ...(34)$$

where $x = (N_0K^2/2T^2)(1+F_0^2\,W^2\,T^2)$, $y = 1/T + \tfrac{1}{2}a\,KF_0$ and $z = aK/2T$ and C is the normalizing constant to be determined from the boundary conditions,

$$\int_{-\pi}^{\pi}\int_{-\infty}^{\infty} p(\dot{\psi}_n, \psi_n)\,d\,\dot{\psi}_n\,d\,\psi_n = 1$$

$$\text{and } p(\dot{\psi}_n, \psi_n + 2\pi) = p(\dot{\psi}_n, \psi_n) \quad ...(35)$$

Now replacing ψ_n^2 by the corresponding nonlinear term $2(1-\cos\psi_n)$ in the Ist order approximation in

Eq. (34) and with the boundary conditions (35), the phase error pdf is given as

$$p(\psi_n) = \frac{\exp(\alpha \cos \psi_n)}{2\pi I_0(\alpha)} \quad \ldots(36)$$

where $\alpha = 1/2\,(\mathrm{CNR}) \dfrac{2+F_0\,aKT}{1+F_0^2\,(W/aK)\,(aKT)^2}$

Proceeding similarly with Eq. (30b) and with boundary conditions of the same nature as (35) for ψ_θ process, one can get pdf for ψ_θ process as,

$$p(\psi_\theta) = \frac{\exp(\alpha' \cos \psi_n)}{2\pi I_0(\alpha')} \quad \ldots(37)$$

where $\alpha' = \dfrac{(2+F_0\,aKT)}{1{\cdot}6072\,\pi^2\,\delta^3(aK)^2}$, δ being defined as $(2B_s/aK)$, i.e. the instantaneous fading-to-loop noise bandwidth ratio. It will now be judicious to write α and α' normalized in terms of average amplitude $\bar{a}$, and loop phase error variance σ_ψ^2 can then be obtained from Eqs. (36), (37) and (18). Hence, we can have the locking ratio for an instantaneous a as

$$\frac{\Omega}{aK} = (a/\bar{a}) \exp(-\sigma_\psi^2/2) \quad \overline{F(\Omega)} \quad \ldots(38)$$

from which average locking ratio $\left\langle \Omega/aK \right\rangle$ can be obtained by averaging Eq. (38) over $(a/\bar{a})$ with pdf for $(a/\bar{a})$ in this case as

$$p(a/\bar{a}) = \pi/2\,(a/\bar{a}) \exp[-\pi/4\,(a/\bar{a})^2] \quad \ldots(39)$$

The computed variation of average locking ratio with loop CNR $(2\bar{a}/KN_0)$ is shown in Fig. 2.

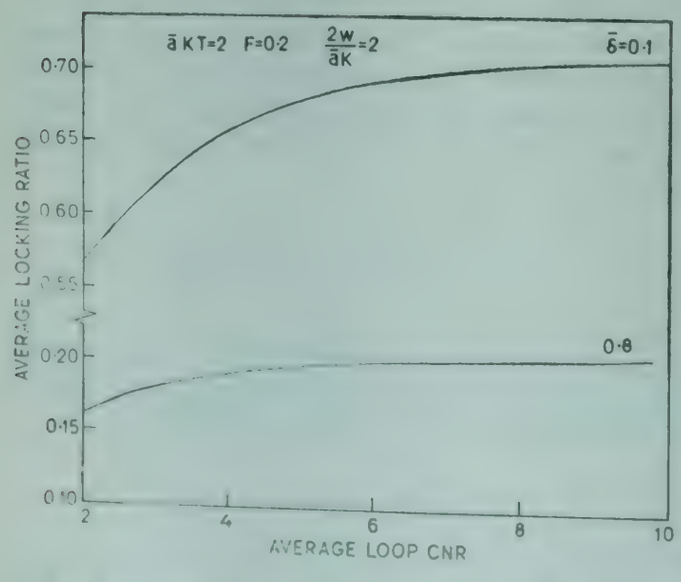

Fig. 2—Variation of average locking ratio with average loop CNR for different values of $\bar{\delta}$ with Rayleigh fading signal

4.2 Lognormal Fading Signal

With this type of fading input signal, the locking characteristics of a PLL incorporating a filter of the form as given by Eq. (27) can be studied by the method outlined in Section 3.2. The computational results for slow fading signal and weak amplitude fading signal are shown in Figs. 3(a) and (b) respectively. For a slow fading signal variation of

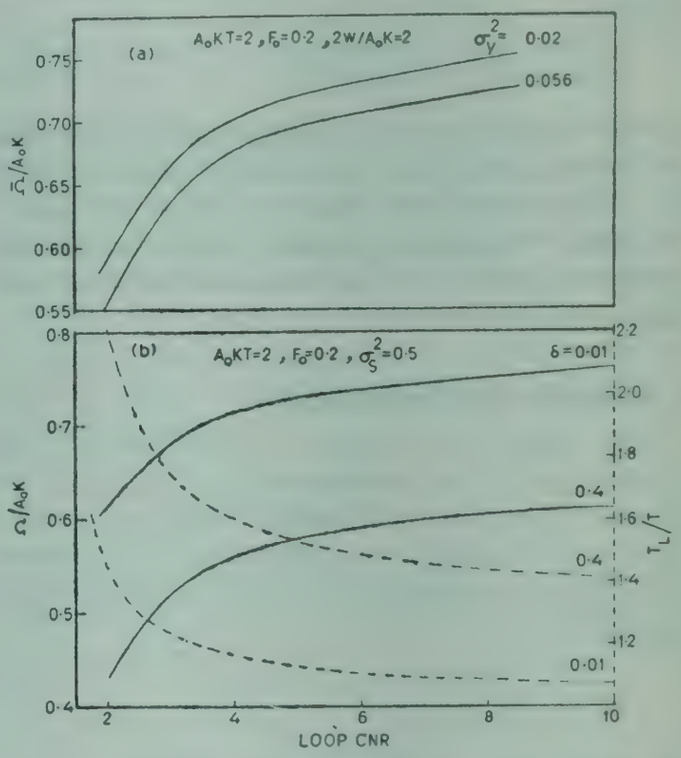

Fig. 3—Computed results for lognormal fading signal [(a) slow fading case : Variation of average locking ratio with average loop CNR for different σ_γ^2; (b) weak amplitude fluctuating case: Variation of locking ratio and normalized locking time with loop CNR for different δ]

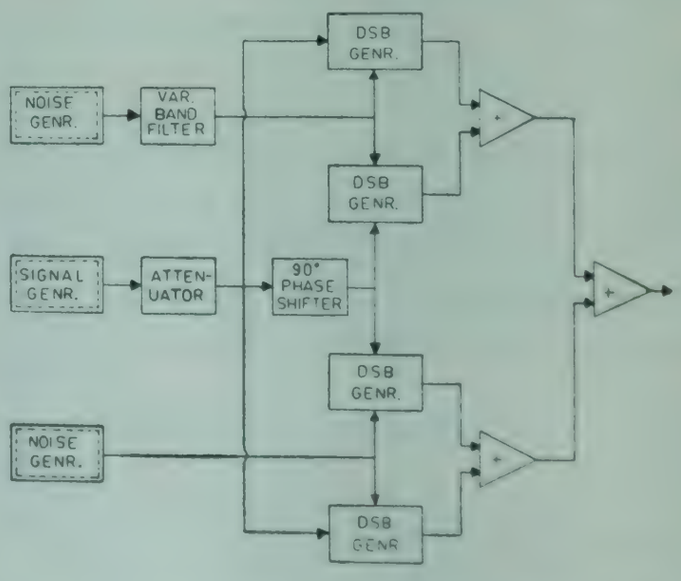

Fig. 4—Block diagram of the experimental set-up for Rayleigh fading channel

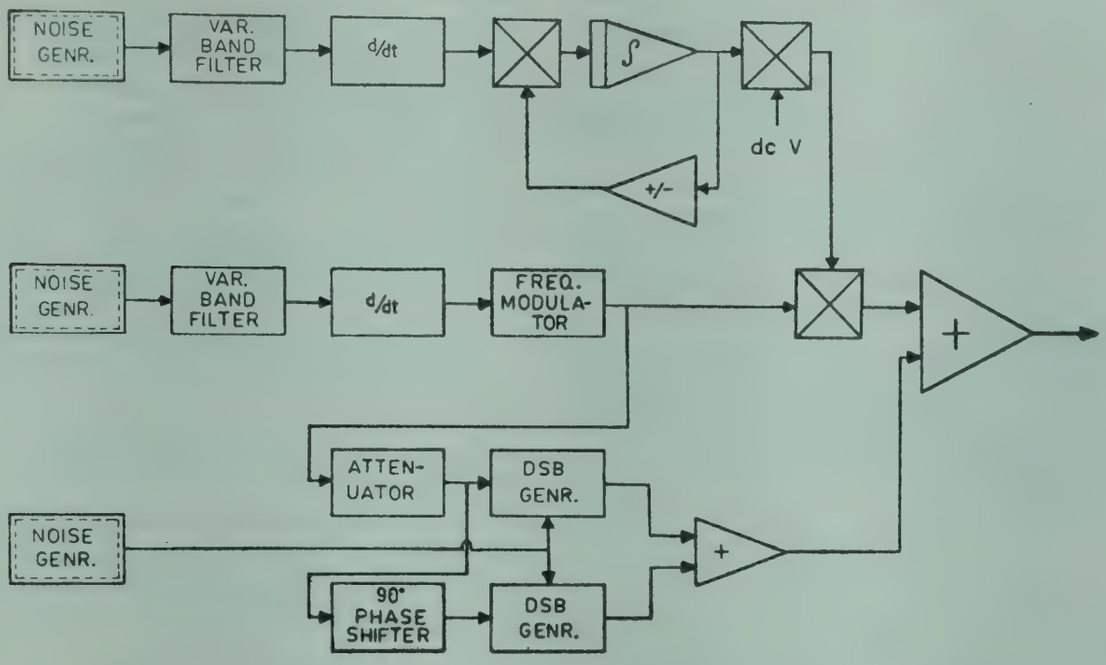

Fig. 5—Block diagram of the experimental set-up for lognormal fading channel

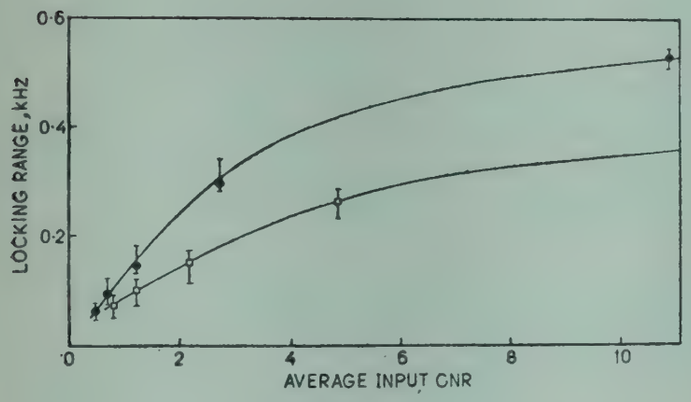

Fig. 6—Variation of locking range with average input CNR in the case of a Rayleigh fading input
[Narrow band noise strengths : □—□, 16·5 mV, and ●—● 22 mV respectively]

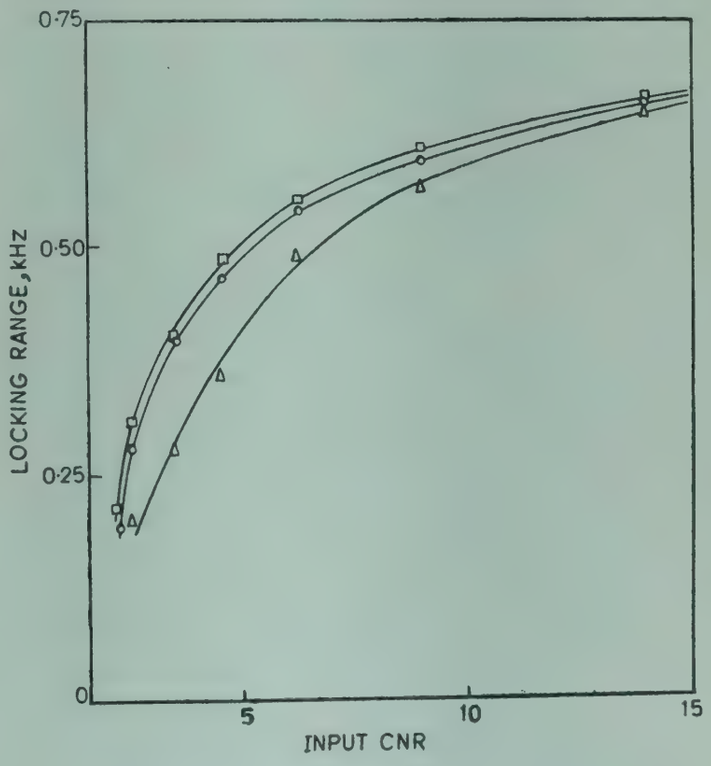

Fig. 7—Variation of locking range with input CNR in the case of a lognormal fading input [The bands of angle and amplitude perturbation processes for different curves are respectively as follows : □—□, 100 Hz and 52 Hz; ○—○, 150 Hz and 62 Hz; and △—△, 250 Hz and 63 Hz]

average locking ratio with loop, CNR is plotted, and for a weak amplitude fading signal variation of locking ratio and normalized locking time with input loop CNR is shown.

5. Experimental Details

The acquisition properties of a second order PLL in the face of Rayleigh and lognormal fading signals have been extensively studied in the laboratory. The fading input signal added with AWGN has been generated by simulating respective channels experimentally. The diagrammatic representation for Rayleigh channel is shown in Fig. 4 and that for lognormal channel in Fig. 5. The experimental observations for the two channels are depicted in Figs. 6 and 7 respectively.

6. Conclusion

The performance degradation of a conventional PLL with fading input signal in terms of its acquisition behaviour has been thoroughly studied for Rayleigh and lognormal types of fading. The effect of fading noise bandwidth and fading noise variance

on the locking range and locking time of PLL has been pointed out. In the course of the study, a simple but approximate approach to solve nonlinear FPK equation has been developed. The loop phase error variance computed from this method is fairly comparable to that derived from other methods, and this is particularly valid when loop CNR is not very low.

Acknowledgement

The investigation was carried out under a research project supported by the Indian Space Research Organization, Department of Space, Government of India.

References

1. Lindsey W C, *Synchronization systems in communication and control* (Prentice Hall, New Jersey), 1972.
2. Weber III W J, *Analysis of phase-locked loops in the presence of time varying communication channels*, Ph D dissertation, University of Southern California, 1974.
3. Biswas B N, Ray S K & Bhattacharya A K, *IEEE Trans. Commun.*, COM27 (1) (1979), 170.
4. Dutcher G L, *A communication channel model of the solar corona and interplanetary medium*, Ph D dissertation, M!T Cambridge, Massachusetts.
5. Woo R, Kendall W, Inshimaru A & Berwin R, *Effects of turbulence in the atmosphere of Venus on pioneer Venus radio—phase I*, Tec nical Memo 33-664, Jet Propulsion Laboratory, Pasadena, Calif, 1973.
6. Rice S O, *Bell Syst. tech. J.*, 27 (1948), 109.
7. Viterbi A J, *Proc. IEEE*, Vol 51 (1963), 1737.
8. Tikhonov V I, *Avtom. Telemekh.*, 22 (9) (1959).

Communications

An Alternative Approach for the Description of Physical Properties in Ferroic Species

P Gopalakrishna Murti & S Uma Devi
Engineering College, Andhra University, Waltair 530 003

Received 10 *December* 1979

A relation between the number of components required to describe a physical property by the ferroic point group, prototypic point group and the species is given. Some of the consequences of this relation are also pointed out.

Aizu[1] defined a ferroic-crystal and its properties on the basis of orientational states and ferroic operations. A ferroic crystal is said to be ferro-magnetic, ferro-electric and ferro-elastic if all or some of whose orientation states are different in spontaneous magnetization, spontaneous polarization and spontaneous strain tensor respectively. Aizu has given the components required to describe the above properties against 164 species for non-magnetic properties.

In this communication, we give a general method of evaluation of the number of components n_i required to describe a physical property for the ferroic species, using Bhagavantam's formula.[2]

$$n_i = 1/g \sum h_\rho \chi'_\rho (R) \overline{\chi}^i_\rho (R) \qquad ...(1)$$

where g is the order of the group and h the order of the ρ th conjugate class. $\chi'_\rho (R)$ is the character of R provided by the appropriate physical property and $\overline{\chi}^i_\rho (R)$ the character of R in the ith irreducible representation.

The occurrence of spontaneous polarization in the lower symmetry is a necessary condition for the crystal to be ferro-electric. So, at least one component of the polarization vector should remain invariant under the symmetry of the ferroic point group (lower symmetry groups). Hence the number of components n_i against the total symmetric representation of H should be $\geqslant 1$, is a necessary condition for the appearance of that property.

But this is not a sufficient condition. The spontaneous polarization should be reversible or reorientable under the influence of an external electric field to exhibit that property. That is, the component occurring against the total symmetric representation of the ferroic point group should make a turn under the symmetry of the prototypic point group. Hence some or all the components vanish under the symmetry of the prototype point group. Thus the number of components against the total symmetric class of the prototypic point group should be less than that of the ferroic point group for a crystal to exhibit that property.

By simple evaluation of n_i from Eq. (1) against the total symmetric representations of both the prototypic and ferroic point group one can say whether a crystal is ferro-electric or not.

The components invarient under the ferroic point group which make a turn on the application of the symmetry elements of the prototypic point group are only responsible for the appearance of the physical property in the ferroic species. Hence the number of components required to describe a physical property by the ferroic species GFH can be evaluated from that of G and H which is given by

$$n_i (GFH) = n_i (H) - n_i (G) \qquad ...(2)$$

If H is a subgroup of index two, then this species is induced by condensation of a soft mode belonging to the corresponding alternative irreducible representation of the prototypic group. Then the number n_i against that representation gives the number of components required by the species against that irreducible representation to describe a property.

But this is not true in case of the other lower symmetry groups, whereas using Eq. (2) we can evaluate the number of components required by all the 773 ferroic species.

The above principle is now illustrated for the three properties namely ferro-electricity, ferro-magnetism and ferro-elasticity for the species 4 *mm Fm* in Table 1.

Table 1—Number of Physical Constants for the Species 4 *mm Fm*

	$n_i (H)$	$n_i (G)$	$n_i (GFH)$
Ferro-electricity	2	1	1
Ferro-magnetism	1	0	1
Ferro-elasticity	4	2	2

Table 2—Components of Magnetic Vector, Polar Vector and Strain Tensor for 48 Ferroic Species

Ferroic species	Ferro-magnetism	Ferro-electricity	Ferro-elasticity
$2/mF1$	2 (M_3)	3 (P_1, P_2, P_3)	2 (x_4, x_5)
$222\ F1$	3 (M_1, M_2, M_3)	3 (P_1, P_2, P_3)	3 (x_4, x_5, x_6)
$mm2\ F1$	3 (M_1, M_2, M_3)	2 (P_1, P_2)	3 (x_4, x_5, x_6)
$mmmF1$	3 (M_1, M_2, M_3)	3 (P_1, P_2, P_3)	3 (x_4, x_5, x_6)
$mmmF\bar{1}$	3 (M_1, M_2, M_3)	0	3 (x_4, x_5, x_6)
$mmmF2$	1 (M_3)	1 (P_3)	1 (x_6)
$mmmFm$	1 (M_3)	2 (P_2, P_3)	1 (x_6)
$4/m\ F1$	2 (M_1, M_2)	3 (P_1, P_2, P_3)	4 (x_4, x_5, x_6, w_6)
$4/m\ F2$	0	1 (P_3)	2 (w_6, x_6)
$422\ F2\ (P)$	1 (M_3)	1 (P_2)	2 (x_6, w_6)
$4\ mm\ F2$	1 (M_3)	0	2 (x_6, w_6)
$\bar{4}\ 2mF2\ (P)$	1 (M_3)	1 (P_3)	2 (x_6, w_6)
$4/mmm\ F1$	3 (M_1, M_2, M_3)	3 (P_1, P_2, P_3)	4 (x_4, x_5, w_6, x_6)
$4/mmm\ F2\ (P)$	1 (M_3)	1 (P_3)	2 (x_6, w_6)
$4/mmm\ F2\ (S)$	1 (M_1)	1 (P_1)	2 (w_6, x_4)
$4/mmm\ Fm\ (S)$	1 (M_1)	2 (P_2, P_3)	2 (x_4, w_6)
$4/mmm\ F2/m\ (P)$	1 (M_3)	0	2 (x_5, w_6)
$4/mmm\ F22\ 2\ (P)$	0	0	1 (w_6)
$4/mmm\ Fmm\ 2\ (P)$	0	1 (P_3)	1 (w_6)
$4/mmm\ F4$	1 (M_3)	1 (P_3)	0
$4/mmm\ F\bar{4}$	1 (M_3)	0	0
$\bar{3}\ m\ F3$	1 (M_3)	1 (P_3)	0
$6/m\ F1$	2 (M_1, M_2)	3 (P_1, P_2, P_3)	4 (x_4, x_5, w_6, x_6)
$6/m\ F3$	0	1 (P_3)	0
$622\ F3$	1 (M_3)	1 (P_3)	0
$6mm\ F3$	1 (M_3)	0	0
$\bar{6}m2\ F3$	1 (M_3)	1 (P_3)	0
$6/mmm\ F1$	3 (M_1, M_2, M_3)	3 (P_1, P_2, P_3)	4 (x_4, x_5, w_6, x_6)
$6/mmm\ F2\ (S)$	1 (M_1)	1 (P_1)	2 (x_4, w_6)
$6/mmm\ Fm\ (S)$	1 (M_1)	2 (P_2, P_3)	2 (x_4, w_6)
$6/mmm\ F3$	1 (M_3)	1 (P_3)	0
$6/mmm\ F\bar{3}$	1 (M_3)	0	0
$6/mmm\ F32$	0	0	0
$6/mmm\ F3m$	0	1 (P_3)	0
$6/mmm\ F6$	1 (M_3)	1 (P_3)	0
$6/mmm\ F\bar{6}$	1 (M_3)	0	0
$m3\ F2$	1 (M_3)	1 (P_3)	4 (x_6, w_4, w_5, w_6)
$432\ F2\ (P)$	1 (M_3)	1 (P_3)	4 (x_6, w_4, w_5, w_6)
$\bar{4}3m\ F2$	1 (M_3)	1 (P_3)	4 (x_6, w_4, w_5, w_6)
$m3m\ F2\ (P)$	1 (M_3)	1 (P_3)	4 (x_6, w_4, w_5, w_6)
$3m3\ F2m\ (P)$	1 (M_3)	0	4 (x_6, w_4, w_5, w_6)
$m3m\ F222\ (SS)$	0	0	3 (x_4, w_4, w_5)

Contd.

Table 2—Components of Megnetic Vector, Polar Vector and Strain Tensor for 48 Ferroic Species (Contd)

Ferroic species	Ferro-magnetism	Ferro-electricity	Ferro-elasticity
m3m F mm2 (PP)	0	1 (P_3)	3 (x_4, w_5, w_6)
m3m Fmm 2 (SS)	0	1 (P_3)	3 (x_4, x_6, w_6)
m3m F 4	1 (M_3)	1 (P_3)	2 (x_6, w_6)
m3m F $\bar{4}$	1 (M_3)	0	2 (x_6, w_6)
m3m F 3	1 (M_3)	1 (P_3)	2 (x_6, w_6)
m3m F 23	1 (M_3)	0	0

$\bar{M} = (M_1, M_2, M_3)$, $\bar{P} = (P_1, P_2, P_3)$, $\bar{X} = (X_1, X_2, X_3, X_4, X_5, X_6)$ denote a magnetic vector, polar vector and strain tensor respectively. And $W_4 = (X_2 - X_3)/2$, $W_5 = (X_3 - X_1)/2$, $W_6 = (X_1 - X_2)/2$, $W_1 = (X_1 - X_1 + X_2 + X_3)/3$, $W_2 = (X_2 - X_1 + X_2 + X_3)/2$ and $W_3 = (X_3 - X_1 + X_2 + X_3)/3$.

In Table 2 the number of components required by the 48 ferroic species which are not generated by a zero wavenumber vibrational mode or a set of degenerate zero number vibrational modes to describe the three above properties are given.

In the case of a non-magnetic property, n_i is the same for a grey group or an ordinary point group or its magnetic variant. If $G\,1'$, G, G' denote a grey group, an ordinary point group and a magnetic variant of the point group G respectively, then n_i ($G\,1'FG$) and $n_i(G1'FG')$ are zero; and $n_i(G1'FH1')$ is as that of n_i (GFH). The above considerations account for all the 212 species considered by Aizu.[3]

In the case of a magnetic property, n_i for a grey group is zero; while n_i for an ordinary point group and its variants can be calculated respectively from the total symmetric and alternative representations of the ordinary point group and when both G and H are grey groups, n_i (GFH) is zero. If G is a grey group and H an ordinary point group or its variant, then $n_i(GFH)$ is the same as $n_i(H)$.

The authors wish to express their grateful thanks to Prof. T S G Krishnamurty, Head of the Department of Applied Mathematics, for his kind interest in this work.

References

1. Aizu Keitsiro, *Phys. Rev. B*, 2 (1970), 754.
2. Bhagavantam S, Crystal symmetry and physical properties (Academic Press, New York), 1966, 83.
3. Aizu Keitsiro, *J. phys. Soc. Japan*, 35 (1973), 180.
4. Landau L D, Lifshitz E M, *Statistical Physics*, Vol. 5. (Pergamon Press, London) 1958, 439.

Notes

Electrical Properties of Bi_2O_3 Layers under Reduced Pressure*

S L Pandey, S Singh & R N Saxena

Thin Films Laboratory, Physics Department
Bareilly College, Bareilly 243 001

Received 12 *March* 1979; *revised received* 12 *September* 1979

Thin film Bi_2O_3 capacitors with Al-electrodes have been prepared by the vacuum evaporation technique. The capacitance decreases with frequency (100 Hz-100 kHz) for all the thicknesses under atmospheric as well as under reduced pressure, the decrease being more pronounced in the former than in the latter. The losses ($\tan\delta$) also vary with frequency, being minimum in the frequency range 1-4 kHz. The capacitors exhibit quite stable capacitance values and moderate losses.

The properties of thin films are highly dependent on the deposition and working conditions. In vacuum-evaporated films, the molecules of residual gases in the vacuum chamber, in howsoever small amounts they may be, cause contamination during condensation of atoms of evaporated material. The dielectric parameters are also affected by the surrounding atmosphere and temperature of the films and connecting lead resistance, etc. The present work was carried out to study the effect of atmosphere on capacitance, loss values ($\tan\delta$) and conduction phenomena in polycrystalline bismuth trioxide (Bi_2O_3) layers.

Doyle[1] reported that Bi_2O_3 decomposes during vacuum evaporation. Molten Bi_2O_3 dissolves nearly all the materials of boats and crucibles in common use.[2,3] Hence the Bi_2O_3 layers were not obtained by the vacuum evaporation of the oxide itself, but by the oxidation of Bi-films on cleaned glass substrates at 175°C in air.

Experimental details—As reported earlier,[4] for preparing Al-Bi_2O_3-Al capacitors, bismuth films with Al-base electrodes were vacuum evaporated on clean, baked glass substrates. These films were then heated at 175°C for several days under atmospheric pressure, till they were completely oxidized into polycrystalline Bi_2O_3. This was confirmed by electron microscopic studies and electrical resistivity measurements of the films. Al-counter electrodes were then deposited in cross-fashion, sandwiching Bi_2O_3 layers in between Al-electrodes.

The thickness of the Bi_2O_3 layers was measured within $\pm$ 50 Å by the Fizeau's method using TOWA metallurgical microscope fitted with a micrometer eyepiece. In the present investigation the thickness of the Bi_2O_3 layer was between 300 and 750 Å.

To measure dielectric parameters, leads were connected to the electrodes of the capacitors. The lead resistance and capacitance were less than 1 Ω and 2 pF respectively.

The study of dielectric parameters was made under atmospheric pressure as well as under reduced pressure (100 micron) at room temperature. The capacitors were mounted on suitable base before taking any observations to avoid damages and disconnections. The variations in capacitance and loss values of stabilized specimen versus frequency (100 Hz-100 kHz) were measured using Marconi Universal Bridge TF 2700 and Philips AC signal generator model PM 5100. For the measurement of current-voltage (I-V) characteristics and breakdown voltage, a circuit reported earlier[4] was used, employing Philips dc μV-meter PP 9004. For taking observations under reduced pressure, the capacitor assembly was kept in an evacuated glass chamber.

Results and discussion—The capacitance (C) decreases with frequency of the applied signal (100 Hz-100 kHz) for all the thicknesses under atmospheric as well as under reduced pressure (Fig. 1), the decrease being more pronounced (max. value of $\Delta C/C$ being $\approx$16%) in the former than in the latter ($\Delta C/C \approx 8\%$). The losses of all the samples also vary with frequency and are minimum in the frequency range 1-4 kHz (Fig. 1) for both the pressure conditions.

The films could bear appreciably stronger fields, before breaking down, under reduced pressure than under atmospheric pressure as shown in I-V characteristics of the samples (Fig. 2).

The breakdown voltage of the thicker dielectric films is higher than those of the thinner ones, but the breakdown field (F_b) decreases with increase in the dielectric thickness (t), obeying a relation $F_b \alpha t^{-\beta}$ as suggested by Forlani and Minnaja[5] (Fig. 3); in the

*Paper presented at the 'Nuclear Physics and Solid State Physics Symposium 1978' organized by the Department of Atomic Energy, Government of India and held at the Indian Institute of Technology, Bombay, during 28-31 December 1978.

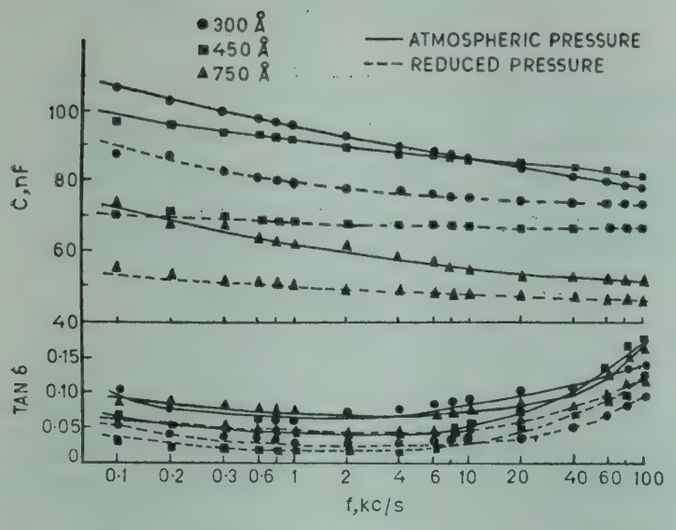

Fig 1—Variations of capacitance and tanδ with frequency under atmospheric and reduced pressures

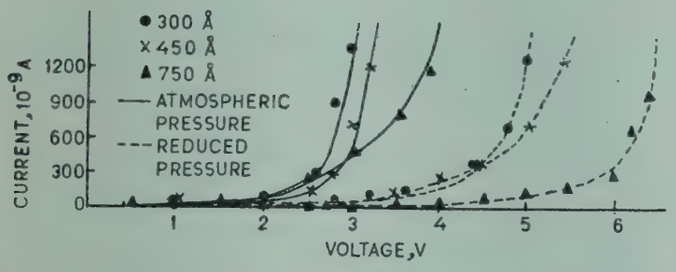

Fig. 2—*I-V* characteristics under atmospheric and reduced pressures

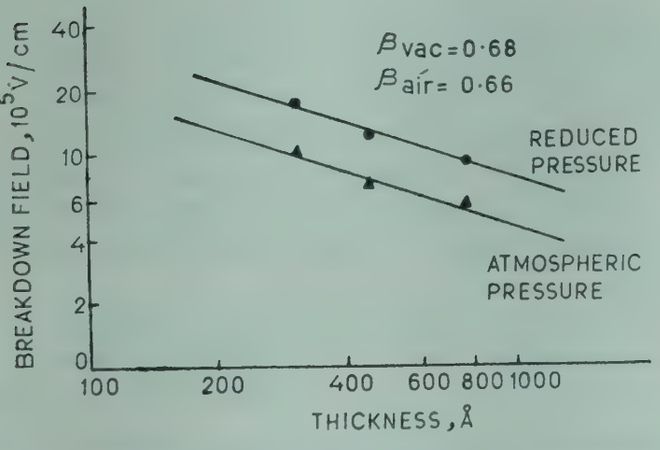

Fig. 3—Breakdown field versus thickness under atmospheric and reduced pressures

present case, β_{air}=0·66 and $\beta_{vac.}$=0·68, where β is a constant. Similar results have been reported by other workers[6,7] for different dielectrics.

The observed variations in capacitance and losses with frequency in the case of Bi_2O_3 layers are quite similar to those obtained for ZnS films.[8]

The measured capacity (C_s) and losses (tan δ) are given by the following relations,

$$C_s = C + \frac{1}{\omega^2 R^2 C} \qquad ...(1)$$

and

$$\tan \delta = \omega r C + \frac{1}{\omega RC} \qquad ...(2)$$

where inherent capacity (C), dielectric resistance (R) (in parallel to C) and series lead resistance (r), are the 3 elements of the capacitor.

The continuous decrease in measured value of capacitance with frequency is evident from Eq. (1).

As is clear from Eq. (2), at lower frequencies, $\tan\delta \propto 1/\omega$ and at higher frequencies, $\tan\delta \propto \omega$, so, on both ends of the frequency range the losses increase, showing a minimum at a frequency $\omega_{min} = \frac{1}{\sqrt{rRC^2}}$. This explains the loss variation with frequency.

The reasons for the capacitance and loss values being more under atmospheric pressure than under reduced pressure may be explained on the assumption that capacitors, when exposed to atmosphere, have two dielectric layers[9]—one of Bi-oxide and the other of adsorbed water vapour. Water vapour decreases the dielectric resistance, resulting in the marked increase in capacitance and loss values.[10] In vacuum, this moisture is extracted out of the dielectric, so C and tanδ are both diminished. Hence for practical uses, the adsorption of moisture should be avoided. The Bi_2O_3 capacitors exhibit quite stable capacitance values and moderate losses. The larger breakdown fields also confirm the extraction of moisture from the dielectric layers. The breakdown field of Bi_2O_3 layers is of the same order as for other dielectrics.

The study reveals that the variation of the signal voltage (0·2 to 2 V), applied for taking measurements, has no effect on the measured values of capacitance and tan δ.

References

1. Doyle W P, *J. Phys. Chem. Solids*, 4 (1958), 144.
2. Halford J H & Hacker (Jr) H, *Thin Solid Films*, 4 (1969), 265.
3. Matton D M & Gildert L, *J. Phys. Chem. Solids*, 18 (1961), 215.
4. Saxena R N *et al.*, *Indian J. Phys.*, 53A (1979), 257.
5. Forlani F & Minnaja N, *Phys. Status. Solidi, A* 4 (1964), 311.
6. Forlani F & Minnaja N, *J. Vac. Sci. Technol.*, 6 (1969), 518.
7. Goswami A P & Goswami A, *Indian J. pure appl. Phys.*, 12 (1974), 26.
8. Goswami A & Goswami A P, *Thin Solid Films*, 16 (1973), 175.
9. Anderson J C, *Dielectrics* (Chapman & Hall, London), 1964.
10. Chopra K L, *Thin film phenomena* (McGraw-Hill, New York), 1969, 475.

Fermi Surface Distortion in Sodium

K N KHANNA

Department of Physics, VSSD College, Kanpur

Received 10 *July* 1978

Radial distortions of Fermi surface in sodium have been studied using a model potential suggested by the author [*Indian J. pure appl. Phys.*, 15 (1977), 733]. The results obtained are comparable with experimental data.

The experimental and theoretical studies have yielded the quantitative information about the anisotropies of the fermi surfaces of the alkali metals. The calculations have shown consistently that fermi surface should be slightly distorted from a free electron sphere and the distortion of the fermi surface should increase in the sequence Na, K, Rb, Cs. Measurements of the de Haas-van Alphen effect in Na were made by Lee[1] and Shoenberg and Stiles[2] studied the effect in K and Rb. The de Haas-van Alphen studies of the fermi surface of Na and K reveal them to be only slightly distorted from free electron spheres.

In addition to experimental studies, the fermi surfaces of alkali metals have been the subject of several theoretical discussions. Ham[3] combined the quantum method with Green's function method to study the band structures of the alkali metals. Heine and Abarenkov[4] found that the computed fermi surfaces were considerably less distorted than those found by Ham.[3] Aschroft[5] analyzed the distortion of the fermi surfaces of K and Rb in terms of a local model pseudopotential. The deviations of the fermi surface from sphericity have also been calculated by Schneider and Stoll[6] for Na, K, Rb, Cs, Al and Pb. Lee and Falicov[7] showed that the shape of fermi surface of K is strongly influenced by low lying *d*-like energy bands. The fermi surface of Na also might be expected to show some residual non-local effects although they are weak due to partial cancellation of the *S*- and *p*-like components of the ionic potential by the *S*- and *p*-like core states.

The electronic band structure is determined by the Secular equation[6]

$$\det \left| \left[\frac{\hbar^2}{2m} (K-h)^2 - E_k \right] \delta_{hh'} + F(h-h') \; U_l(|h-h'|) \right| = 0 \quad .. (1)$$

where $F(h\text{-}h')$ is the structure factor.

The distortion of the fermi surface from a free electron sphere may be written as

$$k_F = K_F^0 \left[1 + \Delta(\theta) \right] \quad ...(2)$$

where θ is the angle between K_F and h and K_F^0 is the free electron fermi wavenumber. Thus $\Delta(\theta)$ is the dilation to the free electron fermi radius K_F^0. From second order perturbation theory, we can write

$$E_F = \frac{\hbar^2}{2m} K_F^{0^2} - \sum_h C(h)\, U_l^2(h)$$

Value of $C(h)$ must be determined by the condition that the distortion should not alter the volume enclosed by the fermi surface. An elementary integration yields :

$$C(h) = \frac{m}{2\hbar^2 K_F^0 h} \ln \left| \frac{2K_F^0 + h}{2K_F^0 - h} \right|$$

The quantity Δ is small and hence higher powers of Δ are neglected. We find

$$\frac{\Delta K_F}{K_F^0} = \sum_{h \text{ pairs}} \left[\frac{U_l^2(h)}{E_F^0} \left(\frac{1}{\frac{\hbar^2}{2m} h^2 - 4E_F^0 \cos^2\theta_{kh}} - C(h) \right) \right] \quad .. (3)$$

which indicates that the deviations from sphericity are simply additive and any number of Bragg-plane pairs can be considered. It is important to note that θ is measured from reciprocal lattice vector h.

In this note, the fermi energy and the radial distortion of the fermi surface of sodium have been calculated using a new model pseudopotential of the form[8]

$$W_b(q) = \frac{2\pi Z e^2}{\Omega q^2} \left[-\cos(qr_c) - \frac{\sin(qr_c)}{qr_c} \right] \exp(-0{\cdot}026\, q^4) \quad .. (4)$$

where Z, Ω, r_c are valence, atomic volume and the radius of ion core respectively. The model potential is screened by the Hartree and modified Hartree dielectric functions, given by

$$\epsilon(q) = 1 + \frac{4\pi Z e^2}{\Omega q^2} \left(1 - f(q) \right) \frac{3}{2E_F} \left[0{\cdot}5 + \frac{4K_F^2 - q^2}{8K_F q} \ln \left| \frac{2K_F + q}{2K_F - q} \right| \right]$$

where $f(q) = q^2/2(q^2 + K_F^2 + K_S^2)$ .. (5)

and

$$\epsilon^*(q) = \epsilon(q) - G(q)\,[\epsilon(q) - 1] \quad .. (6)$$

Table 1—Fermi Energies of Sodium

a	4·225	10^{-8} cm
E_F^0	5·193	10^{-12} erg
E_F (Hartree)	5·060	10^{-12} erg
E_F (Mod. Hartree)	5·053	10^{-12} erg

Table 2—Radial Distortions of the Fermi Surface of Sodium

($\Delta K_F/K_F^0$ in %)

	(100)	(110)	(111)
Hartree dielectric	−0·0538	+0·0632	−0·0110
Modified Hartree dielectric	−0·0588	+0·0692	−0·0120
Experimental values	−0·078	+0·093	−0·015

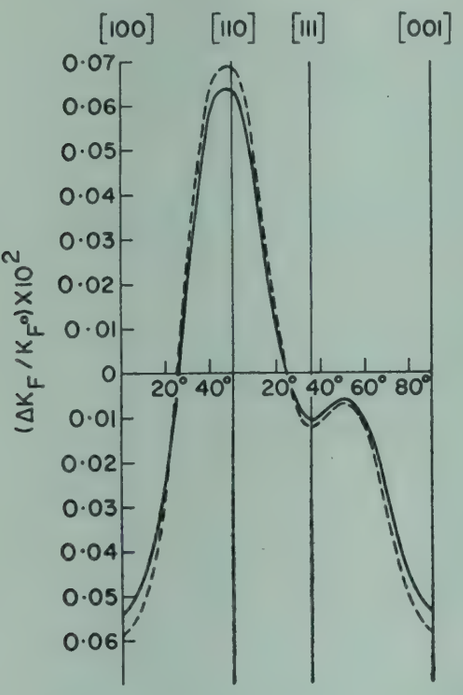

Fig. 1—Distortions of the Fermi surface from sphericity for Na [—Hartree dielectric function ; - - - Modified Hartree dielectric function]

This modified form of dielectric function includes the short-range effects among conduction electrons. The expression for $G(q)$ has been deduced by Singwi *et al.*[9]

Using Eqs. (4) and (5) or (6), the fermi energy and the radial distortion of the fermi surface of sodium are calculated for two dielectric constants. The fermi energies are listed in Table 1 for the equilibrium lattice constant at 0 K. The radial distortions for the (100), (110) and (111) directions are given in Table 2 and the deviations of the fermi surface from sphericity for Na are shown in Fig. 1. In computing Eq. (3), the five nearest neighbour shells are included. We see that the Fermi surface of sodium receives a slight distortion and in agreement with experimental results. We also notice that the radial distortion is more for modified Hartree dielectric function. The experimental results[1] agree more closely with the predictions of the modified Hartree dielectric function than with those of the Hartree dielectric function.

The author is grateful to Dr P K Sharma, Allahabad University and to Dr E Stoll for valuable suggestions.

References

1. Lee M J G, *Proc. R. Soc.*, **A295** (1966), 440.
2. Shoenberg D & Stiles P J, *Proc. R. Soc.*, **A281** (1964), 62.
3. Ham F S, *Phys. Rev.*, **128** (1962), 82, 2524.
4. Heine V & Abarenkov I, *Phil. Mag.*, **9** (1964), 451.
5. Ashcroft N W, *Phys. Rev.*, **A140** (1965), 935.
6. Schneider T & Stoll E, *Phys. Kondens Materie*, **5** (1966), 331, **6** (1967), 135.
7. Lee M J G & Failicov, *Proc. R. Soc.*, **A304** (1968), 319.
8. Khanna K N, *Indian J. pure appl. Phys.*, **15** (1977), 733.
9. Sinawi K S, Tosi M P, Land R H & Sjolander A, *Phys. Rev.*, **176** (1968), 589.

Effect of Magnetic Field on the Current Gain of Junction Transistors

N Manohara Murthy, P Mallikarjuna Reddy* & S V Subrahmanyam

Department of Physics, SVU Post-Graduate Centre
Anantapur 515 003

Received 28 *June* 1979

The effect of magnetic field (B) on the emitter-collector current gain β of junction transistors has been studied. Value of β of transistors made up of germanium was found to decrease on the application of B while no change in B was observed for transistors made up of silicon. The results have been explained on the basis of the theory due to N saleh [*J. appl. Phys.*, 45 (1974), 889].

It is essential to have a knowledge of the effects of intense magnetic field (B) on the operational characteristics of junction transistors when instruments using junction transistors are used in the presence of strong fields. The emitter-collector current gain (β) is one of the most sensitive measures of transistor quality. Misra[1] studied the effect of B on β of 2N654 germanium transistors and observed a decrement of 20 to 25% (in β), when B is equal to 10 kgauss. This decrement in β was attributed by

* Present address : Department of Physics V R College, Nellore.

him as due to the change produced in the characteristics of the base region namely conductivity,[2] lifetime[3] and diffusion constant or mobility.[4,5] Hudson *et al.*[6] studied the effect of B on the operational characteristics of various transistors at 300 K. Parshad and Mehta[7] studied the effect of B on a number of germanium transistors belonging to 2 N and OC series and also on some silicon transistors and found that silicon transistors are less susceptible to B than germanium transistors. The theory proposed by them to explain the effect of B on the characteristics of transistors could not account for the insensitiveness in the characteristics of silicon transistors to B. Saleh[8] proposed a theory to explain the effect of B on β of germanium and silicon transistors and derived the following expressions.

$$\beta(B) = \beta(0) \exp[-B/6{\cdot}76] \qquad \ldots(1)$$

for germanium transistors and

$$\beta(B) = \beta(0) \exp[-B/15{\cdot}4] \qquad \ldots(2)$$

for silicon transistors

where B is in tesla (1 tesla = 10 kgauss) and β (0) represents the current gain at zero field strength. We have studied the effect of B on β of a few series of germanium (AC 125, 126, 127, 128 and AC 188) and silicon (BC 107, 108, 109, 147 and BC 157) transistors at laboratory temperature and the results are reported in this note.

The effect of magnetic field was studied by housing the transistors in between the pole pieces of an electromagnet and β was determined by the convertional method. No change in β of silicon transistors on the application of B was observed. But β of germanium transistors was found to change with B. The variation of the percentage of decrement in β with B for the germanium transistors studied is shown in Fig. 1. The percentages of decrement in β when B is equal to 17·3 kgauss for the germanium transistors are given in Table 1 along with the values of β evaluated using the Eq. (1) due to Saleh[8] for comparison. The agreement between the experimental and theoretical β values is reasonable within the limits of experimental error. The data also indicate that the magnitude of the effect of B on β is not the same for all the transistors. This behaviour suggests that the effect depends not only on mobility, lifetime, and diffusion length, but also on the impurity content in different regions and other structural parameters like thickness of the base region, junction area and geometry of the transistor on which the transistor gain is dependent. The effect of B on β of the

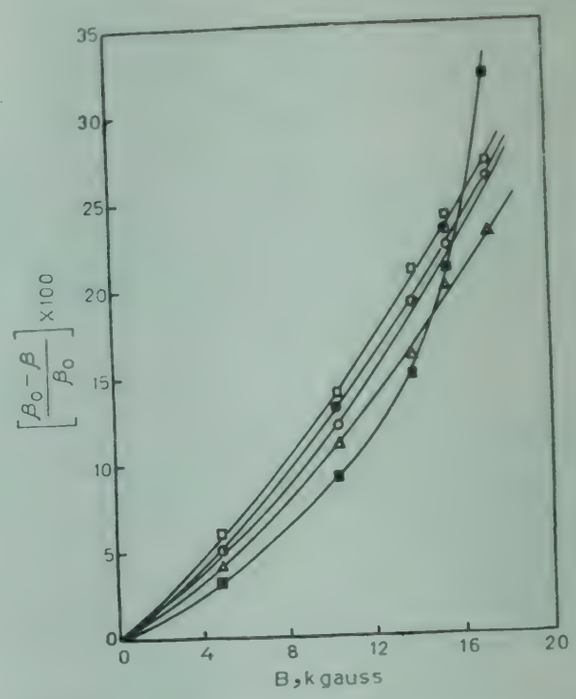

Fig. 1—Variation of the percentage of decrement in β with B for different germanium transistors [Transistor type : □, AC 125; ▣, AC 127; ○, AC 126; ●, AC 128; and △, AC 188]

Table 1—Magnitude of Decrease in β for B = 17·3 kgauss for Various Germanium Transistors at Laboratory Temperature

Transistor type	β			Percentage decrease in β	
	$B = 0$	B = 17·3 kgauss			
		Exptl	Theo	Exptl	Theo
AC 125	127	93	98	27	23
AC 126	133	98	103	26	23
AC 127	81	55	62	32	24
AC 128	142	104	110	27	23
AC 188	250	193	192	23	23

transistors of the same type was found to be not of equal magnitude which may be attributed to the wide production tolerances and technical limitations in the manufacture of these devices.

As per the theory of Saleh,[8] silicon transistors should also exhibit a change in β on the application of B but the present observations showed almost negligible change in β. This behaviour may be considered to be due to the B being small and Eq. (2) indicates that β of silicon transistors will be affected only when $B \sim 7{\cdot}5$ tesla (75 kgauss) which is much larger than the value of B employed in the present study.

References

1. Misra M, *Indian J. pure appl. Phys.*, 3 (1965), 30.
2. Esterman I & Shockley N, *Phys. Rev.*, 79 (1950), 365.
3. Suhl H & Shockley W, *Phys. Rev.*, 79 (1949), 1617.

4. Seitz F, *Phys. Rev.*, 79 (1950), 372.
5. Yefet Y, Keyes R W & Adama E N, *J. Phys. Chem. Solids*, 1 (1956), 137.
6. Hudson W R, Meyh E H & Schultz C W, *IEEE Trans.* MAG-6 (1970), 704.
7. Parshad R & Mehta S C, *Indian J. pure appl. Phys.*, 5 (1967), 165.
8. Saleh N, *J. appl. Phys.*, 45 (1974), 889.

Surface Tension of Hard Sphere Liquids with Attractive Interactions & Estimation of Rao's Acoustical Parameter

B K Sharma

Department of Physics, Regional College of Education
Bhubaneswar 751 007

Received 8 *January* 1979; *revised received* 19 *April* 1979

The validity of an approximate equation of state of real fluids and the expression for surface tension of hard-sphere liquids with attractive interactions [derived by Sharma *et al.*, *Indian J. pure appl. Phys.*, 16 (1978), 1068] have been tested by obtaining the expressions for isothermal compressibility, pressure coefficient of bulk modulus and Rao's acoustical parameter, and comparing them with the experimental values. The agreement is found to be fair in the cases of simple and slightly non-spherical liquids.

Surface tension is one of the important equilibrium properties of liquids and is associated with other molecular thermodynamic and bulk properties. In an earlier paper,[1] analytical expressions for the surface tension and Eötvös constant of liquid systems were derived through radial distribution function (RDF) of a hard sphere with attractive interactions at the point of contact, obtained from the reduced equation of state of real fluids.[2] In the present note, it is proposed to utilize these expressions to derive certain thermodynamic and acoustical properties (related to surface tension) like isothermal compressibility β_T, pressure coefficient of bulk modulus C_1 and Rao's acoustical parameter μ from the pressure coefficient of surface tension and bulk modulus respectively.

The parameter C_1 serving as a severe test for the equation of state of liquids, is defined by[3]

$$C_1 = \left[\frac{\partial (1/\beta_T)}{\partial p} \right]_T \qquad ...(1)$$

where isothermal compressibility is given by

$$\beta_T = - \left(\frac{1}{V} \right) \left(\frac{\partial V}{\partial p} \right)_T \qquad ...(2)$$

The parameter C_1 was introduced[3,4] as a useful tool for investigating the molecular force constants governing the intermolecular energy and other thermodynamic properties of liquid state. C_1 is an important thermodynamic quantity, characteristic of the liquid, even though it has a general value of around 8 for most of the liquids.[5,6]

Rao's acoustical parameter μ is an important acoustical quantity related to C_1. Rao[7,8] found empirically that for a wide variety of unassociated organic liquids near room temperature

$$\mu = - \left(\frac{\partial \ln U}{\partial \ln V} \right)_p = 3, \qquad ...(3)$$

where U is the bulk sound velocity and V the molar volume of the liquid at absolute temperature T and external pressure p.

It was shown[9] that C_1 is related to μ as:

$$\mu = (C_1 - 1)/2 \qquad ...(4)$$

Sharma *et al.*[1] derived an expression for a hard-sphere liquid with attractive interactions in contact with its own vapour of negligible density as

$$Y = A \Big/ \left\{ V \left(V_r^{1/3} - 1 \right) \right\} \qquad ...(5)$$

in which

$$A = - \left(\frac{3}{16} \right) R T (2^{1/2} V^*/N)^{1/3} \qquad ...(6)$$

where V_r $(=V/V^*)$ is the reduced volume, V^* the characteristic or hard core volume, N the Avogadro's number and R the gas constant.

Eq. (6) shows that the surface tension for a rigid sphere fluid with attractive interactions is indeed negative as shown by Kirkwood and Buff[10] and Reiss *et al.*[11,12] Hence we give only the absolute values in the tables.

It was shown, for rigid sphere liquids[13] with attractive interactions, that

$$(\partial Y/\partial p) = (\sigma^*/4) \qquad ...(7)$$

where σ^* is the so called rigid-core molecular diameter.

Recently, Sharma[14] has obtained an analytical expression for thermal expansion coefficient α as

$$\alpha = 3 \left(V_r^{1/3} - 1 \right) \Big/ T \left[1 - 3 \left(V_r^{1/3} - 1 \right) \right] \qquad ...(8)$$

Differentiating Eq. (5) with respect to pressure at constant temperature we obtain

$$\left(\frac{\partial Y}{\partial p} \right)_T = Y \beta_T \left[1 + \left(\frac{\delta}{3} \right) \right] \qquad ...(9)$$

where

$$\delta = V_r^{1/3} \Big/ \left(V_r^{1/3} - 1 \right) \qquad ...(10)$$

Table 1—Comparison of Calculated and Observed Values of β_T

Liquid	T, K	σ^*, Å	V^* cc/mole	V cc/mole	δ	Y dyne/cm	$\beta_T \times 10^{-12}$ cm²/dyne	
							calc	obs
Benzene	293	5·270	67·84	88 86	11·73	29·39	91·4	94·4
Carbon tetrachloride	293	5·881	75·07	96·60	12·52	30·00	94·8	103·4
n-Octane	296	5·400	126·9	163·0	12·61	21·52	120·6	119·8
Cyclohexane	304	6·993	83·47	109·7	11·60	26·15	119·6	122·8
n-Hexane	298	5·909	97·15	131·6	10·50	20·10	163·3	160·6
Acetone	303	4·669	50·70	74·53	8·37	22·60	136·2	138
Methyl acetate	293	4·44	57·91	79·30	10·15	26·62	95·5	101
Ethyl acetate	293	4·80	72·07	97·79	10·44	23·94	111·9	105
Diethyl ether	303	4·74	73·34	105·6	8·82	19·11	157·4	167
Ethyl alcohol	273	4·455	41·63	57·00	10·15	30·96	82·1	96·3
Methyl alcohol	273	3·585	25·96	39·55	7·71	28·00	89·6	106·8
n-Pentane	293	6·099	83·16	115·2	9·81	19·88	179·6	159
Toluene	293	5·932	86·10	106·3	14·90	34·44	72·1	89·4
Nitrous oxide	184	4·59	26·16	36·00	10·00	27·87	95·0	—

A comparison of Eq. (7) with Eq. (9) gives

$$\beta_T = \sigma^* \Big/ \left\{ 4\ Y \left[1 + \left(\frac{\delta}{3} \right) \right] \right\} \qquad ...(11)$$

Eq. (11) establishes a very simple relationship between isothermal compressibility and surface tension. It is very convenient and involves only few parameters. Eq. (11) has been applied for calculating β_T of a few simples, slightly non-spherical and associated liquids. The calculated values are compared with the experimental values in Table 1 taking the necessary data on σ^* and V from literature.[15-17] The calculated values of Y using Eq. (5) and those of V^* were taken from earlier papers.[1,2,14,18] It may be seen from Table 1 that the agreement between the theoretical and the experimental values is fair in case of simple and slightly non-spherical liquids. However, in case of associated liquids the agreement is satisfactory in view of the assumptions and crudeness of the liquid state model in which polar interactions are assumed to be absent. Any deviation in the calculated values of β_T in case of associated liquids is attributed to the effect of strong hydrogen bonding and polar interactions.

Differentiating Eq. (11) with respect to pressure at constant temperature and using Eqs. (6), (10) and (1), we obtain

$$C_1 = 1 + \left(\frac{\delta}{3} \right) \left\{ 1 + \left(4\ Y \beta_T \right) \Big/ \left[3\sigma^* \left(V_r^{1/3} - 1 \right) \right] \right\} \qquad ...(12)$$

Eq. (12) establishes the inter-relationship between C_1 [hence μ vide Eq. (4)], surface tension and compressibility. Knowing the values of Y, β_T, σ^* and V_r, C_1 and μ can be evaluated. However, Eq. (12) takes a simple, convenient form and involves only parameters α and V_r, if various variables Y, β_T and σ^* are eliminated.

Using Eqs. (8) and (11), the simplification of Eqs. (12) and (4) leads to expressions for C_1 and μ respectively as

$$C_1 = 1 + \left(\frac{\delta}{3} \right) \left\{ 1 + \left[1 + \left(\frac{\delta}{3} \right) \right]^{-1} \left[1 + (\alpha T)^{-1} \right] \right\} \qquad ...(13)$$

$$\mu = \left(\frac{\delta}{6} \right) \left\{ 1 + \left[1 + \left(\frac{\delta}{3} \right) \right]^{-1} \left[1 + (\alpha T)^{-1} \right] \right\} \qquad ...(14)$$

Eqs. (13) and (14) are very convenient since C_1 and μ can be estimated from α and V_r only. The calculated values of α using Eq. (8) and C_1 using Eq. (12) or (13) with the literature values[3,4] are presented in Table 2. The values of μ using Eq. (14) are also included in last column of Table 2. It is interesting to note that the calculated values of C_1 show very good agreement with observed values, thereby proving that the equation of state[2] on which the present treatment is based is more realistic. In most cases, the calculated values of C_1 are found to be around 8 in accordance with the suggestion of Gopala

Table 2—Comparison of Calculated and Observed Values of C_1 and μ

Liquid	T, K	δ	$\alpha \times 10^{-3}$ K^{-1}	C_1 calc	C_1 obs	μ
Benzene	293	11·73	1·32	7·77	8·0	3·38
Carbon tetrachloride	293	12·52	1·20	8·27	8·6	3·63
n-Octane	296	12·61	1·17	8·34	8·5	3·67
Cyclohexane	304	11·60	1·30	7·68	—	3·34
n-Hexane	298	10·50	1·54	6·97	7·8	2·99
Acetone	303	8·37	2·26	5·60	6·5	2·30
Methyl acetate	293	10·15	1·66	6·74	8·0	2·87
Ethyl acetate	293	10·44	1·59	6·92	8·0	2·96
Diethyl ether	303	8·82	2·00	5·92	7·5	2·46
Ethyl alcohol	273	10·15	1·78	6·74	5·4	2·87

Rao *et al.*[5,6] Also, the calculated values of μ in most cases are found to lie between 2·5 to 3·5 which is in reasonably good agreement with Rao's relation.

We have given formulae for estimating β_T, C_1 and μ parameters of simple and slightly non-spherical liquids in terms of the values of the reduced volume and α or the parameters σ^*, Y, β_T. The results show that simple liquids can be described satisfactorily by a rigid sphere model with attractive interactions. However, the disagreement in the case of associated liquids having strong polar interactions suggests the inadequacy of the model in explaining the bulk properties of these liquids.

The author thankfully acknowledges the financial assistance from CSIR, New Delhi.

References

1. Sharma B K, Chandrasekhar M A & Kumar S, *Indian J. pure appl. Phys.*, 16 (1978), 1068.
2. Sharma B K & Bhatnagar H L, *Indian J. pure appl. Phys.*, 13 (1975), 328.
3. Moelwyn-Hughes E A, *Physical chemistry* (Pergamon, London), 1965, 330.
4. Moelwyn-Hughes E A, J. *phys. Chem.*, 55 (1951), 1246.
5. Gopala Rao R V, Keer H V & Das C D, *Phys. Chem. Lpz.*, 219 (1962), 321; 220 (1962), 71.
6. Gopala Rao R V, Keer H V & Das C D, *Indian J. Chem.*, 2 (1964), 27, 29.
7. Rao M R, *Indian J. Phys.*, 14 (1940), 109.
8. Rao M R, *J. chem. Phys.*, 9 (1941), 682.
9. Gopala Rao R V & Rao B S M, *Trans. Faraday Soc.*, 62 (1966), 2704.
10. Kirkwood J G & Buff F P, *J. chem. Phys.*, 17 (1949), 338.
11. Reiss H, Frisch H L & Lebowitz J L, *J. chem. Phys.*, 31 (1959), 369.
12. Reiss H, Frisch H L, Helfand F & Lebowitz J L, *J. chem. Phys.*, 32 (1960), 119.
13. Gopala Rao R V, *Indian J. pure appl. Phys.*, 3 (1965), 233.
14. Sharma B K, *Indian J. pure appl. Phys.*, 15 (1977), 633.
15. Gopala Rao R V & Venkata Seshaiah V, *Indian J. Phys.*, 43 (1969), 377.
16. Hirschfelder J O, Curtiss C F & Bird R B, *Molecular theory of gases and liquids*, (John Wiley, New York), 1954, 1110.
17. Timmermans J, *Physico-chemical constants of pure organic compounds* (Elsevier, New York), 1950.
18. Sharma B K, *Indian J. pure appl. Phys.*, 14 (1976), 939.

Transport Properties of Neon, Krypton & Xenon According to L-J (12-6) Potential

P C Jain

National Physical Laboratory, New Delhi 110 012

Received 31 *January* 1979

New values of the distance parameter (σ) of the Lennard-Jones (12-6) potential are derived for neon, krypton and xenon, which enable the transport properties to be described with accuracies comparable to those of the sophisticated potentials.

The Lennard-Jones (12-6) potential has not always been found to be satisfactory in predicting the transport properties of gases. However, in the case of argon, it has been shown[1] that this model can represent the experimental data quite adequately if the distance parameter (σ) is derived from the viscosity values recommended by Maitland and Smith[2] and the energy parameter (ϵ/k) is taken equal to that suggested by Hogervorst.[3] In this note, the same approach has been applied to 3 other noble gases, viz. Ne, Kr and Xe in order to test the suitability of this model for representing their transport properties.

The new σ values thus calculated for Ne, Kr and Xe are given in Table 1 along with their standard deviations. These new values of σ happen to be practically the same as those suggested by Hogervorst.[3]

The transport properties of Ne, Kr and Xe calculated on the basis of these new values of σ taking the same ϵ/k values as suggested by Hogervorst[3] in

Table 1—Potential Parameters of L-J (12-6) Potential for Ne, Kr and Xe

Gas	ϵ/k* K	σ, Å: From Ref. 3	σ, Å: present study	Standard deviation for σ, Å
Ne	43	2·73	2·724	0·008
Kr	193	3·57	3·566	0·006
Xe	256	3·92	3·923	0·006

* Ref. 3

Table 2—Predicted Values of Transport Properties of Ne, Kr and Xe Based on L-J (12-6) Potential as a Function of Temperature

Temp	Thermal conductivity, mW/mK			Viscosity, μg/cm			Self-diffusion coefficient, cm^2/sec		
K	Ne	Kr	Xe	Ne	Kr	Xe	Ne	Kr	Xe
400	60·61	12·35	7·31	390·6	331·3	307·5	0·846	0·173	0·101
600	78·99	17·12	10·40	508·9	458·9	437·3	1·662	0·360	0·215
800	95·17	21·18	13·07	613·0	567·3	548·9	2·678	0·595	0·360
1000	109·93	24·80	15·43	708·2	663·9	647·8	3·875	0·873	0·532
1200	123·69	28·10	17·58	796·8	752·3	737·4	5·241	1·190	0·729
1400	136·65	31·18	19·58	880·2	834·4	821·1	6·764	1·544	0·949
1600	148·97	34·08	21·44	959·7	911·8	899·1	8·436	1·932	1·190
1800	160·73	36·84	23·18	1035·5	985·6	973·6	10·250	2·353	1·452
2000	172·11	39·47	24·89	1108·7	1108·7	1044·9	12·204	2·805	1·734
2200	183·09	42·00	26·49	1179·5	1123·6	1112·4	14·291	3·288	2·034
2400	193·74	44·46	28·05	1248·1	1189·3	1177·9	16·506	3·800	2·353
2500	198·92	45·66	28·81	1281·5	1281·4	1209·9	17·658	4·068	2·519

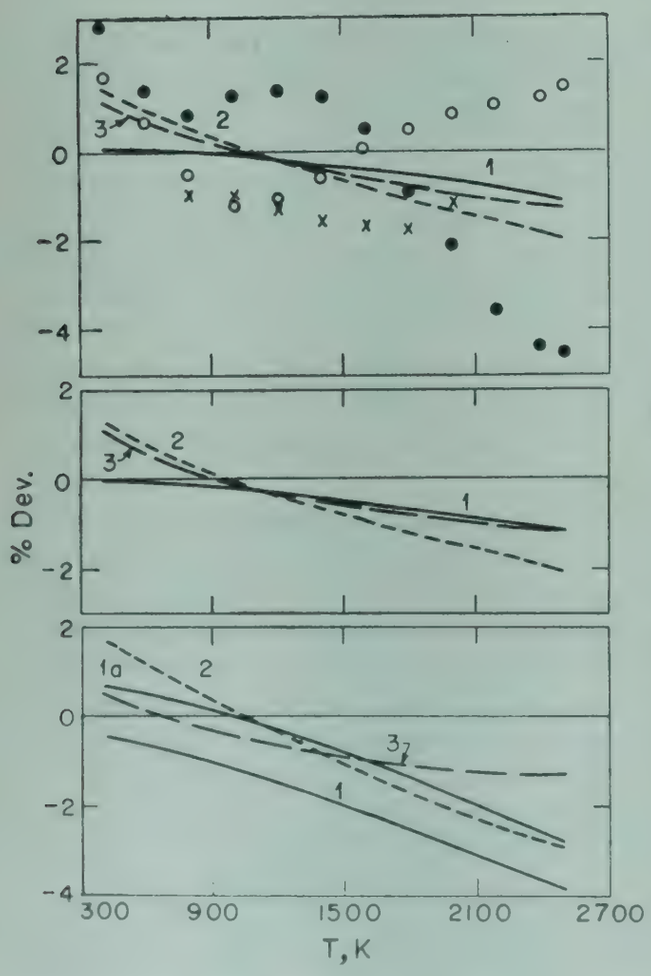

Fig. 1 ←

Fig. 1—Comparison of the thermal conductivity based on the predictions of L-J (12-6) potential with the predictions of sophisticated potential and experimental data [Curve 1, Ne (ESMS VIII)[7]; Curve 2, Kr (BDVKS)[8]; Curve 3, Xe (BWLSLX 3)[10]; ○, data on Ne[11]; ●, data on Kr[12]; × : data on Xe[9]]

Fig. 2 ←

Fig. 2—Comparison of viscosity based on the predictions of L-J (12-6) potential and the sophisticated potentials [Curve 1, Ne (ESMS VIII)[7]; Curve 2, Kr (BDVKS)[8]; Curve 3, Xe (BWLSLX 3)[10]]

Fig. 3 ←

Fig. 3—Comparison of self-diffusion coefficient based L-J (12-6) potential and the sophisticated potentials [Curve 1, Ne (ESMS VIII)[7]; Curve 1a, Ne (ESMS VI)[7]; Curve 2, Kr (BDVKS)[8]; Curve 3, Xe (BWLSLX) 3[10]]

conjunction with the kinetic theory expressions (Hirschfelder *et al.*[4]) are given in Table 2 in the temperature range 400-2500 K. In these calculations, the collision integrals and the higher approximation correction factors suggested by Klein and Smith[5] were used.

Nain *et al.*[6] after reviewing most of the accurate and sophisticated potentials presently available for Ne and Kr have found that the ESMS VIII potential[7] and the BDVKS potential[8] adequately describe the transport properties of Ne and Kr respectively. Similarly, Jody *et al.*[9] have found that

Table 3—Comparison of the Transport Properties of Ne, Kr and Xe Predicted by L-J (12-6) and the Sophisticated Potentials

Transport property	Neon		Krypton		Xenon	
	AAD %	MD %	AAD %	MD %	AAD %	MD %
Thermal conductivity	0·4	1·1	1·0	2·0	0·7	1·3
Viscosity	0·5	1·2	1·1	2·1	0·7	1·2
Self-diffusion coefficient	2·1	3·9	1·5	2·9	0·8	1·3

AAD, average absolute deviation; MD, maximum deviation

Table 4—Comparison of the Predicted Thermal Conductivity Based on L-J (12-6) Potential with the Experimental Data on Neon,[11] Krypton[12] and Xenon[9]

Gas	AAD %	ND %
Ne	0·9	1·7
Kr	2·1	4·5
Xe	1·4	1·8

the BWLSLX 3 potential[10] is superior in the case of Xe.

A comparison of the transport properties of Ne, Kr and Xe predicted on the basis of L-J (12-6) potential (with the parameters recommended in the present work) and the sophisticated potentials—ESMS VIII (Ne), BDVKS (Kr) and BWLSL X 3 (Xe) is displayed in Figs. 1-3 for thermal conductivity, viscosity and self-diffusion coefficient respectively. The agreement in all these cases is very good. The average absolute and the maximum deviations are given in Table 3.

In the case of self-diffusion coefficient of neon, however, the ESMS VI potential[7] leads to better agreement (curve 1a of Fig. 3) [Average absolute deviation (AAD), 1·3 %, Maximum deviation (MD), 2·8%] than the ESMS VIII model.

A comparison of the thermal conductivity predicted on the basis of L-J (12-6) potential with the experimental data of Jain and Saxena[11,12] on Ne and Kr and of Jody *et al.*[9] on Xe is also shown in Fig. 1. The deviations are given in Table 4.

The agreement in the cases of Ne and Xe is excellent. In the case of Kr, however, the agreement is very good up to 2000 K only. The Kr data above 2000 K were also not found to be consistent with the 11-6-8 potential by Nain *et al.*[6]

Thus, the simple L-J (12-6) potential with the suggested parameters (Table 1) is capable of reproducing the transport properties of Ne, Kr and Xe with accuracies comparable to those of the sophisticated potentials.

References

1. Jain P C, *Indian J. pure appl. Phys.*, 16 (1978), 1058.
2. Maitland G C & Smith E B, *J. chem. Engng Data*, 17 (1972), 150.
3. Hogervorst W, *Physica*, 51 (1971), 77.
4. Hirschfelder J O, Curtiss C F & Bird R B, *Molecular theory of gases and liquids* (Wiley, New York) 1964, 528.
5. Klein M & Smith F J, *J. Res. natn. Bur. Stand., Wash.*, 72A (1968), 359.
6. Nain V P S, Aziz R A, Jain P C & Saxena S C, *J. chem. Phys.*, 65 (1976), 3242.
7. Farrar J M, Lee Y T, Goldman V V & Klein M L, *Chem. Phys. Lett.*, 19 (1973), 359.
8. Buck U, Dondi M G, Valbusa U, Klein M L & Scoles G, *Phys. Rev.*, 8A (1973), 2409.
9. Jody B J, Saxena S C, Nain V P S & Aziz R A, *High Temp. Sci.*, 8 (1976), 343.
10. Barker J A, Watts R O, Lee J K, Schafer T P & Lee Y T, *J. chem. Phys.*, 61 (1974), 3081.
11. Jain P C & Saxena S C, *Chem. Phys. Lett.*, 28 (1974), 454.
12. Jain P C & Saxena S C, *J. chem. Phys.*, 63 (1975), 5052.

Calculations of CSDA Range & Projected Range of Monoenergetic Electrons

S K Gupta & D K Gupta

Physics Department, S V College, Aligarh

Received 13 *February* 1979; *revised received* 21 *December* 1979

The continuous slowing down approximation (CSDA) range and projected range of monoenergetic electrons in the energy region 0·2-10·0 MeV for the absorbers of atomic numbers 1 to 92 have been calculated using the empirical relation for the total stopping power of monoenergetic electrons proposed by the authors previously. By applying Bragg's additivity theorem, the calculations were also carried out in some compounds and liquids. The maximum deviation of the calculated values from the reported values is generally around 3-4%.

In two previous papers,[1,2] we have reported an empirical relation for the total stopping power of electrons in the energy region 0·2-10·0 MeV for the absorbers of atomic numbers 1 to 92 as well as for some compounds and liquids, which is expressed as,

$$\left(-\frac{1}{\rho}\frac{dE}{dX}\right)^{-}_{\text{Total}} = (AZ + 1{\cdot}3230)\,\gamma^2/\gamma^{a^- z+b^-} - 1 \quad \ldots(1)$$

where a^-, b^-, and A are the parameters, $\gamma = \frac{T}{m_0 C^2} + 1$, and T is the kinetic energy of incident electrons.

Calculation procedure for CSDA range—In this note, an attempt has been made to calculate CSDA range and projected range. The abbreviation CSDA stands for 'continuous slowing down approximation' defined in Ref. 3. Under this approximation, an electron, when it penetrates into the absorbers,

loses energy continuously by inelastic collisions and the total path length which a particle would travel in the absorbers during the slowing down process in an unbounded homogeneous medium from initial kinetic energy T_0 to final zero kinetic energy is called the CSDA range of the particle. It can be expressed by the relation,

$$R^-(T_0) = \int_{T_l}^{T_0} \left[\left(-\frac{1}{\rho}\frac{dE}{dX} \right)^-_{\text{Total}} \right]^{-1} dT + R(T_l \to 1 \text{ keV}) \quad \ldots(2)$$

where T_l denotes some lower limit below which calculations cannot be performed because of the poor knowledge of total stopping power in that limit (energy region of a few keV). Nelms[4] assumed this limit as 5 keV, whereas Berger and Seltzers[5] took it as 1 keV. We have used the value of 1 keV in our work.

Substituting Eq. (1) into Eq. (2) and integrating, one gets

$$R^-(T_0) = \frac{m_0 C^2}{AZ + 1{\cdot}3230}\left[\frac{\gamma^{a^- z + b^- - 1}}{a^- z + b^- - 1} + \frac{1}{\gamma} \right]_{1{\cdot}1957}^{\gamma_0} + R^-(100 \text{ keV} \to 1 \text{ keV}) \quad \ldots(3)$$

The values of R^- are the same as given by Berger and Seltzer.[5]

It should also be noted that the definition of the CSDA range involves the path length and not the depth of penetration in any special direction. The CSDA range thus differs from other types of ranges such as the projected range and the extrapolated range.

In order to find out the range in compounds and liquids, we have used the procedure of Thompson[6] for the calculation of stopping power of protons through liquids. His calculations were based on the assumption that the stopping power of an atom is unaltered by the proximity of the other atoms or by the atom being bound in a molecule. Thus the stopping power of a compound becomes the sum of the stopping powers of its constituents.

According to the additivity theorem[7,8] the CSDA range of monoenergetic electrons in a compound $A_a B_b$ of molecular weight M is given by,

$$R^-_{\text{cpd}} = \int_0^E \frac{dE}{\frac{aA}{M}\left(-\frac{1}{\rho}\frac{dE}{dX} \right)^-_A + \frac{bB}{M}\left(-\frac{1}{\rho}\frac{dE}{dX} \right)^-_B} \quad \ldots(4)$$

where A and B represent the atomic weight of constituents and a and b the number of atoms per molecule A and B respectively.

While studying the effect of chemical structure of organic compounds on the stopping power of high energy protons, Thompson[6] has proved that Eq. (4) can be approximated to

$$R^-_{\text{cpd}} = M.\frac{R^-_A . R^-_B}{aAR^-_B + bBR^-_A} \quad \ldots(5)$$

where R^-_A and R^-_B are the CSDA ranges.

Calculation procedure for projected range—One can find out the projected range with the help of CSDA range using Tabata's semi-empirical relation,[9]

$$R_{pr} = \frac{1}{2}\lambda\left\{ \left[\left(\frac{4R^-(T_0)}{\lambda} \right) + 1 \right]^{1/2} - 1 \right\} \quad \ldots(6)$$

where λ is the parameter that can be interpreted approximately as the effective transport mean free path, projected on the incident direction of electrons in travelling the whole range and can be expressed in the form

$$\lambda = \left(\frac{\lambda_0}{d_1} \right)\left[1 + d_2 Z^{d_3}\left(\frac{m_0 C^2}{T} \right)^{d_4}\lambda_0 \right]^{-1} \quad \ldots(7)$$

where $m_0 C^2$ is the rest energy of the electrons and d_is ($i = 1$ to 4) are constants.

For the calculation of projected range we have used relation (6); the values of $R(T_0)$ have been calculated with the help of Eq. (3), the values of λ from Eq. (7) and the values of λ_0 from the expression of Bethe *et al.*[10]

Results and discussion—The computation work of the constants a^-, b^- and A was done with the help of IBM-1130 computer and the results are presented in Table 1. Table 2 represents the comparison between the calculated values and reported values of CSDA range[5,11] for four representative cases, viz. aluminium, copper, gold and lead. These metals were chosen arbitrarily keeping in view that they will cover the entire range of metals from $Z = 1$ to $Z = 92$ though the authors have made the calculations for the entire

Table 1—Numerical Values of Constants

Z-Values	$-A$ (MeV cm²/g)	a^-	b^-
$1 \leqslant Z \leqslant 10$	0·05800 ± 0·0148		
$10 \leqslant Z \leqslant 36$	0·02985 ± 0·0132	−0·0040	1·8160
$36 \leqslant Z \leqslant 92$	0·01295 ± 0·0036		

Table 2—Comparison of Theoretical and Calculated Values of CSDA Ranges for Metals

K E (MeV)	Theoretical values g/cm²	Calculated values g/cm²	Difference (%)	Theoretical values g/cm²	Calculated values g/cm²	Difference (%)
	Aluminium			Copper		
0·2	0·05772	0·05556	−3·74	0·06739	0·0639	−5·16
0·5	0·2243	0·2254	−0·51	0·2567	0·2544	−0·87
0·8	0·4168	0·4296	3·07	0·4725	0·4805	1·70
1·0	0·5493	0·5718	4·09	0·6198	0·6365	2·70
3·0	1·855	1·9669	6·03	2·030	2·1240	4·67
5·0	3·076	3·2381	5·27	3·294	3·4329	4·21
8·0	4·777	4·9776	4·20	4·984	5·1768	2·86
10·0	5·841	6·0598	3·74	6·003	6·2408	3·96
	Gold			Lead		
0·2	0·08929	0·0839	−5·97	0·09100	0·0850	−6·55
0·5	0·3248	0·3207	−1·26	0·3303	0·3228	−2·24
0·8	0·5818	0·0839	1·54	0·5906	0·5936	0·50
1·0	0·7529	0·7719	2·52	0·7631	0·7748	1·53
3·0	2·274	2·3559	3·60	2·288	2·3519	2·79
5·0	3·509	3·6077	2·81	3·519	3·5902	2·02
8·0	5·029	5·1434	2·27	5·028	5·1021	1·47
10·0	6·888	6·0257	2·33	5·879	5·9675	1·50

Table 3—Comparison of Theoretical and Calculated Values of CSDA Ranges for Representative Compounds

K E (MeV)	Theoretical values g/cm²	Calculated values g/cm²	Difference (%)	Theoretical values g/cm²	Calculated values g/cm²	Difference (%)
	Stilbene			Methane		
0·2	0·04587	0·0451	−1·67	0·03724	0·0367	−1·26
0·5	0·1811	0·1857	2·56	0·1476	0·1499	1·60
0·8	0·3399	0·3536	4·03	0·2766	0·2844	2·81
1·0	0·4503	0·4713	4·67	0·3657	0·3783	3·45
3·0	1·565	1·6421	4·93	1·248	1·3144	5·32
5·0	2·638	2·7299	3·48	2·078	2·1911	5·44
8·0	4·176	4·2431	1·60	3·247	3·4218	5·38
10·0	5·164	5·1955	0·61	3 990	4·2023	5·32
	Polystyrene			Xylene		
0·2	0·04524	0·0445	−1·55	0·04433	0·0436	−1·66
0·5	0·1786	0·1833	2·63	0·1750	0·1793	2·40
0·8	0·3352	0·3490	4·13	0·3283	0·3410	3·89
1·0	0·4441	0·4649	4·69	0·4349	0·4544	4·49
3·0	1·544	1·6195	4·89	1·511	1·5826	4·73
5·0	2·602	2·6928	3·49	2·547	2·6321	3·34
8·0	4·120	4·1868	1·62	4·034	4·0947	1·50
10·0	5·095	5·1276	0·64	4·989	5·0164	0·56

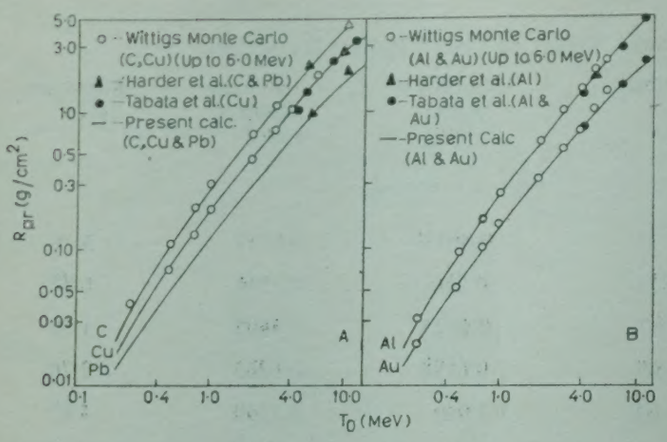
o - Wittigs Monte Carlo (C,Cu) (Up to 6·0 Mev)
▲ - Harder et al.(C & Pb)
● - Tabata et al.(Cu)
— - Present calc. (C,Cu & Pb)
o - Wittigs Monte Carlo (Al & Au) (Up to 6·0 MeV)
▲ - Harder et al.(Al)
● - Tabata et al.(Al & Au)
— - Present Calc (Al & Au)
C
Cu
Pb
Al
Au
A
B
R_{pr} (g/cm²)
T_0 (MeV)

Fig. 1—Projected range R_{pr} as a function of incident energy T_0 (for energies below 10 MeV)

range of metals. Table 3 shows a comparison between the CSDA ranges in four representative compounds, viz. stilbene, methane, polystyrene and xylene. However, calculations were also carried out in ethylene, acetylene, toluene, polyethylene, carbon dioxide, water, anthracene and lucite. It can be seen from these Tables that Eqs. (4) and (5) reproduce very well the CSDA range. A measure of goodness of calculations may be given by the percentage difference of the calculated values from the reported theoretical values.

In Fig. 1 the calculated values of projected range using Eq. (6) have been compared with the available results in the literature from different approaches, in five representative metals, viz. carbon, aluminium, copper, gold and lead, though the authors have calculated projected range (R_{pr}) for the entire range of the metals. Our calculated values of R_{pr}, for the sample metals carbon, aluminium, copper, gold and lead are in good agreement with the calculated values reported by Wittig[12] through Monte Carlo calculations up to 6·0 MeV. It can be seen from Fig. 1 that our results are also in agreement with experimental results obtained by Harder and Poschet[13] from the measurements of transmission curves and by Tabata *et al.*[9] from the measurements of charge deposition distribution. The slope of the curve for each of the metals is also almost similar.

Since the problem of the penetration of electrons through matter is much complicated, drastically simplified approaches are frequently necessary in deriving explicit expressions for quantities of interest. The empirical relation suggested in this note is useful for establishing such simplified treatments as projected range, etc.

It may be concluded from the tables that CSDA range of monoenergetic electrons in various metals and compounds, reported from the approach of Berger and Seltzer[5] is in good agreement with the approach proposed by the authors. The labour involved in the present approach is extremely reduced compared to the numerical methods.

Our empirical relation is also useful in calculating stopping power and range in case of positrons simply by adjusting the values of constants. This study is under progress.

The authors are thankful to Dr S C Gupta, Principal of the S V College for his encouragement during the course of this work. They would also like to thank to Drs Aslam Qadeer, D C Tomar and other staff of the computer centre of the Aligarh Muslim University (AMU) for providing computer facilities, useful discussions and for their kind co-operation. We are also grateful to Prof. M Z R Khan, Head of the Physics Department, AMU for providing library facilities. One of us (SKG) acknowledges the financial assistance from CSIR, New Delhi, in the form of a junior research fellowship.

References

1. Gupta S K & Gupta D K, *Symp.Nucl. Phys. Solid St. Phys. (India)*, (Department of Atomic Energy, Government of India, Bombay 1), **20B** (1977), 172.
2. Gupta S K & Gupta D K, *Indian J. pure appl. Phys*, 17 (1979), 775.
3. Berger M J & Seltzer S M, *Studies in penetration of charged particles through matter*, NRC-Pub. No. 1133, 1964.
4. Nelmes A, *Energy loss and ranges of electrons and positrons*, NBS Circular No. 577, 1956.
5. Berger M J & Seltzer S M, *Tables of energy loss and ranges of electrons and positrons*, NASA-SP-3012, 1964.
6. Thompson T J, *Effect of chemical structure on stopping powers for high energy protons*, Ph D thesis, UCRL-1910, August 1952.
7. Trower W P, *Range-momentum and dP/dX plots of charged particles in matter*, UCRL-2426, Vol. IV, 1966.
8. Aron W A, *The passage of charged particles through matter*, Ph D thesis, UCRL-1325, May 1951.
9. Tabata T, Ito R & Okabe S, *J. appl. Phys.*, 42 (1971), 3361.
10. Bethe H A, Rose M E & Smith L P, *Proc. Am. phil. Soc.*, 78 (1938), 573.
11. Pages L, Bertel E, Joffre H & Saklavenitis L, *Atomic Data*, 4 (1972), 1.
12. Wittig S, *Johann-Wolfgang-Goethe University Institute for Nuclear Physics Report* No. IKF-20, 1968 (unpublished).
13. Harder D & Poschet G, *Physics Lett.*, 24B (1967), 519.

INSTRUCTIONS TO CONTRIBUTORS

Manuscripts should be typewritten in double space and on *only one side* of good quality paper; the original and *one carbon copy are to be submitted.*

Papers must be written in clear and concise English. Good attention to spelling and grammar should be given. Long introductions should be avoided. Standard international nomenclature should be followed in giving names of chemical compounds. Standard abbreviations for units of measurement should be used in the text, tables and illustrations. The abbreviations should be used without fullstops.

Title—The title should be neither too brief/general nor unnecessarily long. It should reflect the content of the paper so as to derive the maximum advantage in indexing and information retrieval. A short title for use as running title should also be supplied. If a paper forms part of a series, a subtitle indicating the aspects of the work covered in the paper should be provided.

Abstract—The abstract should indicate the scope of the work and the principal findings of the paper. It should not exceed 3% of the length of the paper and, barring exceptional cases, it should not exceed 200 words. The abstract should be prepared in such a form that abstracting periodicals can use it without modification.

Data—Only such primary data as are essential for understanding the discussion and the main conclusions emerging from the study should be included. All such secondary data as are of interest to a specific category of readership may, if necessary, be deposited in the editorial office (or retained by the authors) for supply on demand. A footnote to this effect may be inserted at a suitable place in the paper.

Mathematical portions—Special attention should be given to the mathematical portions of the paper. Equations must be well separated from the text and written clearly with good separation between the successive lines. The usual norms of breaking long mathematical expressions may be adhered to. Equations should be numbered consecutively in Arabic numerals with the number in parentheses near the right hand margin. Superscripts and subscripts should be clearly indicated in pencil by $\vee$ and $\wedge$ sign respectively. Capital and small letters, particularly of the same letter when both occur, as well as letters or symbols likely to be confused one for the other, should be clearly distinguished. Special characters (e.g. Greek, script, vector, tensor, matrix, etc.) required must be indicated by marginal notes. Letters and symbols which should appear in bold face must be clearly indicated. To simplify typesetting: (i) long and complicated mathematical expressions which are frequently repeated should be replaced with single letter/symbol, without clashing with the others used in the paper; (ii) the "exp" form of complex exponential functions should be used: and (iii) to simplify fractions, the solidus (/) is to be used and fractional exponents are to be used instead of root signs, e.g.

write $\left(4\omega_{pl} K_{s\lambda}^2 \Big/ \tilde{\omega}\ K_D^2\right)^{1/2}$ and *not* $\sqrt{4\frac{\omega_{pl} K_{s\lambda}^2}{\tilde{\omega}\ K_D^2}}$

write $\exp\{-i\omega_0 (t_1 - t_2)/2\}$ and *not* $e^{-i\omega_0 (t_1-t_2)/2}$

Tables—Tables should be typed *on separate sheets* of paper without any text matter on the page. They should be numbered consecutively in Arabic numerals and should bear brief titles. *Column headings should be brief.* Units of measurements should be abbreviated and placed below the headings. Nil results should be indicated and distinguished clearly from absence of data. Graphs as well as tables, both representing the same set of data, must be strictly avoided. Inclusion of structural formulae inside the tables should be avoided as far as possible. Tables should be referred to in the text by numbers and not by terms like 'above', 'below', 'preceding' or 'following'.

Illustrations—All illustrations should be numbered consecutively in Arabic numerals. Captions and legends to the figures should be self-explanatory and should be typed on a separate sheet of paper and attached at the end of the manuscript. Line drawings should be made with Indian ink on white drawing paper (perferably Bristol board), cellophane sheet or tracing cloth. In addition to the originals, a set of blue-prints or photostat copies should be sent. For satisfactory reproduction, the graphs and line drawings should be drawn to approximately twice the printed size.

The lettering should be uniform, perferably in stencil, so as to be *not less than 2 mm after reduction* widthwise to 3″ or 6″ as required. The size of geometrical shapes (used to distinguish different graphs), dot, lines, etc. should be sufficiently large to permit the necessary reduction without loss of detail. In the case of *photographs*, prints *must be on glossy paper and contrasty.* If an illustration is taken from another publication, reference to the source should be given and prior permission secured. Illustrations should be protected by thick cardboard packing against creases, folds and broken corners during transit. Illustrations should be referred to in the text by numbers and not by terms like 'above', 'below', 'preceding' or 'following.

Infrared, ultraviolet, NMR and other spectra, DTA curves, etc. should be included only if they pertain to new compounds and/or are essential to the discussion; otherwise only significant numerical data should be included in the text.

References—The list of references should be prepared strictly in accordance with the style followed

in the Journal. In the text, references to literatures should be numbered consecutively, in the order of their first occurence, and should be indicated by superscripts at the relevant places; as far as possible the placement of references on numerals of other symbols should be avoided; in such cases the reference may be given in parentheses in running text, e.g. "this yielded for n a value of 2·3 (Ref. 5)". Full bibliographic details for all the references mentioned in the text should be listed in serial order at the end of the paper.

In citing references to research papers, names and initials of authors should be followed, in order, by the title of the periodical in the abbreviated form (underlined), the volume number (two lines underneath), the year within circular brackets and the page reference [e.g. Venkatesh, H G & Guha Sarkar, G, *Indian J. pure appl. Phys.*, **12** (1974), 502]. For names of periodicals, the standard abbreviations listed in the *World list of scientific periodicals* edited by P Brown & G B Stratton (Butterworths & Co. Ltd, London), 4th Edition, 1963-65, should be used. If the reference is to an article published without any authorship in a periodical, the title of the article takes the place of the author in the citation [e.g. The content, influence and value of scientific conference papers and proceedings. *Unesco Bull. Libr.*, **16** (1952), 113-26.]. If a paper has been accepted for publication, the names of the authors and the journals should be given followed by the words "in press" within circular brackets [e.g. Sastry, B. A. & Sastry, G. S., *Physica*, (in press).].

In the list of references, unpublished work, accepted papers in press and personal communications should be clearly distinguished.

Even if a reference contains more than two authors, the names of all the authors with their respective initials should be given. The abbreviations *et al.*, *idem* and *ibid* should be avoided.

Reference to a book should include details in the following order: names and initials of authors, the title of the book (underlined), name of publisher and place of publication within circular brackets and year [e.g. Herzberg, G, *Spectra of diatomic molecules* (D Van Nostand & Co. Inc., New Jersey), 2nd Edn, 1950, 31.]. If the reference is to the work of an author published in a book by a different author or edited by a different person, the fact that it is cited from the source book should be clearly indicated [e.g. Garlick, G F J, cited in *Encyclopedia of Physics*, Vol. 26—*Light and matter* II, edited by S Flugge (Springer Verlag, Berlin), 1958, 1.].

Proceedings of conferences and symposia should be treated in the same manner as books. Reference to a paper presented at a conference, the proceedings of which are not published, should include, in the following order, names and initials of authors, title of the paper (underlined), name of the conference, place where the conference was held and date (Deekshitulu, B L, *Design and fabrication of drum scanner for picture processing*, paper presented in the Symposuim on Applied Optics, Indian Institute of Science, Bangalore, 28-30 Nov. 1974).

Reference to a thesis should include the name of the author, title of the thesis (underlined), university or institution to which it was submitted and year of submission (e.g. Chandrasekaran, K S., *Studies on crystal structure and absolute configuration of crystals*, Ph. D. thesis, Madras University, 1956).

Reference to a patent should include names of patentees, country of origin (underlined) and patent number, the organization to which the patent has been assigned within circular brackets, data of acceptance of the patent and reference to an abstracting periodical where available [Trepagnier, J H, *US Pat.* 2,463,219 (to E I du Pont de Nemours & Co.), 1 March 1949, *Chem. Abstr.*, **43** (1949), 7258.].

Abbreviations and symbols—Abbreviations used should conform to the style of the journals. The following prefixes to units of measurements may be used for expressing submultiples and multiples.

Submultiples	*Abbreviation*	*Multiples*	*Abbreviation*
Deci- ($=10^{-1}$)	deci	deca- ($=10^{1}$)	deca-
centi- ($=10^{-2}$)	c	hecto- (10^{2})	hecto
milli- (10^{-3})	m	kilo- ($=10^{3}$)	k
micro- ($=10^{-6}$)	μ	mega- ($=10^{6}$)	M
nano- ($=10^{-9}$)	n	giga- ($=10^{9}$)	G
pico- ($=10^{-12}$)	p	tera- ($=10^{12}$)	T
femto- ($=10^{-15}$)	f		
atto- ($=10^{-18}$)	at		

Frequently repeating combinations of words, e.g. electric field gradient (EFG), junction field effect transistor (JFET), stimulated Raman emission (SRE), should be abbreviated subsequently, indicating the abbreviated form in parentheses, as shown, at the place of their first occurrence.

Nomenclature—Where too many symbols are used in the text, a section entitled "Nomenclature", explaining the significance of the various symbols, may be given and placed just above the Acknowledgement section.

Acknowledgement—Acknowledgements should not be exuberant and must be made only to real assistance rendered in connection with the work reported in the paper.

Appendixes—Appendixes, typed on separate sheets, should be numbered consecutively, in Arabic numerals, in the order of their occurence in the text, and should be placed at the very end of the paper.

Printed and Published by Shri D S Sastry, Publications & Information Directorate, Council of Scientific & Industrial Research, New Delhi, at the Leipzig Press, D-52 South Extension Part I, New Delhi 110 049.

Regd. D-(C)-540